

Synthesis, Characterization and Application of Anisotropic Cu Nanowires and Nanoparticles for the Electrocatalytic Reduction of CO₂

Pedro Mazaira Couce

Student number: 6624189

Utrecht, July 2021

A thesis submitted in fulfilment of the requirements for the degree of Master of Nanomaterial's Science in the Graduate School of Natural Sciences

Debye Institute for Nanomaterials Science

Supervisor: Shuang Yang

First examiner: Dr Ward van der Stam

Second examiner: Dr Peter Ngene



Utrecht University



Advanced
Research Center
Chemical Building
Blocks Consortium

Abstract

Two fundamental steps are needed to halt or at least slowdown climate change. One is the reduction of atmospheric carbon dioxide (CO_2), and two is developing more efficient renewable energy storage solutions. The electrocatalytic reduction of CO_2 toward fuels or valuable chemicals is a promising candidate to solve both problems. Copper (Cu) is a unique catalyst capable of the electrocatalytic conversion of CO_2 into a variety of carbon products like methane (CH_4), ethylene (C_2H_4), or formic acid (HCOOH). However, the low selectivity towards C_2 and C_{2+} products and the low stability of the bulk Cu catalyst complicate the economic viability of the electrocatalytic reduction of CO_2 . The use of Cu nanostructures as a catalyst has been shown to enhance the selectivity and the faradaic efficiency (FE) of the electrocatalysis due to the increased catalyst's surface area and the control of the exposed Cu facets. Exposure of the Cu (100) facets in the catalyst's surface has been demonstrated to enhance the FE for C_2 products, especially ethylene. During our research, we used a colloidal approach to synthesize Cu nanowires (NWs) with exposed (100) facets. However, a side nucleation of nanoparticles (NPs) was observed in all cases. Adjusting the synthesis parameters, we were able to control not only the length and thickness of the NWs but also the size and structure of the side nucleation. Little to no research has been done on the impact on selectivity and stability of combining different Cu nanocrystals, nanocrystals with different shape, size, and exposed facets. By controlling the concentration of ligands during the colloidal synthesis, we were able to produce three different Cu catalysts: NWs with a diameter of 30 nm and multi-shaped NPs, 30 nm NWs with nanopyramids and 40 nm NWs with multi-shaped NPs. After modifying the NP's concentration of the three different catalysts and comparing its electrocatalytic performance, we were able to show the impact of the NPs over the selectivity of the NWs. It has been revealed that a high concentration of NPs, in the case of 30 nm NWs with multi-shaped NPs and 30 nm NWs with nanopyramids, increases the selectivity towards ethylene and the stability of the catalyst. This increment is due to the creation of CO^* intermediate over the NPs' surface and its transfer to the NWs for its reduction to ethylene. The results of this research are promising with a maximum selectivity towards, however, there is a need for more research to understand the mechanism of this synergy and how to optimize it.

1. INTRODUCTION	5
2. THEORETICAL BACKGROUND	9
2.1 CATALYSIS.....	9
2.2 ELECTROCATALYSIS.....	10
2.3 ELECTROCATALYTIC REDUCTION OF CO ₂	13
2.4 COPPER AS A CATALYST	16
2.5 FACTORS THAT INFLUENCE THE CU CATALYST SELECTIVITY	18
2.5.1 <i>Impact of the crystal structure</i>	18
2.5.2 <i>Size of the catalyst</i>	20
2.5.3 <i>pH and electrolyte</i>	22
2.5.4 <i>Copper Nanowires as a catalyst</i>	23
2.6 COLLOIDAL SYNTHESIS.....	25
3. EXPERIMENTAL SECTION.....	29
3.1 CHEMICALS	29
3.2 COLLOIDAL SYNTHESIS	29
3.2.1 <i>Introduction to Schenk line</i>	29
3.2.2 <i>Synthesis of the catalyst</i>	31
3.3 SIZE SELECTIVE PRECIPITATION.....	32
3.4 UV–VIS ABSORPTION SPECTROSCOPY	33
3.5 X–RAY DIFFRACTION	34
3.6 ELECTRODE PREPARATION	34
3.7 ELECTROCHEMICAL MEASUREMENTS.....	35
3.8 NMR	36
3.9 RAMAN SPECTROSCOPY.....	37
3.10 ELECTRON MICROSCOPY	37
4. RESULTS AND DISCUSSION	38
4.1 SYNTHESIS OF THE CATALYSTS	38
4.1.1 <i>30 nm nanowires with a secondary nucleation of multi-shaped nanoparticles</i> ..	38
4.1.2 <i>30 nm Nanowires with a secondary nucleation of nanopyramids</i>	39
4.1.3 <i>40 nm Nanowires with a secondary nucleation of multi-shaped nanoparticles</i>	41
4.2 SIZE-SELECTIVE PRECIPITATION.....	43
4.3 CHARACTERIZATION PRACTICITY	46
4.3.1 <i>XRD</i>	46
4.3.2 <i>Sample after drop casting</i>	48
.....	51
4.4 ELECTROCHEMICAL PERFORMANCE AND CHARACTERIZATION POST SYHTESIS.....	52
4.4.1 <i>30 nm nanowires and multi-shaped nanoparticles</i>	52
4.4.2 <i>30 nm nanowires and nanopyramids</i>	59
4.4.3 <i>40 nm nanowires and multiple shapes nanoparticles</i>	68

4.7 COMPARISON OF THE ELECTROCATALYTIC PERFORMANCE BETWEEN THE DIFFERENT CATALYSTS AT -1.3 V VS RHE.....	74
5. CONCLUSION AND OUTLOOK	78
6. ACKNOWLEDGEMENTS	81
7. REFERENCES	82
8. ANNEX A.....	90
COLLOIDAL SYNTHESIS USED TO OPTIMIZE THE SYNTHETIZATION OF THE Cu NWS CATALYSTS.	90
9. ANNEX B.....	91
30 nm NWS WITH MULTI-SHAPED NPS.....	91
10 ANNEX C	92
30 nm NWS WITH NANOPYRAMIDS.	92
11 ANNEX D.....	93
40 nm NWS WITH MULTI-SHAPED NPS.....	93
12 ANNEX E	94
ABSORPTION SPECTRA OF THE 30 nm NWS WITH NANOPYRAMIDS	94

1. Introduction

Since the industrial revolution there has been an exponential increase in energy demand, which has been satisfied using fossil fuels.¹ The burning of fossil fuels provides a reliable and easy to use source of energy. However, the process of fuel consumption releases Carbon dioxide (CO₂) into the atmosphere as a collateral product. CO₂ is a greenhouse gas² and one of the principal actors in climate change.^{3,4}

In order to reduce CO₂ emissions and stop or slow down climate change, there has been an international effort to improve and promote alternative energy sources.⁵ The so-called green energies, like solar, wind or tidal energies, are environmentally friendly, renewable, and CO₂-free power sources.⁶ In 2018, green energies represented 26,2% of the total power generated worldwide and this percentage is projected to grow rapidly over time.⁷

However, one of the drawbacks of renewable energies is that they are not able to produce power at a constant rate. Green energy production depends on atmospheric conditions, like air currents for wind energy,⁸ or sunlight hours for solar energy.⁹ Thus, there is a need to store the energy produced during peak production time so it can be used whenever needed. To overcome this drawback, a new generation of more efficient and durable energy storage technology is needed.¹⁰

A solution that could tackle both problems, the atmospheric CO₂ and the energy storage necessities, would be the electrocatalytic reduction of CO₂ into fuels or valuable products. A catalyst able to favour the transfer of electrons for CO₂ reduction using power generated by renewable energies efficiently and economically would radically improve the viability of green energies and reduce the carbon footprint of our industrial society.¹¹

Hori *et al.* demonstrated in 1986 that copper (Cu) had the unique capability of catalysing the reduction of carbon dioxide by transferring electrons from the Cu to the CO₂ under a negative potential (As shown in **figure 1**).¹² Due to this transfer of electrons to CO₂, it was possible to reduce the Carbon Dioxide into other molecules with one carbon (C₁) like carbon monoxide (CO), methane (CH₄) or formic acid (HCOOH), hydrocarbons with two carbons (C₂) like ethane (C₂H₆), ethylene (C₂H₄) or ethanol (C₂H₅OH) and products with more than two carbon (C₂₊) like propanol (C₃H₈O).¹³ This differentiating characteristic of Cu in comparison with other metals to catalyse the production of hydrocarbons from CO₂ has been attributed to its distinct ability to bind the CO* intermediate, favouring the coupling with itself during the reaction, but not binding the H* intermediate, which would favour the competitive hydrogen evolution reaction (HER) producing H₂.^{14,15}

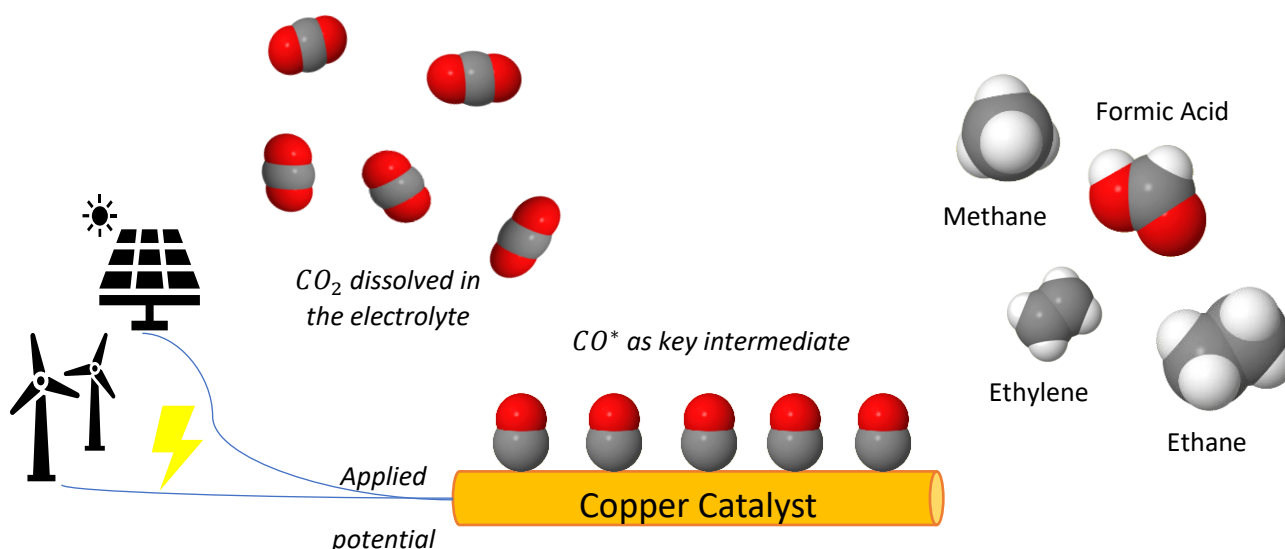


Figure 1: Diagram of the electrocatalytic reduction of CO₂ on a Copper catalyst using renewable energies as a energy source. CO₂ molecules dissolved in the electrolyte adhere over the copper catalyst's surface. Then, due to the applied potential, electrons are transferred to the CO₂ molecules, which get reduced and transform into intermediates. These intermediates will react and transform into hydrocarbons.

The catalyst's selectivity is defined as the proportion between a particular reaction product and the rest of the production.¹⁶ In the electrocatalytic reduction of CO₂, the Faradaic Efficiency (FE) is used to describe the selectivity and it is defined by the fraction of Faradaic charge utilized to produce a given product.^{17,18} The selectivity toward carbon products of the electrocatalytic reduction of CO₂ was studied by Hori *et al.* using bulk polycrystalline copper. They were able to have an 82% Faradaic Efficiency for carbon species which main product were methane (29,4%) and ethylene (30,1%).¹³

The improvement of the selectivity is one of the most critical factors for the economic viability of the electrocatalytic reduction of CO₂.¹¹ For example, ethylene is used as a chemical intermediate for the preparation of a wide variety of the most used plastics in the world and it is mainly produced by petrochemical sources.¹⁹ If we were able to increase the selectivity of CO₂ reduction toward ethylene substantially, it would be possible to use renewable energy to compete economically with fossil fuels in ethylene production.¹¹ Furthermore, it would be possible to use the selectivity toward ethylene to significantly reduce the CO₂ footprint of plastics and improve their reusability. Ideally, with a perfect selectivity toward ethylene, the energy produced by the heat obtained with the incineration of postconsumer plastics could be used to electrochemically reduce the combustion products (CO₂) into ethylene that can be converted again into recycled plastics(**Figure 2**).²⁰

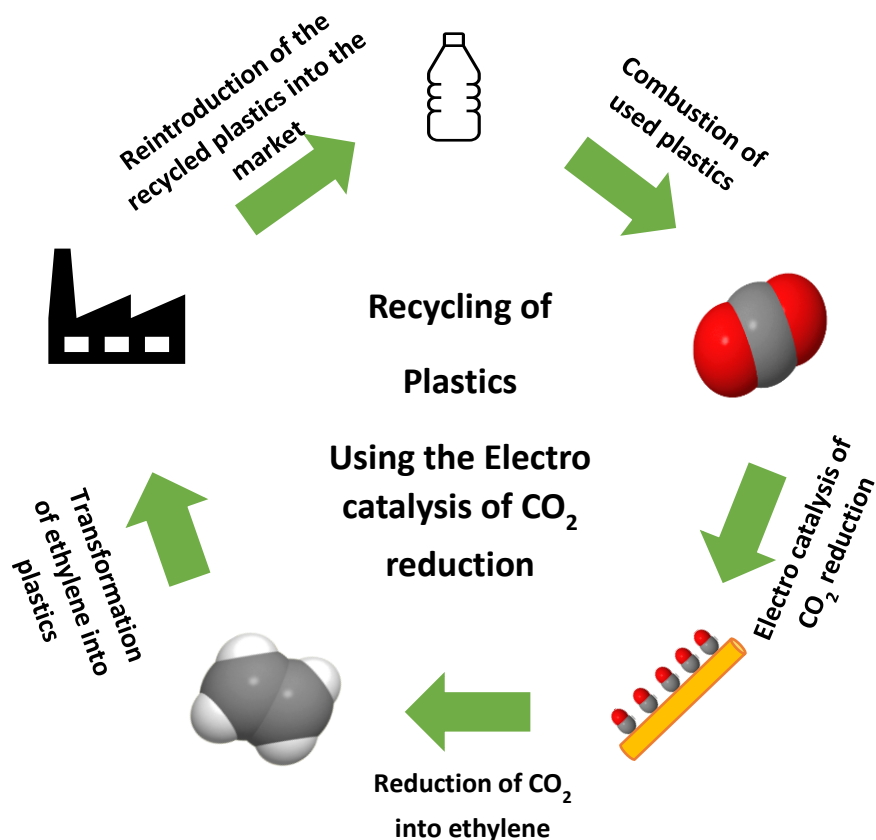


Figure 2: Scheme of the ideal recycling of plastics using a perfect ethylene's selectivity from the electrocatalysis of CO₂ reduction

The final selectivity of the electrocatalytic reduction of CO₂ is linked not only to the catalyst's composition^{12,13,21} but also the catalyst's size²², geometry²³, and exposed facets²⁴. For example, in the work of Manthiram *et al.*, using 7 nm spherical Cu NPs they were able to reach an 80% selectivity toward methane at -1.4V vs RHE. This 80% FE toward methane of the Cu NPs doubles the FE toward methane of bulk Cu at the same voltage.²⁵ Moreover, Wang *et al.* produced Cu rhombic dodecahedrons with exposed facets (110), which not only had a higher selectivity towards methane at -1.4V than bulk copper (60% FE) but also were able to reduce CO₂ to C₃H₈ (3% FE).²⁶

However, if we are interested in a high selectivity towards C₂ products, a structure with a very promising selectivity toward ethylene is the copper nanowire. Using copper nanowires with a 50 nm diameter, Hongyi Zhang *et al.* were able to obtain a combined selectivity toward ethylene and ethane of 60% at -1.1V vs RHE with no trace of Methane or any liquid product.²⁷ However, this selectivity is highly dependent on the size and structure of the surface. For example, thin penta-twinned nanowires with a diameter of 20 nm had a selectivity toward methane of 55% at -1.25V Vs RHE.²⁸ The final product's difference is attributed not only to the diameter but also to the consequent difference of the surface's structure and the proportion between the exposed facets, (100) and (111) of the crystalline copper and the boundaries among those facets.¹⁷

During this research, we have synthesized three copper nanowires catalysts with controlled exposed facets (100) and (111) and with a secondary nucleation in the form of multi-shaped nanoparticles or nanopyramids using a colloidal approach.

There have been multiple studies on the effect of different nanostructures and exposed facets on the Copper catalyst final selectivity. However, there has been little to none published research on the combination of two different types of Cu nanostructures, nanostructures with different sizes, shapes and exposed facets, and how the catalyst's performance would be affected. This knowledge gap opens many interesting questions which should be looked upon.

- Do the nanoparticles present in the nanowire catalyst enhance the FE towards ethylene of the nanowires?
- How do the different shape and sizes of these nanostructures impact the nanowire's catalyst performance?
- What is the stability of Cu anisotropic NPs, like NWs, under operando conditions? Does the presence of other nanostructures with different shapes have an effect on the stability of the catalyst?

We have explored the impact of the size, shape, and concentration of these secondary nucleations on the final selectivity and stability of the copper nanowire catalyst.

In chapter two, a theoretical background has been provided with the key concepts to understand the electrocatalytic reduction of CO₂ and how the structural characteristic of the catalyst influences its selectivity and a short introduction to how to determine these catalyst's structural characteristics using colloidal synthesis. In chapter three, the experimental conditions of our research for the colloidal synthesis and the electrocatalytic reduction of CO₂ are described. In chapter 4, we have described the nanowires and secondary nucleations structure using XRD, TEM and SEM. Afterwards, we have shown and discussed the reasons for the electrochemical performance of all these catalysts compared to the same catalysts with a lower concentration of secondary nucleation and its characterization after activity. Finally, in chapter 5 we discuss the conclusions of our research.

2. Theoretical Background

2.1 Catalysis

Even though the phenomenon of catalysis was not defined until the 19th century, humanity has benefited from it for centuries. Catalysing the breakdown of sugar molecules found in grain or fruits to produce ethanol in the form of alcoholic drinks have been done by human beings since the Neolithic era.²⁹ Nowadays, 90% of all industrial chemicals are made with the aid of catalysts, and the global market size value of catalysts in 2019 was 33.9 billion dollars.³⁰

The IUPAC (International Union of Pure and Applied Chemistry) defines a catalyst as a substance that increases the reaction rate without modifying the reaction's overall standard Gibbs free energy change.³¹ In general, catalysts provide an alternative reaction pathway with lower activation energy, which improves the kinetics of a reaction. Catalysts are not consumed during the process, which allows them to be used several times. Often, only small amounts of catalyst are needed to increase the production rate considerably.³²

If a catalyst is present in a reaction in a different phase (solid, liquid or gas) than the reactants, it is defined as heterogeneous catalysis (**Figure 3**).³³ Heterogeneous catalysts are solids, like zeolites, metals or alumina, and act as a substrate for liquid or gaseous reactants.^{34,35} On a solid heterogeneous catalyst, the reactants would adsorb on the catalyst's surface and react on the active sites. These catalytically active sites can be an exposed crystalline facet of a metal, an acidic spot in a zeolite, a crystal boundary, or other types of structure that would interact with the reactants. Increasing the number of these

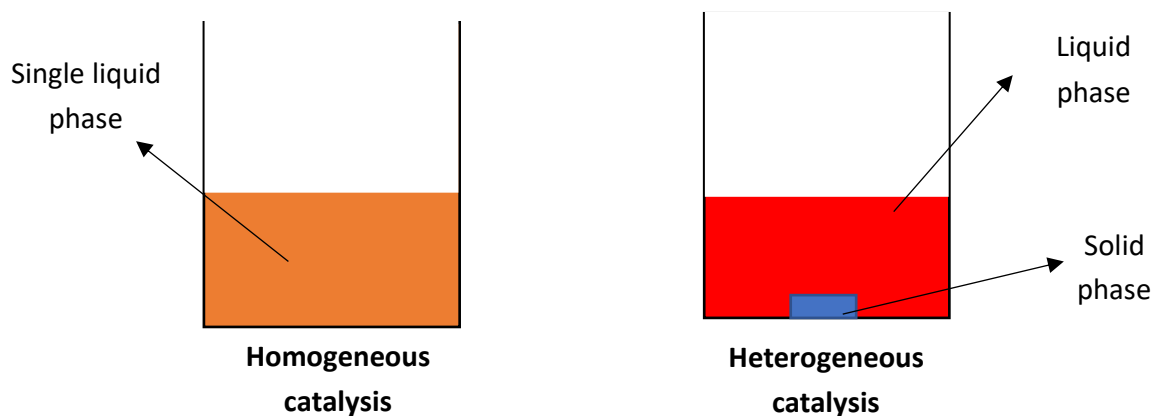
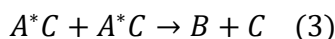


Figure 3: Representation of the difference between homogeneous and heterogeneous catalysis

active sites on the catalyst' surface would alter the selectivity and activity of the reaction.¹⁷ Therefore, nanomaterials are an especially suitable substrate for heterogeneous catalysis as their total surface area is much higher than macromaterials.

A typical reaction on a heterogeneous catalyst could be described using the Langmuir–Hinshelwood mechanism:³⁶



Reaction 1–3: Langmuir mechanism³⁶

Where A is the reactant, C is the Catalyst, A* is the intermediate and B is the product. On the first step A is adsorbed on the catalyst' surface. In the second step, A reacts on the catalyst's active site to form the A* intermediate, which is still adsorbed on the catalyst. Finally, both intermediate react with each other to create a product that will disengage from the catalyst. The langmuair mechanism is shown in **figure 4**.

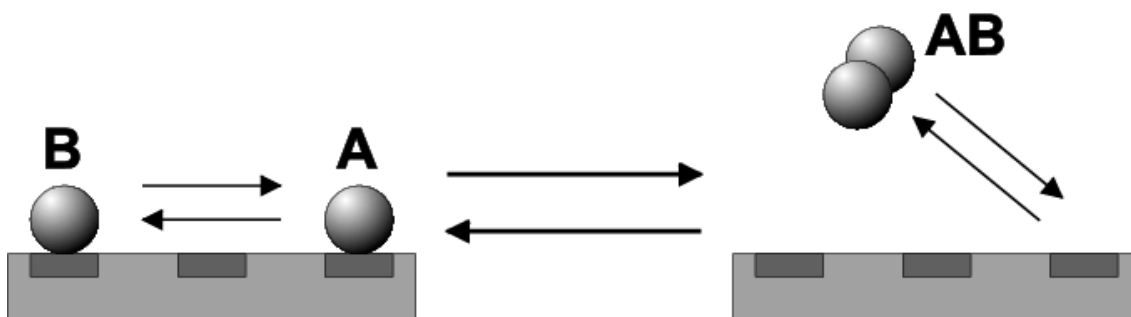


Figure 4: Scheme of the Langmuir mechanism. Extracted from the work of Markus Fertig³⁷

2.2 Electrocatalysis

An electrocatalyst is a type of heterogeneous catalyst where the modification of the reaction rate is done in an electrochemical cell at an electrode surface due to redox reactions.³⁸ An electrochemical cell is a device that is able to generate electricity from a spontaneous redox reaction (Galvanic Cell) or, in the case of electrocatalysis, that uses electricity to produce a nonspontaneous redox reaction (Electrolytic Cell). A typical electrolytic cell for electrocatalysis is usually composed of three electrodes. An electrode is an electrical conductor used to contact the metallic part of the cell with the electrolyte. The three electrodes are the anode, where the oxidation reaction occurs, the cathode, where the reduction reaction takes place, and the reference electrode, which has a stable and well-known electrode potential that is used to characterize the relative potential of the cell. These three electrodes are submerged in an electrolyte solution, which is an electrically neutral solution of a substance that dissociates into positive (cation) and negative (anion)

charged ions. Separating the anode and the cathode, an H⁺ exchange membrane allows the transport of charge between the cathode and the anode (**Figure 5**).^{39,40}

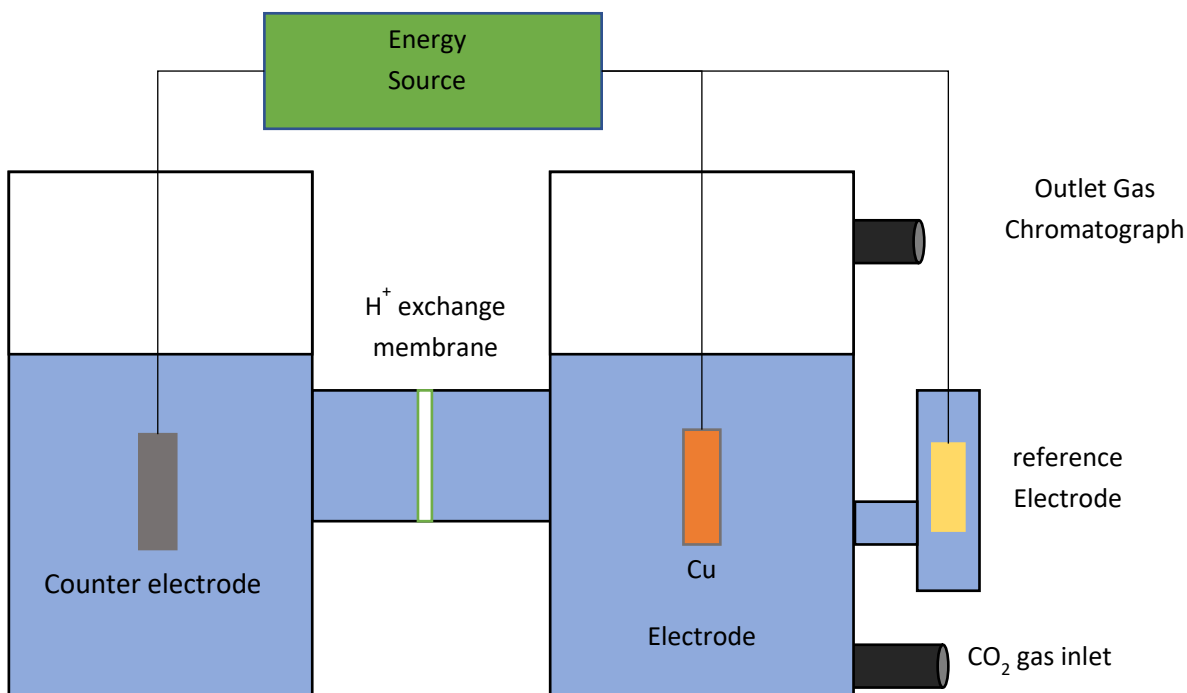


Figure 5: Scheme of an Electrolytic Cell for CO₂ reduction using a copper catalyst attached to a Gas Chromatograph

During electrocatalysis, a difference of electric potential is imposed between the working electrode, the electrode in which the catalysis reaction occurs, and the counter electrode to create an electric current. The difference of electric potential is measured by voltage (V) and the current (I), the number of charges that passes in a conductor per second, is measured in Amperes (A). Using the Electrical Resistance (R) of the cell, which determines the system's opposition to the electric flow, measured in Ohms (Ω), we can link the voltage and current of the system using Ohm's law (**equation 1**).

$$I = \frac{V}{R} \quad (1)$$

Equation 1.

When current flows in an electrochemical cell due to an imposed voltage, a potential disturbance will occur between the working electrode and the counter electrode due to the system's resistance, which is called an Ohmic drop. Using Ohm's law we can determine the potential drop (**Equation 2 and 3**).⁴¹

$$\Delta V_{ohmic} = I * R_s \quad (2)$$

$$\Delta V_{measured} = \Delta V_{applied} - \Delta V_{ohmic} \quad (3)$$

Equation 2–3

Where ΔV_{ohmic} is the Ohmic drop, I is the intensity of the current, R_s is the resistance of the system, $\Delta V_{applied}$ is the voltage difference imposed by the system and $\Delta V_{measured}$ is the real voltage that is measured.

Therefore, to have a stable and comparable voltage, we need a reference electrode with a well-known voltage and no current between it and the working electrode. As there is no practical method to calculate an electrode's potential in isolation, we can only calculate the potential difference between two materials. To be able to compare data of electrical cells, it is collectively agreed that the Hydrogen electrode has a potential of 0 V and the standard potential of any electrode is the difference between itself and the Standard hydrogen electrode (SHE).⁴² To translate any potential from a different reference electrode to SHE, we can use the Nernst Equation (**Equation 4**).⁴³

$$E = E_0 - \frac{RT}{zF} \ln(Q) \quad (4)$$

Where:

E = Reduction potential (V)

E_0 = Standar potential (V)

R = Universal Gas constant = $8,314 \frac{J}{K mol}$

T = Temperature (K)

z = ion charge(number of electrons)

F = Faraday constant = $96485 \frac{C}{mol}$

Q = reaction quotient (a measure of the relative amounts of products and reactants present during a reaction at a particular point in time)

Equation 4

However, if one of the reactions happening in the electrodes forms H^+ or OH^- the voltage of the system would depend on the pH. If voltage is pH dependant, SHE is not longer used but instead the Reversible Hydrogen Electrode(RHE). The Nernst equation can be used to show how the concentration of H^+ can determine the voltage assuming a hydrogen partial pressure (P_{H_2}) of 1 atm and a temperature of 25° C (**Equation 5–7**):⁴⁴

$$E_{H/H_2} = E_0 - \frac{RT}{zF} \left(\frac{P_{H_2}}{[H^+]^2} \right) = E_0 + 0,01285 * 2 \ln[H^+] \quad (5)$$

$$\ln(x) = 2.303 * \log(x) \quad (6)$$

$$E = E_0 + 0,059 * pH \quad (7)$$

Equation 5–7

However, due to experimental atmospheric conditions (pressure and temperature), the characteristics of the catalyst (difference in local pH, conductivity, morphology and composition) and the electrolyte, there is a difference between the theoretical reduction potential and the experimental reduction potential.⁴⁵ This difference is called overpotential and reducing to a minimum this overpotential is fundamental to make the electrocatalytic reduction of CO₂ economically viable.¹¹ Less overpotential means less energy needed for electrocatalysis.

To characterize the electrochemical activity of the catalyst, two techniques are usually used: linear sweep voltammetry (or cyclic voltammetry) and chronoamperometry.^{13,45,46} Linear Sweep Voltammetry is an electrochemical technique that measures a redox-active solution's response (in the form of current density) to a linearly potential sweep between two or more set values. If the voltage applied is not linear but a cycle, it is called cyclic voltammetry (CV). It allows you to measure the current density during the reduction and oxidation process in one cycle. Chronoamperometry is a time-dependant technique in which a constant potential is imposed between the reference electrode and the working electrode for a determined time and the resulted current density is measured.

2.3 Electrocatalytic reduction of CO₂

Suppose we have an electrolytic cell with the electrolyte saturated with CO₂ and we test the CO₂ reduction using a working electrode composed of any pure metal. In that case, we can divide the possible results into four groups according to their selectivity (**Figure 6**).⁴⁵

Ti Titanium 99.7 %	Fe Iron 94.8 %	Co Cobalt	Ni Nickel 88.9 %	Cu Copper 67.5 %	Zn Zinc 79.4 %	Ga Gallium 79.0 %	Ge Germanium
Ru Ruthenium	Rh Rhodium	Pd Palladium 26.2 %	Ag Silver 81.5 %	Cd Cadmium 78.4 %	In Indium 94.9 %	Sn Tin 88.4 %	
Os Osmium	Ir Iridium	Pt Platinum 95.7 %	Au Gold 87.1 %	Hg Mercury 99.5 %	Tl Thallium 95.1 %	Pb Lead 97.4 %	

Symbol Name Faradaic efficiency	H₂	CO	HCOOH	Beyond CO*
--	----------------------	-----------	--------------	-----------------------

Figure 6: Metal catalysts classification by their product for the electroreduction shown in a periodic table with colors and major product faradaic efficiency. Four groups are identified: H₂ (red), formic acid (yellow), CO (blue) and beyond CO* (cyan). Table extracted from the work of Bagger *et al.*¹⁴

- 1) Gold (Au), Silver (Ag) and Zinc (Zn) mostly produces CO
- 2) Lead (Pb), Mercury (Hg), Cadmium (Cd), Indium (In), Tin (Sn), or Thallium (Tl) which mainly produce Formate.
- 3) Iron (Fe), Platinum (Pt), Nickel (Ni) and Palladium (Pd) which do not reduce CO and mainly produce H₂ from water by the competing pathway toward hydrogen evolution reaction (HER).
- 4) Copper (Cu) has the unique property between metals of catalysing the electrochemical reduction of Carbon dioxide into CO, formate, hydrocarbons, and alcohols.

The difference between the four groups' selectivity is attributed to the strength of the bond between the molecular intermediates for the CO₂ reduction (CO*, COOH*, HCOO*)^{14,47,48} and the intermediates created by the Hydrogen Evolution Reaction (HER) of water (H* and OH-).⁴⁹ We can measure the strength of a bond using the bonding energy, which reflexes the amount of energy needed to desorb the intermediate from the catalyst surface. The more negative is the bonding energy, the more energy is required to separate the intermediates. In the case of CO₂ reduction, as we can see in **Figure 7** extracted from the work of Alexander Bagger *et al.*¹⁴, both group 1, which produces CO, and group 2, which produces formate, have a negative, but close to zero, binding energy for the CO* intermediate.

However, group 2 has a more positive binding energy for H* than the first group. This difference means that at potentials where we have CO₂ reduction, we find almost no H* on the surface for the second group, which favour the creation of the COOH* intermediate. Whereas, for the first group, the surface would have the hydrogen intermediate, favouring the competitive HER reaction. On the other hand, the third group has a strong negative binding energy for both CO* and H*, which means that the intermediates do not desorb from the catalyst's surface blocking the active sites and therefore, CO₂ can not continue any reduction pathway and eventually the only possible reaction is HER.¹⁴ This process is called catalyst poisoning.

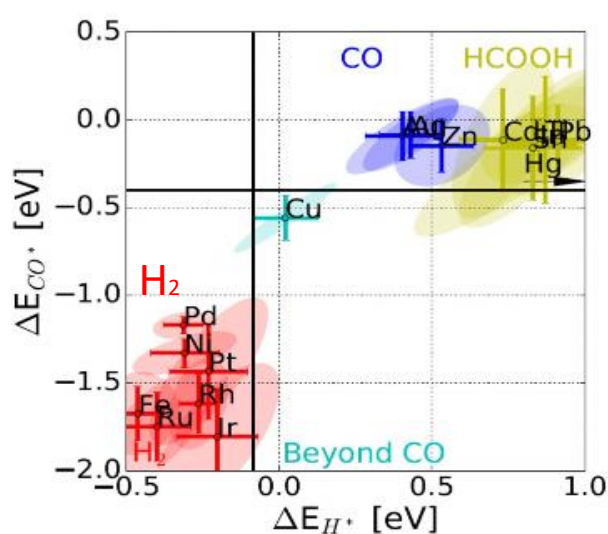


Figure 7: Binding energies (ΔE) for H* and CO* of the different metals. The ellipsoids represent the coupled firsts confidence interval of binding energies with respect to Au, while the Au error ellipsoid is given with respect to the slab and the gas phase. Table extracted from Alexander Bagger *Et Al.*¹⁴

Copper is a unique catalyst because it has an intermediate negative binding energy for CO^* and positive for H^* . This characteristic means that CO will bind with the surface long enough to react but not poison the catalyst. Moreover, the CO adsorption would compete with the adsorption of H_2O molecules on the active sites, avoiding the Hydrogen evolution reaction.

The mechanism of the formation of products beyond CO , like ethylene or methanol, is still under discussion. The reduction of CO_2 is a highly complex process that implies the transfer of multiple electrons and protons with a variety of products and intermediates. For example, as we can see in **Figure 8**, at least 9 steps and the transfer of 12 electrons and 8 protons is necessary to be able to form a molecule of ethylene from the adsorption of 2 molecules of CO_2 . Meanwhile, for the formation of formic acid, hydrogen or CO , only 2 electrons are necessary.^{14,50}

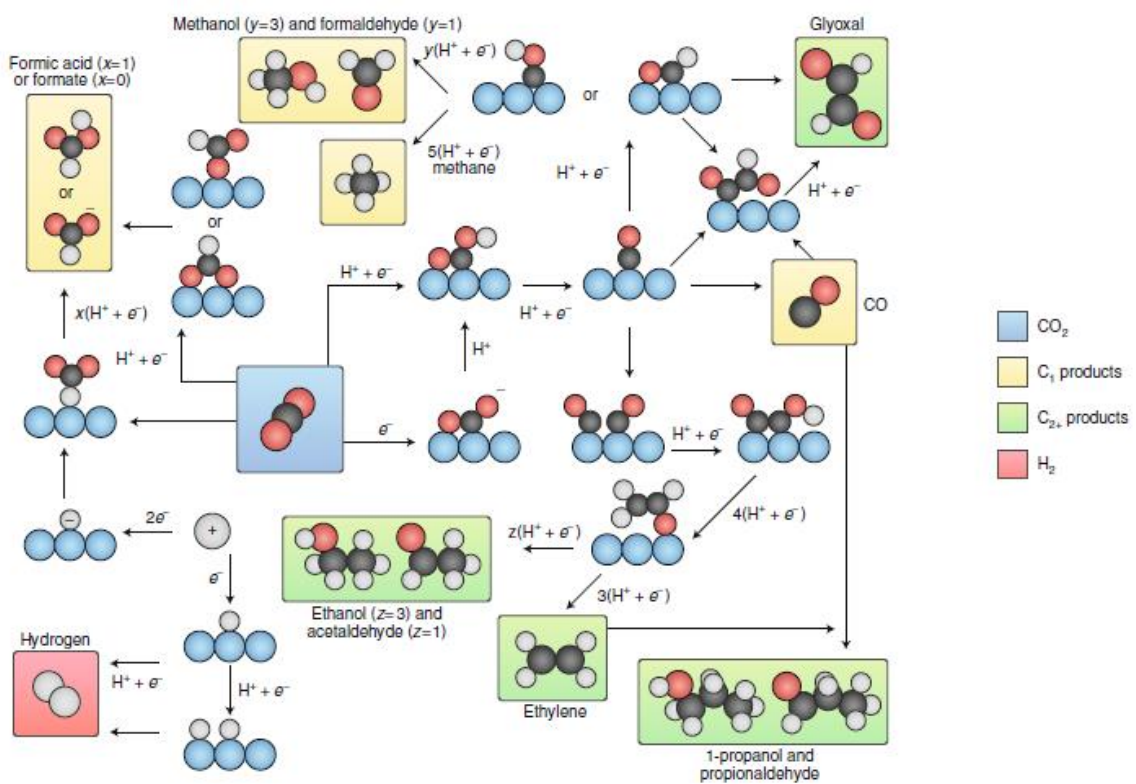
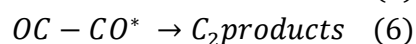
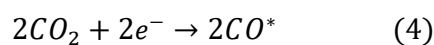


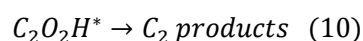
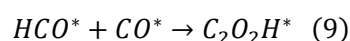
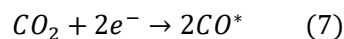
Figure 8: Reaction pathways for CO_2RR towards different products. Black spheres, carbon; red spheres, oxygen; white spheres, hydrogen; blue spheres, copper catalyst. The arrows indicate whether proton or electron transfer takes place. Figure extracted from the work of Birdja *et al.*⁵⁰

A more simplified example would be the mechanism proposed in 2016 by Albertus D. Handoko *et al.* for the reduction of CO_2 toward C_2 products based on the dimerization of CO^* .¹⁵



Reaction 4–6: Reaction mechanism for CO_2 reduction toward C_2 products according to Handoko *et al.*¹⁵

However, in 2018, Alejandro P. Garza *et al.* suggested a different approach to explain the disparity of selectivity between different crystalline facets presented in the Cu catalyst²⁴ (see **section 2.4**). They proposed a mechanism of CO₂ reduction on the surface of a copper's crystalline facet (100):⁵¹



Reaction 7–10: Reaction mechanism for CO₂ reduction toward C₂ products on (111) facets according to Garza *et al.*⁵¹

Both approaches, and most other theories, have in common that CO* is the key intermediate for the reduction of CO₂ toward C₂ products.^{13,52} The characteristic binding energy of copper to the CO* and H* is the most likely explanation of why Cu is the only metal able to catalyse CO₂ reduction to products beyond CO.

2.4 Copper as a catalyst

Hori *et al.*¹³ and Kuhl *et al.*⁴⁶ describe the selectivity and activity of bulk polycrystalline copper catalysts with an electrolyte of 0.1 M of KHCO₃ (pH 6,8) using two electrochemical techniques, linear sweep voltammetry and chronoamperometry (CA), explained in **section 2.2**.

If we look at **Figure 9 a)**, the linear sweep voltammetry of the Cu catalyst between -0.4 V and -1.2 V is exposed. On the X-axis of the table, we can see the potential impose between the working electrode and the reference electrode in Volts. In the Y-axis, the excitation signal of the redox reaction is represented with the current density in units of mA/cm², which gives us information on which voltages are more catalytically active and more electrons transfer is taking place. In **Figure 9 b)** Hori *et al.*¹³ and Kuhl *et al.*⁴² have combined the CA technique with gas chromatography, which allows the separation and identification of the gases produced during catalysis,⁵³ and Nuclear Magnetic Resonance (NMR), which enables the identification of the liquid products.⁵⁴ This

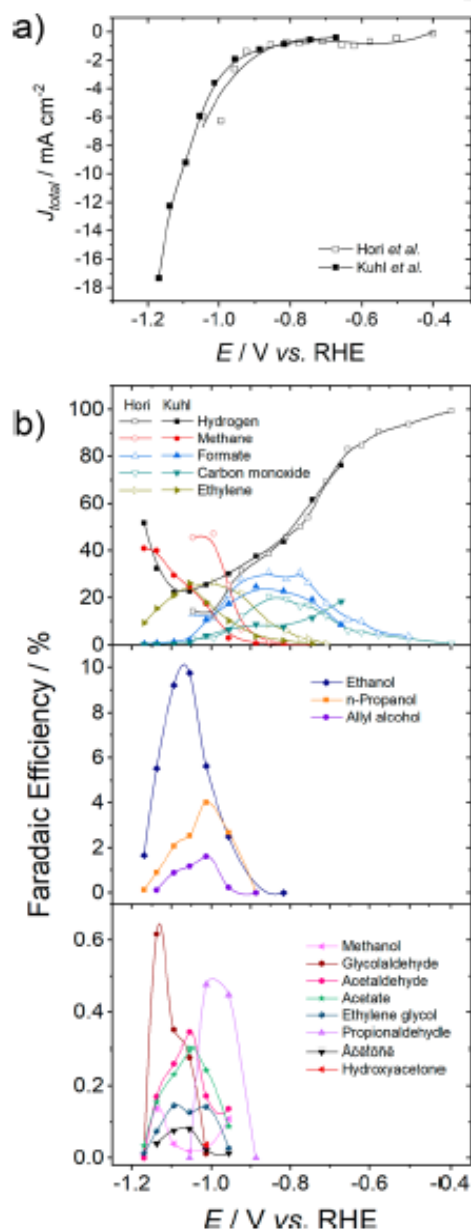


Figure 9: A) Linear sweep voltammetry with total current density of the CO₂ reduction on polycrystalline copper. B) Faradaic Efficiency for different products created during the chronoamperometry with polycrystalline copper. Table Extracted from Nitopi *et al.*⁴² with data from Hori *et al.*¹³ (hollow) and Kuhl *et al.*⁴⁹ (filled)

combination of techniques allows them to describe the bulk, polycrystalline catalyst selectivity at different voltages. Using the current density obtained from the CA and the concentration of products detected by the NMR and the chromatographer, it is possible to calculate the faradaic efficiency toward any giving product using **equation 8**

$$FE = \frac{Z * n * F}{Q} * 100 \quad (8)$$

Z = Number of electrons needed for the reaction

n = number of moles generated of an specific product

F = Faraday constant = $96485 \frac{C}{mol}$

Q = Charge passed during the bulk electrolysis C

Equation 8

In the case of CO₂ reduction, using polycrystalline copper as a catalyst with a 0.1 M KHCO₃ electrolyte, the linear sweep on figure 7 a) shows a small peak at -0.6 V. This peak has been attributed to the onset of the CO₂ reduction.⁴⁶ If we compare with the selectivity data extracted from the chronoamperometry that can be checked in **Figure 9 b)**, this peak corresponds to the start of the formation of CO and Formate. On more positive potentials than -0.6 V, the catalyst produces mainly hydrogen. The peak of selectivity from both CO and Formate is around -0.8 V. Once the -0.8V cathodic bias is surpassed, the current increases exponentially and C₂ and C₂₊ products start to appear. As shown before, the intermediates CO* and HCOO* are essential for the formation of C₂ products. Once the system has enough energy to reduce those intermediates before they get desorbed, the selectivity toward C₂ products increases significantly. At intermediate overpotentials (-0.6 V to -1.1 V) the HER reaction goes from 80% FE to a 20%. This is because the catalyst's active sites are mostly covered by CO* intermediate and the HER is avoided. However, at more negative overpotentials, the hydrogen evolution becomes more prevalent (50% FE at -1.2 V). This rise in the hydrogen selectivity is because at higher cathodic bias, the surface's energy increases. A high superficial energy causes faster desorption of CO₂ and intermediates, which avoids its reduction and favours HER.

As seen In **Figure 9 b)**, at any giving voltage point where there is a substantial production of carbon products, there is a wide range of products, being the maximum selectivity to a single C product at -1.1 volts with a close to 50% FE for methane on Hori *et al.* experiments. Therefore, to make the catalysis of the reduction of CO₂ economically profitable, it is necessary to optimize the selectivity towards an economically attractive product, like ethylene, ethanol or C₂₊ products.¹¹ The peak for ethylene formation at -1 V has a FE close to 30%, but several factors can influence and maximize the FE toward ethylene or any giving product. A selection of these factors will be explored in the next section.

2.5 Factors that influence the Cu catalyst selectivity

2.5.1 Impact of the crystal structure

The atomic surface of a crystal can be described by the combination of its unit cells, which are the smallest repeating unit having the complete symmetry of the crystal structure. These unit cells are characteristic of different atomic compositions and depend on various factors like the size of the atoms or the bonding energy. These unit cells can be described using a notation called Miller Index. Miller index use three integers (h k l) to determine a family of lattice planes that, in combination with the unit cell structure, allows us to describe the atomic surface.

Pure copper has a Face Centered Cubic (FCC) unit cell⁵⁵ that can be described as a cube with one atom at each corner and one atom at the centre of each plane. The miller index integers (hkl) describe the exposed plane of the crystal. An example of the three low miller index structures can be found at **figure 10**.

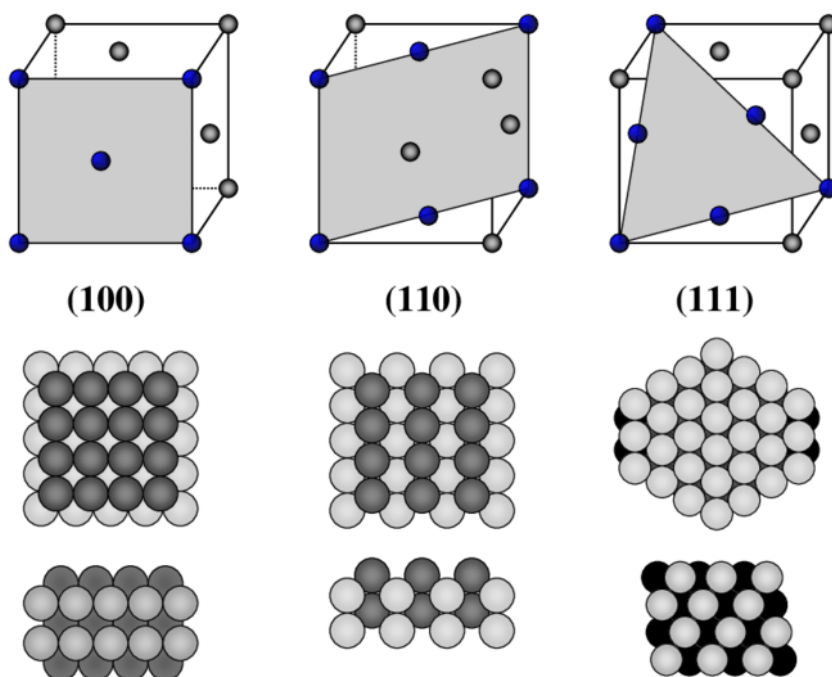


Figure 10: Representation of the three low miller index on a Face Centered Cubic, image extracted from Karl JJ Mayrhofer Thesis.⁵⁶

Hori *et al.* described the direct relation between the exposed facets of the Cu catalyst and the final product of the catalysis. In order to show this relation they tested the electrolytic cell using an 0.1 molar KHCO_3 electrolyte and imposing an electric current of 5 mA and measuring its potential on a Cu catalyst with different exposed facets.²⁴

Crystal orientation	Potential/V vs SHE	Potential/V vs RHE	Faradaic efficiency/%							
			CH_4	C_2H_4	CO	Alc.	Ald.	HCOOH	H_2	$\text{C}_2\text{H}_4/\text{CH}_4$
			Cu(S)-[n(100) × (111)]							
(100)	-1.40	-1.00	30.4	40.4	0.9	12.0	4.4	3.0	6.8	1.3
(11 1 1)	-1.37	-0.97	8.9	50.2	1.8	17.7	4.4	3.2	8.8	5.8
(711)	-1.34	-0.94	5.0	50.0	1.1	14.2	6.4	4.6	15.6	10.0
(311)	-1.37	-0.97	36.0	23.8	2.6	5.2	3.4	14.0	13.3	0.7
(111)	-1.55	-1.15	46.3	8.3	6.4	3.3	2.7	11.5	16.3	0.2
			Cu(S)-[n(100) × (110)]							
(810)	-1.38	-0.98	6.4	45.1	1.4	28.8	2.0	1.5	8.7	7.0
(610)	-1.37	-0.97	7.6	44.7	0.9	29.3	2.7	1.4	9.0	5.9
(510)	-1.38	-0.98	8.1	42.3	2.1	29.5	5.6	2.9	10.5	5.2
(210)	-1.52	-1.12	64.0	13.4	2.2	7.3	1.5	5.5	7.0	0.2
(110)	-1.55	-1.15	49.5	15.1	0	7.4	3.1	6.6	18.8	0.3

Table 1: selectivity of the different exposed facets of Cu catalyst using 0.1 M KHCO_3 electrolyte imposing an electric current of 5 mA, table extracted from Nitopi *et al.*⁴⁵ with data from Hori *et al.*²⁴

If we look at the results of Hori *et al.* in **table 1**, for the low miller index planes (100, 110 and 111) we can see that the facet (100) showed the highest FE toward ethylene with a 40.4% FE and the lowest selectivity toward H_2 with a 6.8%. On the other hand, (111) facet and (110) facets showed a higher tendency to create methane, with 46.3% and 49.5% respectively. Furthermore, (110) facets also distinguish themselves for having the higher selectivity toward H_2 with an 18.8% and having a 0% selectivity toward CO. Therefore, maximizing the (100) facets and minimizing (110) should enhance the ethylene production while reducing H_2 selectivity.

After electrocatalysis at low overpotential (-0.45 V vs RHE) on a Cu catalyst with (100) exposed facets, it is possible to find a low ethylene concentration but zero selectivity toward methane.⁴⁸ According to the work of Calle-Vallejo and Marc Koper,⁵⁷ the reason for this low overpotential selectivity is that on the (100) surface favours the dimerization of CO which is the rate depending step for the formation of C_2 products. Therefore, this low energy pathway toward C_2 products does not share intermediates with methane formation, which increases the selectivity toward C_2 products and reduces it for methane. On the other hand, over the (111) facets, the low energy pathway toward C_2 products shares intermediate with the formation of CH_4 , which explains the higher selectivity toward methane.

2.5.2 Size of the catalyst

The size of the copper catalyst is fundamental for the final selectivity and activity of the catalytic reaction. Decreasing the size of the catalyst from the macro to the nanoscale will lead to an exponential increase of the surface to volume ratio, which raises the number of active sites and the number of the metal ions that are influencing the catalytic process.^{17,45} Therefore, if we compare two catalysts of the same volume where the first is a perfect sphere and the other one is a combination of nanoscale spheres; the surface area of the second catalyst is drastically higher than the first one as shown of **figure 11**.

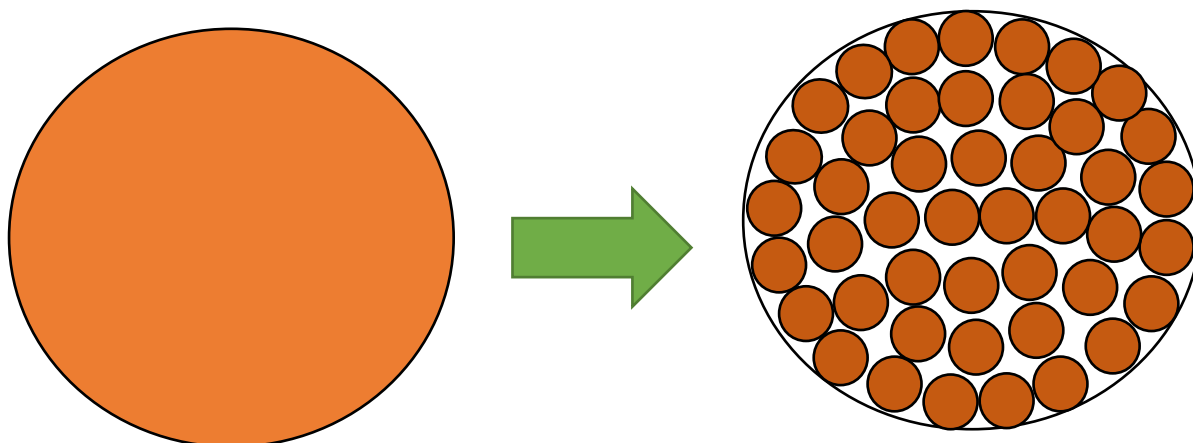


Figure 11: Representation of the increase of surface with the reduction of particle's volume

An atom inside a unit cell has a number of ligand donors atoms to which the metal is directly bonded and these ligand donors are the nearest neighbours of that atom. The number of these ligand donors or nearest neighbours is called the coordination number.³¹ If the size of a particle is decreased, the number of irregularities in its surface increases. These irregularities can take the form of kinks, steps or edges (**figure 12**). Atoms in this location have a low coordination number due to the lack of neighbouring atoms. Uncoordinated atoms lead to perturbed electronic structures and can lead to an increase in activity due to the appearance of dangling bonds. Dangling bonds are unsatisfied valences on a immobilized atom.³¹ These unsatisfied valences are extremely active and increase the catalytic activity of the metal.

Another aspect of size's impact on the activity and selectivity of the catalyst is that the modification of the particle size can influence the binding strength of the different intermediates with the surface of the catalyst, which would impact the final selectivity of the catalyst.⁵⁸

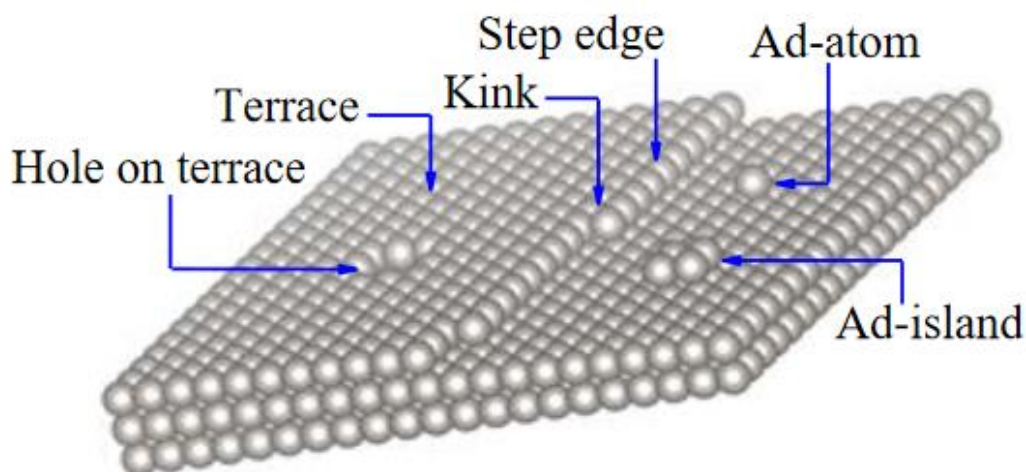


Figure 12: Hard sphere model of a metal surface, indicating different irregularities like terrace, step, kink, hole, ad-atom and ad-atom island. Figure extracted from Farias *et al.*⁵⁹

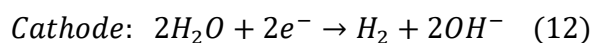
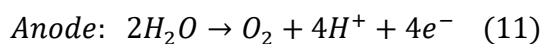
In the case of the Cu catalyst, there are conflicting results on the relation between size and final selectivity. Reske *et al.* showed that using spherical Cu nanoparticles under 30 nm, the catalysis's main product was hydrogen, but larger nanoparticles primarily reduced CO₂.⁶⁰ In contrast, Manthiram *et al.* showed an 80% Faradaic Efficiency toward Methane with spherical Cu nanoparticles with a diameter of 7 nm.²⁵ However, directly comparing both results would be a mistake as they used different synthesis methods and reaction conditions. Moreover, Manthiram *et al.* NPs tends to combine forming agregations of 25 nm diameter under CO₂ reduction conditions whereas, Reske *et al.* nanoparticles remained stable during catalysis.

Loiudice *et al.* compared copper nanocubes and nanospheres of different sizes using a very similar synthesis approach and similar catalysis conditions. They showed that peak selectivity toward C₂ products was measured for nanocubes with a side 44 nm reaching a 41% selectivity toward ethylene with a -1.1 V cathodic bias. Moreover, nanoparticles with 7.5 nm diameter had a selectivity toward Hydrogen of 25% whereas nanoparticles with a diameter of 27 nm had a FE of 45% toward H₂.²² This trend is the opposite that the one founded on the work of Reske *et al.*, which showed that smaller nanoparticles produced more H₂.

Reducing the size of a nanocube increases the proportion of low coordination atoms on the edges of the nanocube, these boundaries between the different (100) exposed facets are highly catalytically active due to the higher energy state of its uncoordinated atoms.⁴⁵ Lojudice *et al.* concluded that at 44 nm there is an optimal balance between the number of these more chemically active atoms on the grain boundary and the area of the (100) exposed facets on the cube's faces.

2.5.3 pH and electrolyte

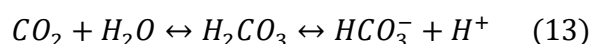
The concentration of Protons (H^+) and Hydroxide ions (OH^-) in the solution can affect the selectivity of the catalytic reduction of CO_2 .⁶¹ On the anode, during catalysis conditions, electrons are transferred to the H_2O molecule. This transfer causes the Oxygen Evolution Reaction (OER) that splits water into H^+ and O_2 .⁶² Those protons are transferred towards the cathode through the H^+ exchange membrane and reacts with the intermediates created by the reduction of CO_2 to form hydrocarbons.⁶³ The reduction of CO_2 and the competitive HER produce OH^- ions over the catalyst surface.⁶⁴



Reaction 11–12: (11) Oxygen Evolution Reaction on the anode and (12) Hydrogen evolution reaction (HER) on the cathode⁶⁴

The generation of OH^- by HER and the reduction of CO_2 increases the local pH around the catalyst's surface. Meaning, a gradient of concentration of OH^- ions at the electrode surface is formed. The RHE, whose scale is pH dependant, is considered with respect to the bulk pH. This pH gradient, or polarization, causes the RHE overpotential in the proximity of the working electrode is usually overestimated⁶¹. This difference in the RHE can be significant enough so that the bulk voltage is not representative of the true activity of the catalyst. In planar polycrystalline copper with a bulk pH of 6.8, the local pH over the catalyst surface starts having a significant difference at biases more cathodic than $-1V$. At this cathodic bias, the pH goes from 6.8 to 8.5 and at more negative potentials like $-1.15 V$, the local pH reaches 9.5.⁶⁵ However, the potential in which the local pH is significant can change depending on the surface area, the catalysts geometry and the bulk's pH.⁶⁶

Moreover, CO_2 's concentration also affects the pH of the solutions as CO_2 also can work as a buffer with a bicarbonate buffering system (**Reaction 13**).⁶⁷ A buffer is a solution of a weak acid and a weak base that keeps the pH at a nearly constant value despite fluctuations of H^+ and OH^- ions. Therefore, if there was a high increase on the system's pH, CO_2 would neutralize it (**Reaction 13**), causing a reduction of the concentration of CO_2 near the surface and thus hampering the CO_2 reduction and favouring HER.⁶⁵



Reaction 13: Buffering reaction Bicarbonate– CO_2

During the electrocatalytic reduction of CO_2 , CO_2 and H^+ are the first reactants to be consumed and therefore, their concentration and reactivity limit the reaction productivity (Limiting reactants). Moreover, the rate of consumption of these limiting reactants is linearly dependent on the current density. Increasing current density decrease the reactant concentration and once reaching the limiting current density the reactants' concentration is negligible. Therefore the limiting current density is the maximum current density in which the reduction can occur and it is dependant on the pH.⁶⁵ Therefore, the reaction productivity can be summarized as a matter of mass transport. Meaning the rate of adsorption of the limiting reactants and the electron transfer rate determine the total velocity of the catalytic reaction.

In a CO_2 saturated solution, the maximum limiting current density and the lowest selectivity toward H_2 are at a pH between 6 and 9 .⁶⁵ Even though this pH region has a relatively low H^+ concentration, the limiting rate step is the mass transfer of CO_2 . This is due to the facilitated mass transport of protons by carbonate thanks to the buffer effect of CO_2 which can easily dissociate to give protons.⁶⁵

To maintain a close to neutral bulk pH, most CO_2 reduction experiments are performed using 0.1 M KHCO_3 electrolyte with 6.8 pH. Multiple researchers have found that a 0.1 M solution was the most efficient for C_2 products, especially ethylene, due to its neutral pH and the low rate of OH^- ions neutralization which raises local pH over the catalyst surface and favours C_2 selectivity.⁴⁵ Solutions with a higher concentration of KHCO_3 show an increase of selectivity toward H_2 and CH_4 . According to Kas et Al.⁶⁸, increasing the concentration of KHCO_3 raises the pH of the bulk electrolyte, which causes a decrease in the surface pH due to the buffering capacity of CO_2 . A low local pH over the catalyst's surface favours HER and the production of C_1 products due to limited CO_2 mass transport.^{65,68}

2.5.4 Copper Nanowires as a catalyst

Copper nanowires are a promising structure for the catalytic reduction of CO_2 . Its structure guarantees a very high surface area, and it is possible to control the exposed facets to focus the selectivity toward ethylene with Cu (100) facets. Moreover, the structure created by nanowires once they are deposited grants the formation of pores. Pores have a higher exposed surface area and a limited mass transport between the inside and outside of the pore. Due to these characteristics, there is a higher production and concentration of OH^- ions inside the pores in comparison with the rest of the surface during catalysis. A higher concentration of OH^- increases the local pH that leads to a better selectivity toward C_2 products.^{45,65}

There are several factors that can influence the selectivity of Cu Nanowire catalysts. As we can see in **Figure 13**, using CuO-derived Cu Nanowires with different lengths for the reduction of CO₂, Ma et al.⁶⁹ discovered a direct relationship between the length of the NW with the selectivity of the catalyst. Longer NWs, 7.3 and 8.1 μm, had approximately a 20% FE towards C₂H₄ whereas shorter nanowires (e.g. 2 μm) produced mainly Hydrogen, CO and Formate at -1.1V vs RHE with a 0.1 M KHCO₃ electrolyte. Even though the ethylene concentration remained similar from the 3 μm toward the 8.1 μm, NWs with longer lengths have a higher selectivity towards other C₂ products like ethane (3% FE at 8.1 μm) or ethanol (5% FE at 8.1 μm).

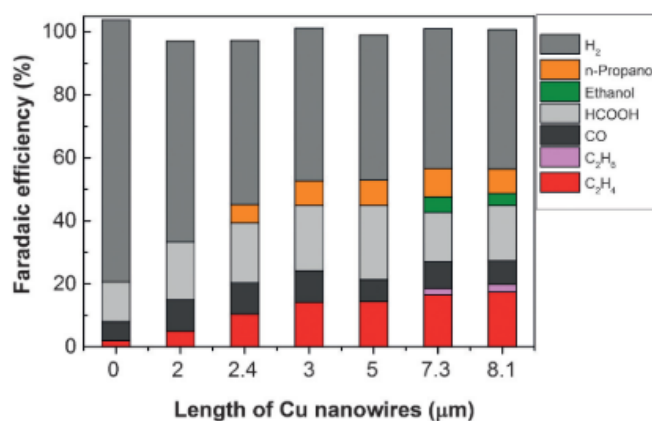


Figure 13: Faradaic efficiency of Copper NW with different lengths from the work of Ma et Al.⁶⁵

The formation of C₂ products on longer NW is attributed to a favourable CO coupling on the catalyst's surface due to the high local pH. The increase of the pH is related to the longitude of the NW as the longer the nanowires are, the higher is the NW density. This higher density is because if you have the same concentration of Cu in the same area, but the NWs are longer, the NWs will have to pile up to equate the Cu concentration, increasing the density and the number of pores. A high nanowire density can hamper the mass transport of the HCO₃⁻ ions from the bulk electrolyte to the catalyst surface and thus limit the neutralization of the OH⁻ ions formed on the catalyst's surface, hence incrementing the local pH.



Figure 14: Structure of the five fold twinned nanowire from the work of Yang et Al.⁶⁷

Facets and grain boundaries also have an impact on the selectivity of the catalyst. For example, Yang et al.⁷⁰ synthesized ultrathin (20 nm) five-fold twinned nanowires (**Figure 14**). The nanowires consisted of five exposed (100) facets forming the length on the nanowire, with highly energetic grain boundaries between each facet and finalized with a spike with five (111) facets. According to the experiments of Hori et al.,²⁴ C₂H₄ should be the main product, as the surface of the nanowires mainly consist of (100) facets. However, Yang et Al. found that the main catalytic product was CH₄ as the selectivity was dominated by the highly active grain boundaries between the (100) facets. Nevertheless, Zhang et Al.²⁷ synthesized nanowires with this same five-fold structure but with a diameter of 50 nm instead of 20 nm. In this diameter range, (100) facets dominate the selectivity providing a 60% FE toward C₂ products without traces of methane or liquid products (like Formic Acid or Ethanol).

2.6 Colloidal synthesis

As shown in **section 2.5**, the selectivity and activity of the electrocatalytic reduction of CO_2 depend on the catalyst's shape, surface structure, size, and composition. In order to study and control all these factors and to be able to optimize the catalyst, it is necessary a synthesis approach that allows the precise tunability of these parameters. Colloidal synthesis has been proven to be a great tool for developing nanostructures with highly controlled characteristics, such as size and shape, and study its effect on electrocatalysis for HER⁷¹, Oxygen evolution⁷² and CO_2 reduction.¹⁷

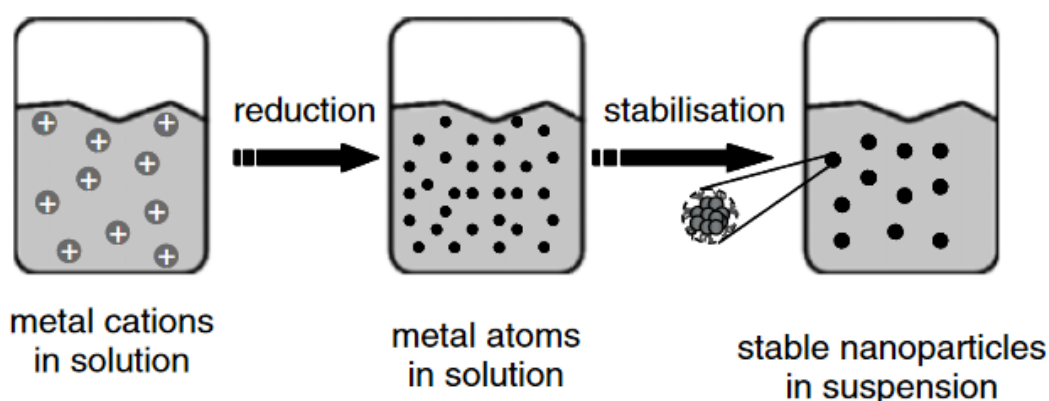


Figure 15: Formation of NPs via reduction of metal salt precursors. Figure extracted from Pachón *et al.*⁷³

Colloidal synthesis is a “bottom–up method” for the formation of nanoparticles, which means that the synthesis is started with a precursor molecule that will release metal atoms into the solution and then, the metal atoms will nucleate and form the nanostructures.⁷⁴ There are different approaches for colloidal syntheses, such as chemical reduction of metal salt precursors, electrochemical synthesis or the controlled decomposition of organometallics. However, in this research we are going to focus only on the chemical reduction approach (**Figure 15**).⁷⁴

Turkevich *et al.* were the first to describe in 1956 the mechanism of the chemical reduction of a salt precursor for the colloidal synthesis of Au nanoparticles as a stepwise process of nucleation–growth–agglomeration.⁷⁵ For this approach is necessary a supersaturated solution of

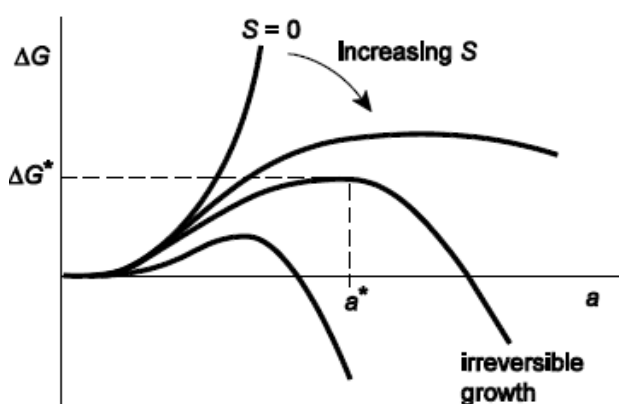


Figure 16: Sketch of the relation between the Gibbs free energy and the radius of the nuclei for the nucleation and growth of a spherical precipitate of radius a in a solution with supersaturation ratio S .

precursor salt, a reducing agent and the presence of a stabilizing agent (ligands or surfactants). A supersaturated solution is a solution that contains more of the maximum amount of solute that is able of being dissolved at that temperature.

The reducing agent reduces the metal ions and releases them into the solution. Spontaneously, as isolated ions are highly energetic and unstable, the metal atoms adhere to each other and form nuclei. The stability of the nuclei depends on the balance between the high energetic atoms on the surface (positive Gibbs free energy) and the stable non-exposed atoms inside the nanostructure (negative Gibbs free energy) as shown in **figure 16**.^{73,74,76} If the spontaneously formed nanoparticles have a radius in which both the positive Gibbs energy of the surface and the negative Gibbs energy of the volume are matched the nuclei is stable and can grow adhering new metal atoms to the nucleus by diffusion (see **Figure 17**).

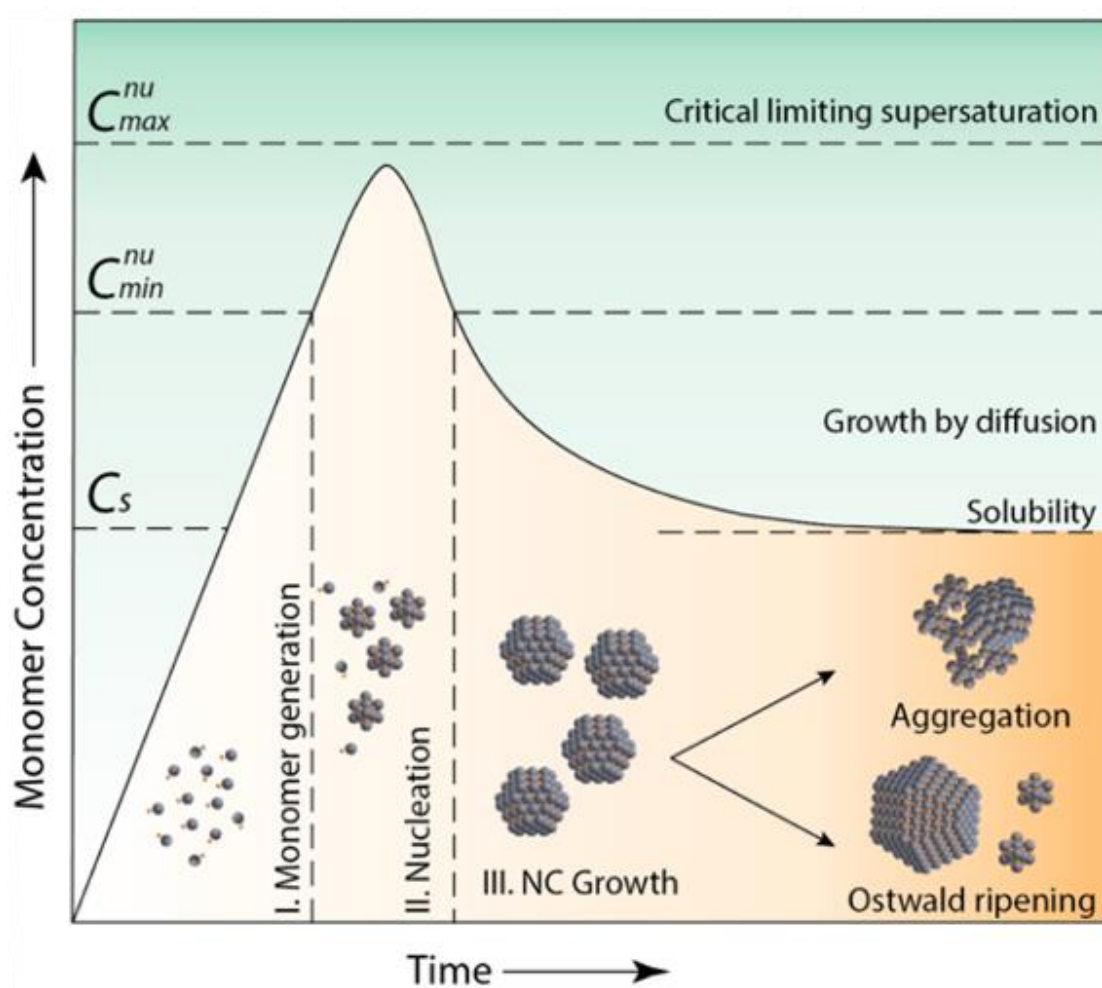


Figure 17: LaMer–Dinegar growth curve depicting the various stages of monomer generation (I), nucleation (II), and growth (III) involved in the solution synthesis. Other processes like aggregation and Ostwald ripening have also been included, which can occur during synthesis. Extracted from Ghosh *Et Al.*⁷⁶

The stabilizing agents, or ligands, partially control the growth, stability, and shape of the newly formed nanostructures. Ligands are ions or molecules which adhere to an atom or the surface of a nucleus and form a coordination complex. Ligands can stabilize nanoparticles in different ways, but in this work we are going to focus in the so-called

steric stabilization. In steric stabilization, the ligands are large organic molecules that adhere to the surface of the nuclei stabilizing the nanoparticle and controlling its growth (look **figure 18**). Ligands control the shape and size of the colloidal nanoparticle due to its preferential adhesion facet and its concentration.

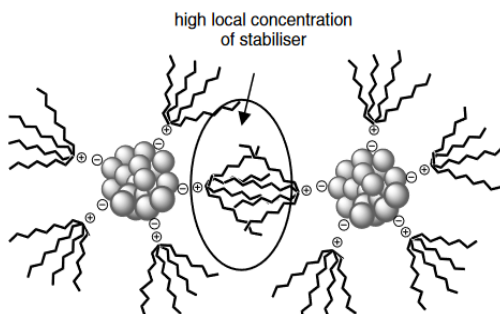


Figure 18: Steric stabilization of metal NP. Figure extracted from Pachón *et Al.*⁷¹

As we can see in **figure 17**, controlling the reaction time is also fundamental during colloidal synthesis.⁷⁶ When monomer's concentration is reduced, and as big NPs are more thermodynamically favourable than smaller NPs, the latter would start to dissolve and be absorbed by the bigger nanoparticles. This process is called Ostwald ripening and it can be observed at the tail of the curve in **figure 17**.

Ostwald ripening can be favourable as it helps the size focusing of the nanoparticles, meaning that as most of the smallest nanoparticles will disappear and be absorbed by the bigger colloids, there would be less disparity of sizes. However, if the process continues for a longer time there would be an aggregation of particles and the formation of bulk macro materials.^{17,76}

The nanoparticle's final shape is determined by a thermodynamical balance between the temperature, reaction time, and ligand concentration. A thermodynamically controlled product is obtained when a system gets sufficient time to let all of the atoms arrive at their final positions to attain the minimum Gibbs free energy for the entire system. Under such circumstances, the shape of the nanoparticles is called the equilibrium shape, which can be achieved by increasing the temperature of the system or giving the reaction sufficiently time to complete.⁷⁶ High temperature and short synthesis time favour the creation of small NP as the high temperature allow the stabilization of smaller critical nuclei and the faster Brownian motion of the nuclei and the ions allow the rapid growth of a higher number of nanoparticles. Large and highly structured nanoparticles as for example nanowires usually need relatively low temperatures and long synthesis time. Low temperature increases the size of the critical nucleus, which lowers the concentration of growing nuclei favouring fewer and larger structures and also the low temperature promotes slower and energetically favorable growth which causes highly ordered structures.

The synthesis of Copper Nanowires with exposed (100) facets has been achieved using different colloidal synthesis.^{28,77-79} In order to synthesize copper NW several factors have to be examined:

- **Salt Source:** CuCl has been showed to be an efficient salt source for the Cu NW formation due to the etching effect of the halide ions. During the nucleation, twin nanoparticles can be formed. Twin particles are nanoparticles with grain boundaries that are shifted as segment of a crystal in which the crystal lattices on each edge are linked across imaginary twin plane by mirror symmetry (**figure 19**). These structures if not controlled can end up with the formation of multifaceted nanoparticles. Introducing halides into the synthesis causes the disintegration of these twinned particles. This disintegration is called the etching effect. Halides interact with the highly active grain boundaries of the twinned structured dissolving them and allowing the growth of single crystals and therefore, helping the growth of single crystal nanowires.^{80,81}

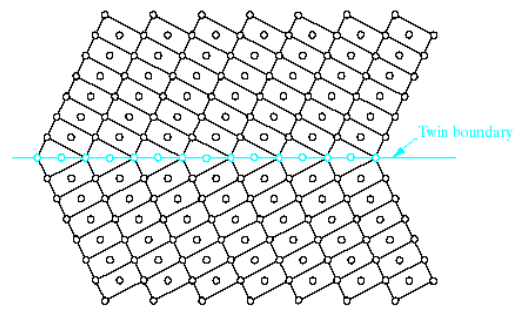


Figure 19: A twin boundary separating 2 crystalline regions that are mirror of each other. Image extracted from the crystallography depparment of MIET university.

- **Ligand:** Oleylamine has a tendency to adsorb over the (100) facets over the (111) planes of Cu crystals.⁷⁰ This is due to the (100) planes being loosely packed, which make bulkier surfactants, like oleylamine able to adhere to its surface. Whereas, the more closely packed (111) facet offers low surface energy sites for the deposition of Cu(0) monomers.^{82,83} As a consequence, Oleylamine can avoid the adhesion of Cu (0) monomers into the (100) facet that would cause an anisotropic growth into the (111) direction.

Using both oleylamine and CuCl with an optimize temperature and synthesis time the production of a Cu nanowire structure with (100) exposed facets should be possible as showed in the next section.

3. Experimental Section

3.1 Chemicals

Colloidal synthesis:

Oleylamine (Olam) (70%), copper acetate (CuOAc) (97%), copper chloride (CuCl) (99%), copper bromide (CuBr) (99%) and Trioctylamine (TOA) (98%) were bought from Sigma Aldrich. 1-Octadecene (90%) was bought from Fisher Scientific.

Solvents:

Isopropanol (99.5%), hexane (99%), anhydrous methanol (99.8%) and anhydrous 1-butanol (99.8%) were bought from Sigma Aldrich.

Electrolyte:

Potassium bicarbonate (KHCO₃) (99.7%) was bought from Sigma Aldrich.

3.2 Colloidal synthesis

3.2.1 Introduction to Schenk line

A Schlenk line, **figure 20**, allows the atmospheric control of the synthesis due to the gas flow management and gas extraction using two separated lines (**1**). One line is under constant nitrogen (N₂) flow and the other is connected to a vacuum pump(**2**). A switch (**3**) allows the change of which channel is connected to a three-neck flask (**3**) where the synthesis is carried out. This connection enables the degassing of the solution under vacuum to extract contaminants as water or oxygen. A condenser tube (**5**) is located between the Schlenk line and the three-neck flask to avoid the vacuum pump's deterioration and the removal of valuable components from the synthesis. Moreover, A cold trap (**6**) filled with liquid nitrogen is located just before the vacuum pump.

All syntheses were carried out in the three-neck flask (**figure 20 b**). With one of the flask's necks connected to the condenser tube, another neck sealed with a septum (**7**), which allows the extraction and addition of chemical components to the synthesis without oxygen contamination, and a third neck connected to a thermocouple (**8**). The metal thermocouple is inserted into a hollow glass tube closed in one side, partially filled with a non-chemically

active solvent (1-Octadecene). This glass tube is immersed into the synthesis solution whose main solvent is 1-Octadecene. This way, as both heat coefficients, the one from the solution and the one from thermocouple, are similar it is possible to control the temperature of the solution. Moreover, As the thermocouple is not in direct contact with the solution due to the glass tube there is no metal contamination in the solution from the metal thermocouple.

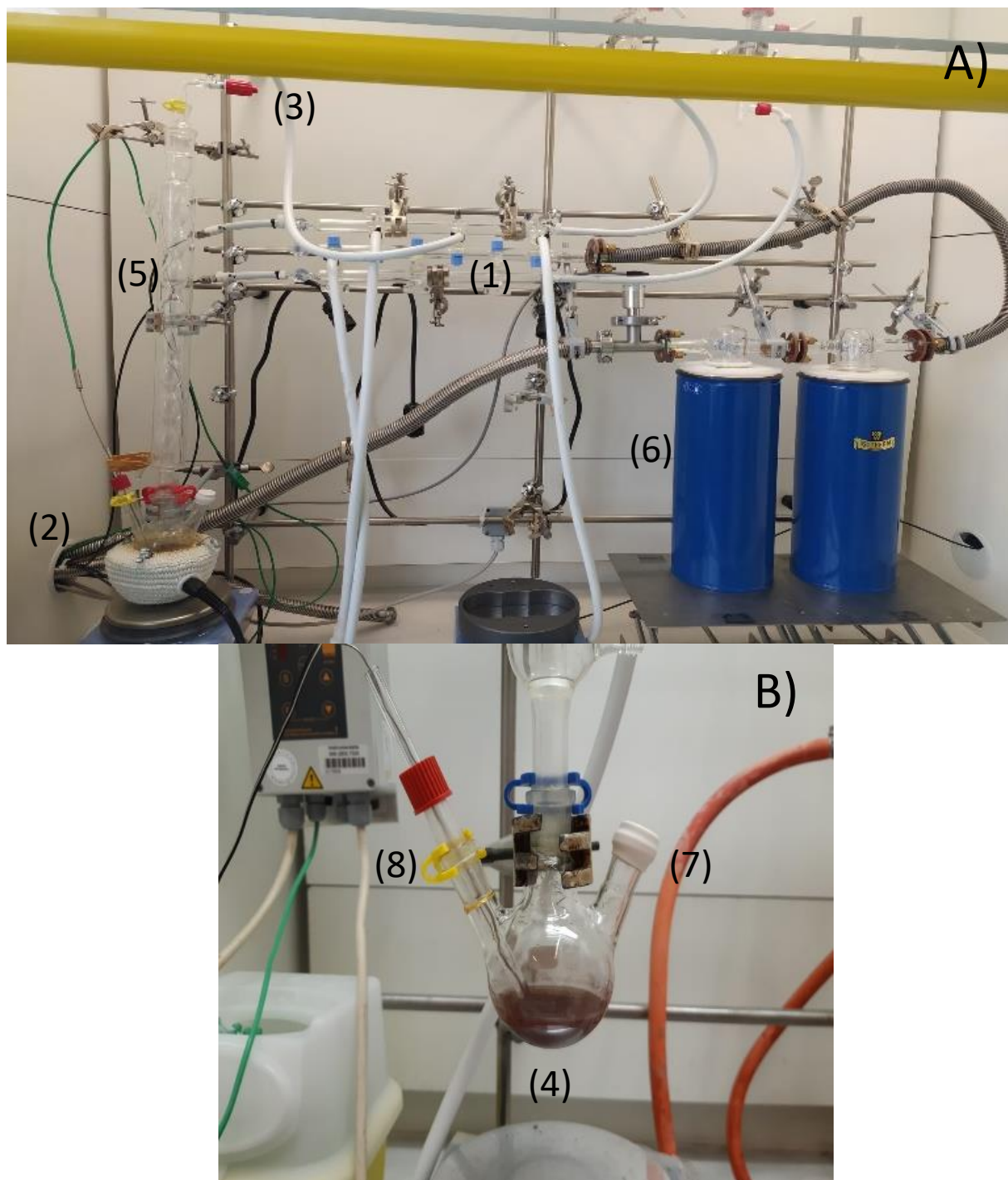


Figure 20: a) Schlenk line connected to a condenser with a double cold trap b) Three Neck flask with a septum and thermocouple.

3.2.2 Synthesis of the catalyst

A typical synthesis would consist of the addition of 1 mmol of CuCl (99 mg), 2.5 mmol of TOA (1 mL), and 10 mL of 1-octadecene in a 100 mL three-neck flask equipped with a glass stir bar. Moreover, depending on the type of catalyst, a different concentration of oleylamine will be added to the colloidal solution.

To synthesize copper nanowires with a diameter of 30 nm with multi-shaped nanoparticles, 6 mmol (2.7 mL) of oleylamine will be added to the solution. For 30 nm copper nanowires with nanopyramids, 8 mmol of oleylamine (3.6 mL) were added. To produce 40 nm nanowires with multi-shaped nanoparticles, 10 mmol (4.5 mL) of oleylamine were added to the solution.

The three-neck flask is connected to a Schenk line, as explained in **section 3.2.1**, to control the reaction atmosphere. The other two necks are sealed by a thermocouple (to control the solution's temperature) and a septum (for adding and extracting materials without oxygen contamination).

Once everything is connected and sealed, the magnetic stirring is initiated, and the gas pump is activated. All the gas is removed from the three-neck flask, and the degassing step is started. Degassing is used to extract contaminants like water from the solution by evaporation. Bubbles will begin to appear in the solution, therefore, the modification of the atmosphere inside the 3-necked flask to vacuum must be done in a stepwise manner to avoid the expulsion of the colloidal solution towards the condenser. The solution is kept at room temperature until there is no more bubble formation.

When the bubbling ceases, the temperature is raised to 100°C. During solution's heating, a close monitoring of the bubble formation is needed to avoid the contamination of the condenser tube. Once 100°C has been reached, the temperature of the solution is kept under vacuum for one hour. During this process, the colour of the solution changed from bright blue at room temperature when copper in solution is Cu^+ , to a dark red at 70°C as copper transition to Cu^0 to finally a transparent yellow colour at 100°C when the Cu^0 is completely dissolved, monoatomic and complexed by Cl^- ions.

After one hour, the flask is filled with nitrogen. The colour of the solution changes from transparent yellow to dark red. Once the atmosphere of the solution is nitrogen, the solution is heated to 180°C. At 140°C the solution became transparent yellow again, and transformed into red at 165°C. This color is maintained until the growth temperature, 180°C, was reached. Once 180°C has been achieved, the solution was kept at this temperature

for three hours, during which the colour of the solution turned bright red as the colloidal NPs were growing.

After three hours of growth, the solution was rapidly cooled using an air gun. When the solution reached room temperature, the colloidal solution was extracted using a syringe, avoiding any oxygen contamination. Next, the extracted liquid was injected into two 40 mL vials with a screw cap with a septum and a nitrogen atmosphere. Afterwards, the same volume of antisolvent as the extracted colloidal solution and 1 mL of solvent (Hexane) were added into the vials. The antisolvent can be isopropanol or a 1:1 proportion of methanol and 1-butanol.

Once the solution in the vial consists of a 1:1 ratio of colloidal solution and antisolvent with 1 mL of hexane, the vial is centrifuged at 3500 rpm for 5 minutes. After centrifugation, the opaque, homogeneous solution inside the vial should have transformed in a two-phase solution with a red precipitate at the bottom and a transparent red supernatant. Next, the supernatant is extracted inside a glove box with an inner atmosphere to avoid any contamination, and 4 ml of hexane were added to the vial. Finally, the vials were sealed using teflon tape to prevent the evaporation of the solvent and stored inside the glovebox.

3.3 Size selective precipitation

Size-selective precipitation is a common technique used for separating polydisperse nanoparticles into fractions with narrower size distributions.⁸⁴ The colloidal particle's rate of deposition under gravity in a suspension solution depends on several factors, such as the size of the nanoparticle, the viscosity of the medium or the buoyancy mass of the nanoparticles.⁸⁵

$$f = 8\pi\eta R^3 \quad (6)$$

$$u = \frac{\Delta mg}{f} = \frac{2(\delta_p - \delta_{solv})}{9\eta} R^2 \quad (7)$$

Where:

f = Stokes friction factor (N)

η = Dynamic viscosity (Pa.s)

R = radius of the nanoparticle (m)

Δm = buoyancy mass of the nanoparticle (Kg)

δ_p = Density of the nanoparticle ($\frac{Kg}{m^3}$)

δ_{solv} = Density of the solvent ($\frac{Kg}{m^3}$)

Equation 6–7

As indicated in **equation 7**, small nanoparticles will remain in suspension longer than larger nanoparticles. As the Stokes friction factor (f) of the NP is inversely proportional to its cubic radius, the NP's deposition rate is therefore proportional to the cubic of its radius. Although the equation is for ideal spherical nanoparticles, it can show how with the extreme buoyancy mass difference between the nanoparticles and the nanowires the deposition time for the latter would be considerably shorter. So, it is possible to use this deposition time difference to separate the different types of colloidal nanoparticles.

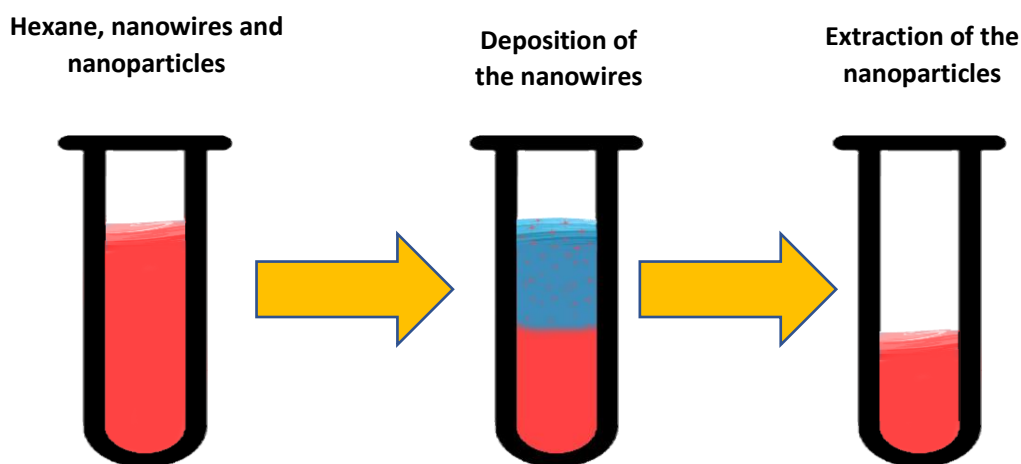


Figure 21: Scheme of the Reduction of nanoparticle loading

As shown in **figure 21**, after sonicating the colloidal solution of NWs and NPs for an hour, leave the suspension static until a two-phase system is formed. The two-phase system consists of a solid phase of nanowires deposited at the bottom of the vial and a reddish but transparent liquid phase formed by the Hexane and nanoparticles. Remove the liquid phase and refill with more Hexane. Repeat the process without sonification 3 times or until the liquid is completely transparent after the nanowire deposition.

3.4 UV-vis Absorption spectroscopy

The absorption spectra were measured using a light source between 400 and 800 nm on a UV-Vis Cary-60 from Agilent Technologies. We introduce 0.2 mL of Nanowire colloidal solution and 1.8 mL of hexane inside a 2 mL cuvette with a screwcap. To avoid oxygen contamination and the possible oxidation and deformation of the colloidal solution all samples were prepared inside a glove box with an inert N_2 atmosphere and the cuvettes were closed with a screwcap.

3.5 X-Ray diffraction

XRD measurements were performed on a Bruker D2 Phaser using Co-K α radiation with a wavelength of 1.79026 Å. Scans were performed in the angular range of $40^\circ < 2\theta < 70^\circ$, with 0.5 seconds scanning times and an angle increment of 0.1° .

3.6 Electrode preparation

The colloidal nanoparticles were deposited onto 1 cm² square pieces of glassy carbon electrodes. To avoid external contamination from the atmosphere and previous experiments, it is necessary to clean the glassy carbon electrodes prior to the catalyst deposition. First, the glassy carbon were polished using a polishing powder composed of 5 μm diamonds. Both sides of the glassy carbon were polished for 30 to 60 seconds. After polishing, the glassy carbon electrodes were submerged in a vial filled with ethanol and sonicated for 30 minutes. Next, the ethanol was extracted and the vial was filled with acetone and sonicated for 30 minutes. Finally, the acetone was removed and the vial was refilled with miliQ water and sonicate for 30 minutes.

Before the deposition of the catalyst's nanoparticles, half of the area of both sides of the glassy carbon electrodes' was covered with Teflon tape to guarantee a clean electric contact once it is in the electrocatalytic cell.

The deposition of the catalyst over the glassy carbon electrode was made via drop-casting (**figure 22**). 30 μL of the colloidal solution was deposited over one face of the glassy carbon as a droplet inside a glove box with an inert atmosphere. If, after the drop-casting, the entire exposed area of the glassy carbon is not entirely covered by the catalyst, repeat the drop-casting using 5 μL of solution until the surface is all covered. Once the drop-casting is finished, the electrodes remain inside the glovebox overnight to dry the solvent (hexane).⁸⁶

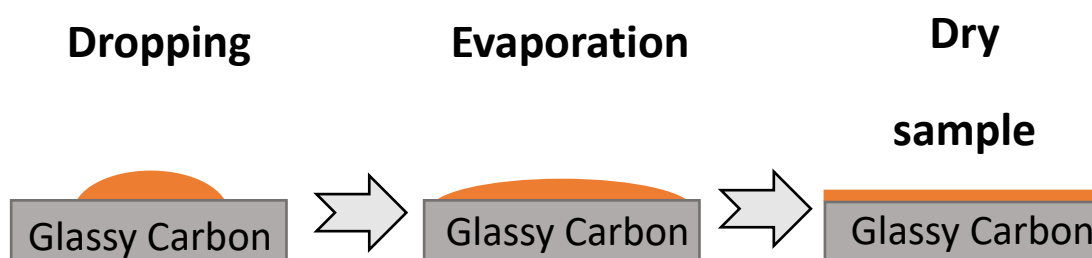


Figure 22: Scheme of the drop-casting process.

After drying and before inserting the electrode in the electrocatalytic cell, it is necessary to eliminate the ligands excess over the electrode. This excess of ligands reduces the conductivity of the electrode and the accessibility of CO₂ to the active sites. To eliminate it, just before the electrochemical measurements, clean the surface of the glassy carbon using a 5 mL syringe filled with electrolyte (0,1 M KHCO₃).

3.7 Electrochemical measurements

All the electrochemical measurements were performed on a standard three-electrode system in a two-compartment H-cell separated by a proton exchange membrane (Nafion 117, Dupont). with an Ag/AgCl reference electrode and a Platinum (Pt) counter electrode, and glass stir in the cathode (see **figure 5, Section 2.2**). As an electrolyte, a solution of 0.1 M of KHCO₃ in miliQ water has been used for all experiments.

To saturate the electrolyte with CO₂, a constant gas flow of 20 mL/min has been used on the cathode under stirring for 30 minutes.

The activity measurements were carried out with a constant glass flow of 10 mL/min of CO₂ and a 0.2 mL/min flow of argon under constant stirring. In all samples, the first electrochemical experiment has been a linear sweep between 0.3 V and -1.5 V Vs RHE for ligand removal and ensuring electrical contact. The second experiment was a chronoamperometry where the bias of the working electrode is set constant. All samples have been tested in a voltage range of -1.1 V to -1.3 V vs RHE. In voltages less cathodic than -1.1 V, close to zero CO₂ reduction products were detected and the production was mostly H₂ in all tested catalyst.

To examine the gas products created during the catalytic activity, the cell is connected to a gas chromatograph. The gas sample is analyzed by the chromatograph in separated injections every four minutes and the different products are separated and catalogued in peaks by their retention time with the stationary phase of the chromatograph. The area of these peaks after calibration gives information about the quantity of product liberated and it is possible to deduce its Faradaic efficiency using **equation 8, 9 and 10** and considering than in standard conditions 1 mol has a volume of 24041 L.

$$ppm = \text{Calibrated SCCM} * \text{peak Area} \quad (8)$$

$$\text{partial current density} = ppm * \text{Flow} * ne * F * \frac{1 \text{ ml}}{1000 \text{ L}} * \frac{1 \text{ min}}{60 \text{ s}} * \frac{1 \text{ mol}}{24041 \text{ L}} \quad (9)$$

$$FE = \frac{\text{Partial current density}}{\text{Current}} * 100 \quad (10)$$

Where:

$ppm = \text{Parts per million of the product}$

$\text{Calibrated SCCM} = \text{Standar Cubic Centimeters per Minute, the volumetric flow of the product (m}^3\text{/min)}$

$\text{Partial current density} = \text{Current aimed to species production (A)}$

$NE = \text{Number of electrons per product (electrons)}$

$F = \text{Faraday's constant 96485 (C/mol)}$

$\text{Flow} = \text{Flow of CO}_2 \text{ (mL/min)}$

Equation 8–10

3.8 NMR

In order to determine the liquid product, ¹H nuclear magnetic resonance (NMR) spectroscopy was used in the water suppression mode. 0.5 mL of electrolyte solution was removed after activity and mixed with 0.1 mL of deuterated water (D₂O) as the lock solvent. As an internal reference, 0.05 μL of dimethyl sulfoxide (DMSO) was employed. With the concentration gathered using NMR it is possible to deduce the average faradaic efficiency of the sample using **equation 11**:

$$FE = \frac{\left(\frac{\text{Peak Area} * 42 * 4.02}{\text{Current}} \right)}{NI} * 100 \quad (11)$$

Where:

Peak area= Area of the NMR's peak

Current: Average current of the catalysis (mA)

NI= Number of injections

FE= Faradaic efficiency (%)

Equation 11

3.9 Raman spectroscopy

Raman spectroscopy is a light scattering technique which allows the characterization of the sample during operando conditions, giving us information about the specific vibrations of the molecular bonds on the catalyst surface.

The sample is immersed in the KHCO_3 electrolyte that is supersaturated with CO_2 and connected to the system via a metallic crocodile. A Platinum counter electrode and an Ag/AgCl reference electrode are also submerged in the electrolyte. The light source, a laser of 532 nm wavelength, is aimed to the sample using an 40X optical microscope.

Two types of tests will be carried out on the catalyst sample. The first test will use a constant voltage with -0.4 V and -1.1 V vs RHE for 30 seconds, three times. The other experiment is another constant voltage at -1.1 V vs RHE for 30 seconds, three times after doing a cyclic voltammetric test between 0.6 and -0.9 V with 1 mV steps and a 0.5 seconds pause between steps to the catalyst. In both experiments, we will detect all vibrations between the frequencies 0 and 2200cm^{-1} .

3.10 Electron microscopy

The imaging of the catalyst pre activity was done using a Transmission Electron Microscope (TEM) Thermo Fisher Tecnai 20 and the HRTEM (High Resolution Transmission Electron Microscopy) images were done using a TFS Talos F200X.

The imaging of the catalyst post activity was done using a Secondary Electron Microscope (SEM), the TFS Helios Nanolab G3 which is able of elemental mapping using Energy Dispersive X-ray Spectroscopy (EDX).

4. Results and discussion

4.1 Synthesis of the Catalysts

4.1.1 30 nm nanowires with a secondary nucleation of multi-shaped nanoparticles

Using a ratio of 1 mmol CuCl, 2.5 mmol of TOA and 6 mmol of Oleylamine with the standard synthesis procedure, a colloidal solution of nanowires with a length of several microns and a diameter of 29.7 ± 4.3 nm is produced. Along with the nanowires, there is a secondary nucleation of nanoparticles with different shapes and a mean diameter of 121.7 ± 13.6 nm (**Figure 22 and annex B**). To determine the size distribution for each type of nanostructure, we have measured the sizes of 25 different examples of that nanostructure in different TEM images, and we calculated the average diameter and the standard deviation.

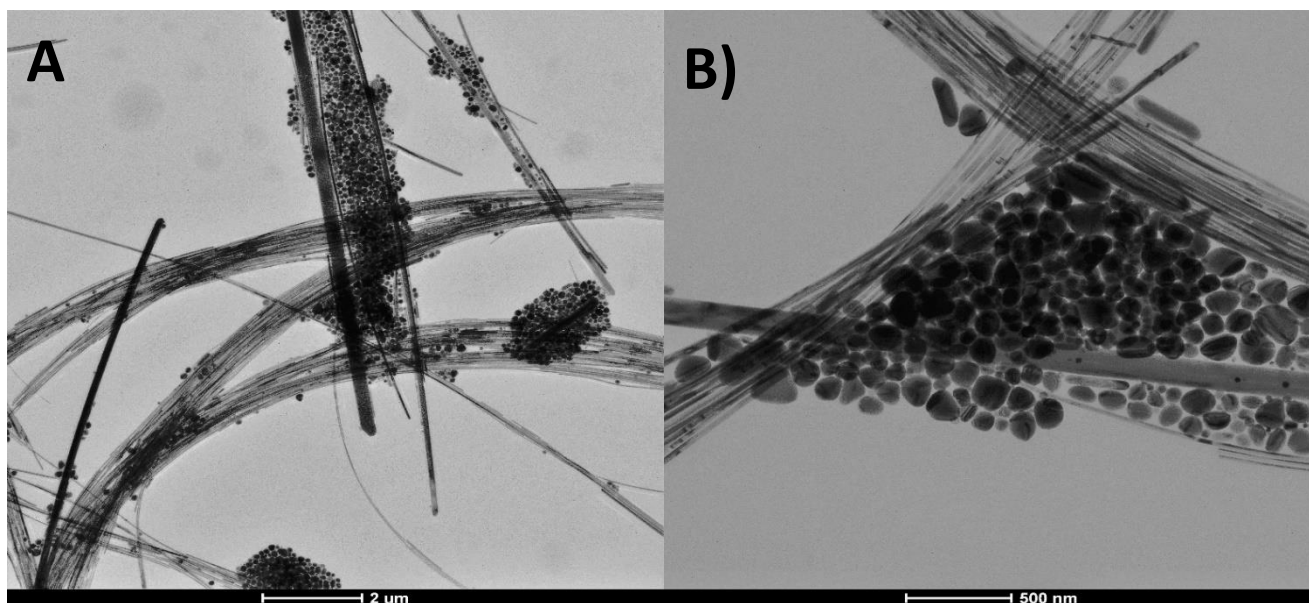


Figure 22: TEM image of 30 nm nanowires with a secondary nucleation of multi-shaped nanoparticles

There are two types of nanowires in the solution. First, thin nanowires, which are the main component of the colloidal solution, with a diameter of approximately 30 nm. They can be found principally in clusters or bundles of nanowires. These bundles are formed by several nanowires in contact between each other due to the interaction forces between colloidal nanoparticles, like Van der Waals forces, and the tendency to reduce the exposed surface area. The second type of nanowire are the thick NWs. The size focusing of this type of nanowires is much lower than the thin ones and they can have a diameter ranging from 100 nm to 200 nm. Thick nanowires are found in isolation without forming any type of bundle

due to the lower energy of its exposed surface. However, most of the nanoparticles of the secondary nucleation can be found around these larger nanowires.

As shown in the work of Zhang *et Al.*²⁷, there is going to be a significant disparity between the selectivity and activity of the thin nanowires (30 nm) and the thicker nanowires (>100 nm). However, there are considerably more thin nanowires than thick ones and therefore, the total catalyst's surface area and the active sites will be mainly provided by the thin nanowires.

Focusing on the nanoparticles, in **figure 22 b)**, contrast lines can be found on the surface of most of the nanoparticles. These lines can be attributed to grain boundaries.

4.1.2 30 nm Nanowires with a secondary nucleation of nanopyramids

Increasing the Oleylamine concentration from 6 to 8 mmol in the standard synthesis does not directly impact the diameter of the nanowires. The diameter of the Cu NWs went from 29.7 ± 4.3 nm to 31.1 ± 5.3 nm, so there is an increase in size, but it is within the standard deviation. Nanowires are also aggregated in bundles and nanoparticles can be found on spots with a high concentration of NWs or around NWs with a larger diameter. On the other hand, as shown in **figure 23 b)**, increasing the Oleylamine concentration has an impact on the size and shape of the secondary nucleation. At first glance, it appears to be two types of nanoparticles, nanocubes with an average size of 97.93 ± 13.8 nm and nanoparticles with triangular shapes. Both types of nanoparticles show contrast lines that cross their surface and that are attributed to grain boundaries. The hypothesis was that both types of nanoparticles are the same square-based nanopyramids. The NPs shape difference observed in the TEM images are due to the different angles at which the NPs are deposited.

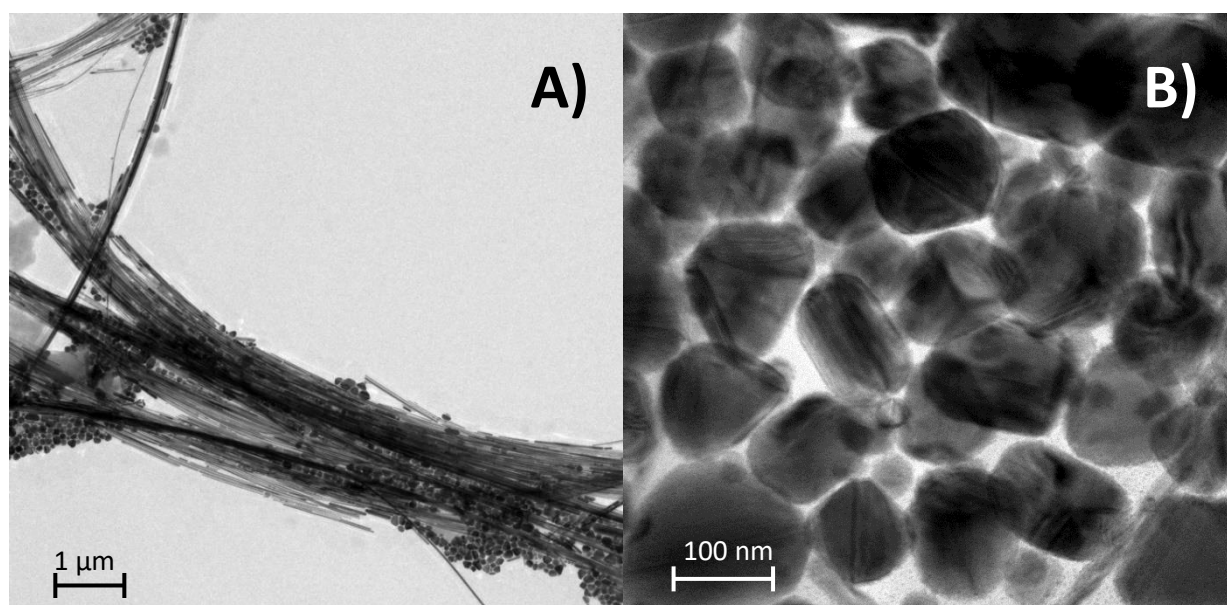


Figure 23: A) :TEM image of 30 nm nanowires with a secondary nucleation of nanopyramids B) HRTEM image of the nanopyramids

An HRTEM analysis of the secondary nucleation is shown in **figure 24 and anex.** With the focus of the HRTEM fixed in a nanocube, the angle of observation has been slightly modified to observe different 2-dimensional images of the 3-dimensional nanoparticle. In **figure 24 a)** the nanoparticle has the shape of a nanocube, in **figure 24 b)** the shape is completely triangular and in **figure 24 c)** the difference of contrast in the nanoparticle implies a pyramidal shape. However, without further analysis, it is impossible to guarantee that all the nanocubes or triangular shapes observed in the sample are nanopyramids. The difference in the shape and the size of the nanoparticles can be attributed to different angles but also to different stages of colloidal growth. Nevertheless, at least a significant percentage of the secondary nucleation would have a nanopyramid shape and therefore have an impact on the final selectivity.

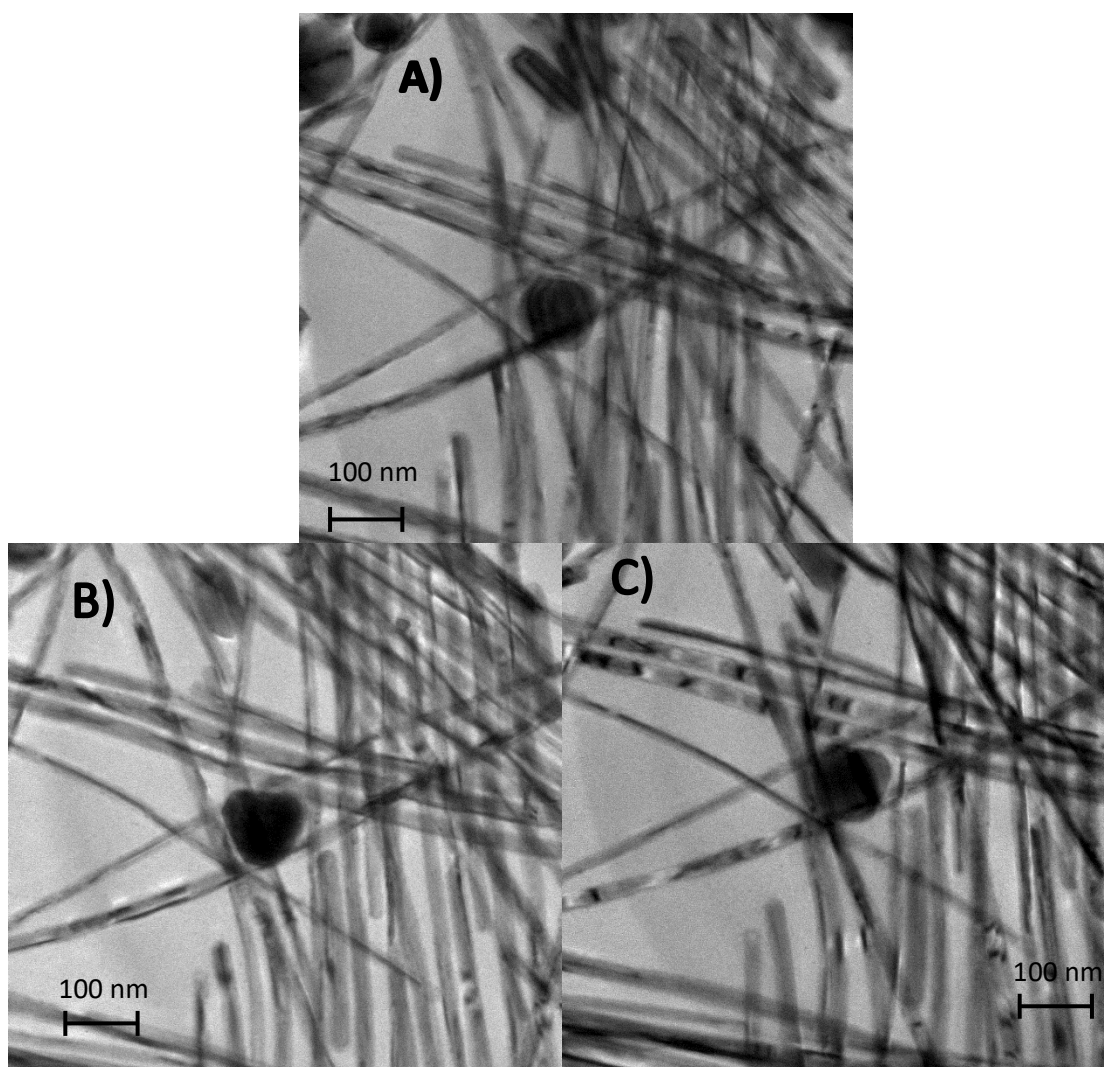


Figure 24: HRTEM images of the same nanoparticle at different angles, showing a) Nanocube b) Triangle c) Cone

The pyramidal shape of the secondary nucleation is attributed to two different factors. First, the increase of ligand concentration, from 6 mmol of Oleylamine to 8 mmol ensures better coverage of the growing secondary nucleation with ligands. The nanowires of both syntheses, 6 mmol of oleylamine and 8 mmol of oleylamine. have the same diameter, similar longitudes, and exposed facets (100) and a (111) preferred growth orientation (see **XRD analysis** in **section 4.3.1**). The difference is in the size and structure of the secondary nucleation. This means that the amount of Oleylamine that coats the surface of the nanowires is relatively the same in both synthesis, and therefore, the excess of ligands in the 8 mmol syntheses is interacting with the secondary nucleation. The second factor is that Oleylamine can also work as a reducing agent. The increment in the ligand concentration can partially reduce the CuCl salt, therefore can provide an increase in the number of critical nuclei and a more homogeneous growth.

4.1.3 40 nm Nanowires with a secondary nucleation of multi-shaped nanoparticles

Increasing the Oleylamine concentration to 10 mmol in the standard synthesis increases the size of the nanowires from 30 nm to an average diameter of 40.27 ± 5.31 . The size dispersion of the NW has risen slightly as the number of thicker nanowires has grown significantly. The NWs are no longer clustered into bundles, and if they are aggregated, they can be found in clusters of a few nanowires. The smaller agglomeration of NWs increases the exposed surface area and, consequently, increases the number of active sites. Also, in some NWs, grain boundaries have appeared where the angle of growth of the NW changes, adding corner sites (**annex D**) which create highly catalytically active irregularities over the catalyst's surface (**Section 2.5.2**).

Focusing on the secondary nucleation, we can still observe the presence of triangular shapes. However, the nanocubes have disappeared from the solution or at least considerably reduced their concentration in the explored areas. The triangular shapes and the contrast lines of the grain boundaries within the nanoparticles still imply a pyramidal structure, but the cubic base has not been encountered on the analyzed samples. It is not only the shape dispersion that has drastically increased, but also the size dispersion of the NPs with an average size 165 ± 49.5 nm.

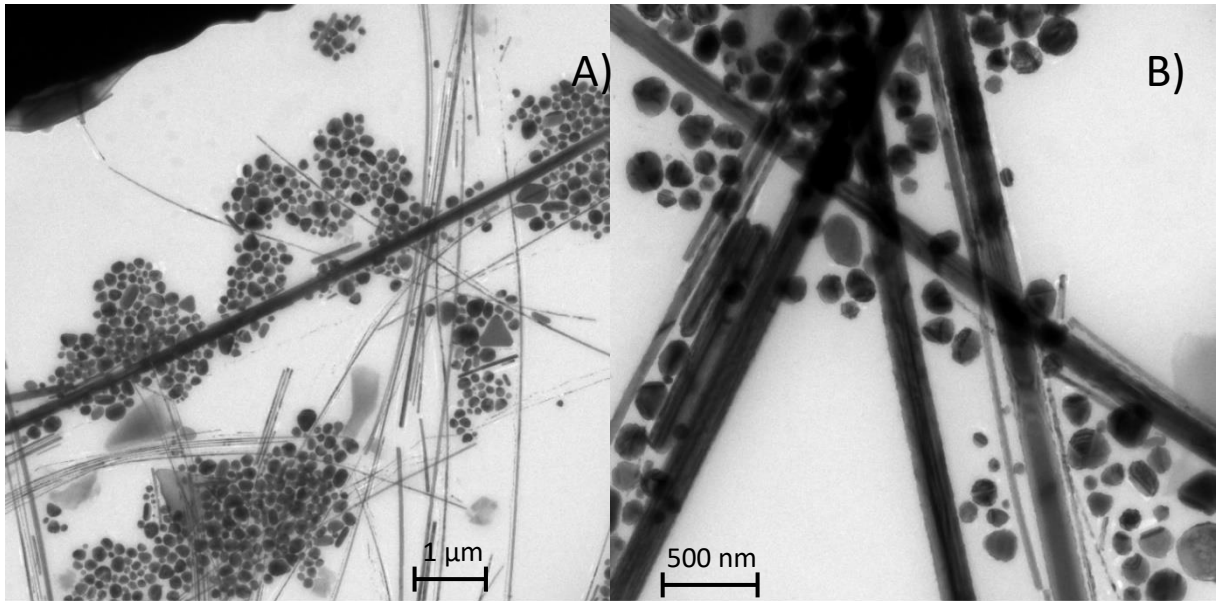


Figure 25 : TEM image of 30 nm nanowires with a secondary nucleation of multi-shaped nanoparticles

Furthermore, this secondary nucleation is not as clustered in the nanowires as in the previous synthesis (**Figure 22 and 23**). In the samples with 6 and 8 mmol of oleylamine, nanoparticles can only be found adhered to thicker nanowires or to spots with a high concentration of NWs. However, in the 10 mmol sample, the NPs are bigger and therefore more stable (lower surface energy), thus the NPs aggregation is lower than in the synthesis with 6 and 8 mmol of OLAM (**figures 23 and 24**).

Oleylamine has a preferential attachment towards (100) however, as shown in the work of Huaman *et al.*,⁸⁰ when there is an excess of ligand it will start attaching to less preferential facets like (110) or even (111), as the proportion between (100) facets and ligands decreases, it is more thermodynamically favourable to attach to other facets than not attaching.⁸⁰ As more facets are being covered by the ligands, the growth of the NWs can be stopped as the oleylamine is covering the (110) and (111) facets, making the NWs shorter and thicker, as shown in Huaman *et al.*, and may be the reason of the change in growth direction inside the nanowires.

4.2 Size-selective precipitation

Using the size-selective precipitation method, we have reduced the concentration of the secondary nucleation loading from the three different catalyst samples.

UV–Absorption of the extracted liquid during size selective precipitation

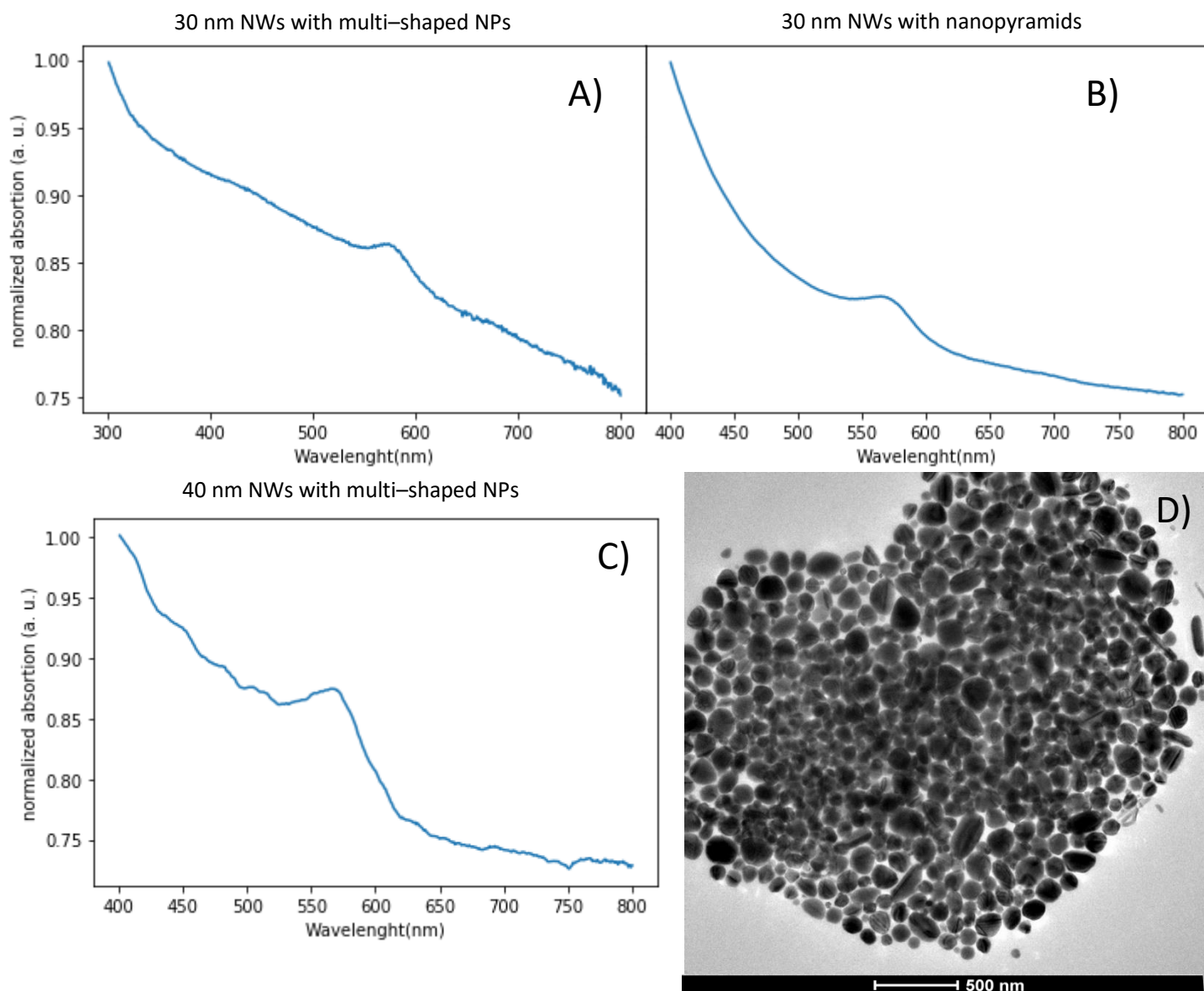


Figure 26: A) Absorption spectrum from the extracted liquid during size selective precipitation of the 30 nm NWs with a secondary nucleation of multi-shaped NPs. B) Absorption spectrum from the extracted liquid during size selective precipitation of the 30 nm NWs with a secondary nucleation of nanopyramids C) Absorption spectrum from the extracted liquid during size selective precipitation of the 40 nm NWs with a secondary nucleation of multi-shaped NPs D) TEM image of the extracted liquid during size selective precipitation of the 30 nm NWs with a secondary nucleation of multi-shaped NPs without presence of NWs

As shown in **figure 26**, we have analyzed the extracted liquid from the size-selective precipitation using TEM for local imaging and UV–vis spectroscopy. UV-vis absorbance experiment has been done on the pristine samples of all catalysts before any size-selective

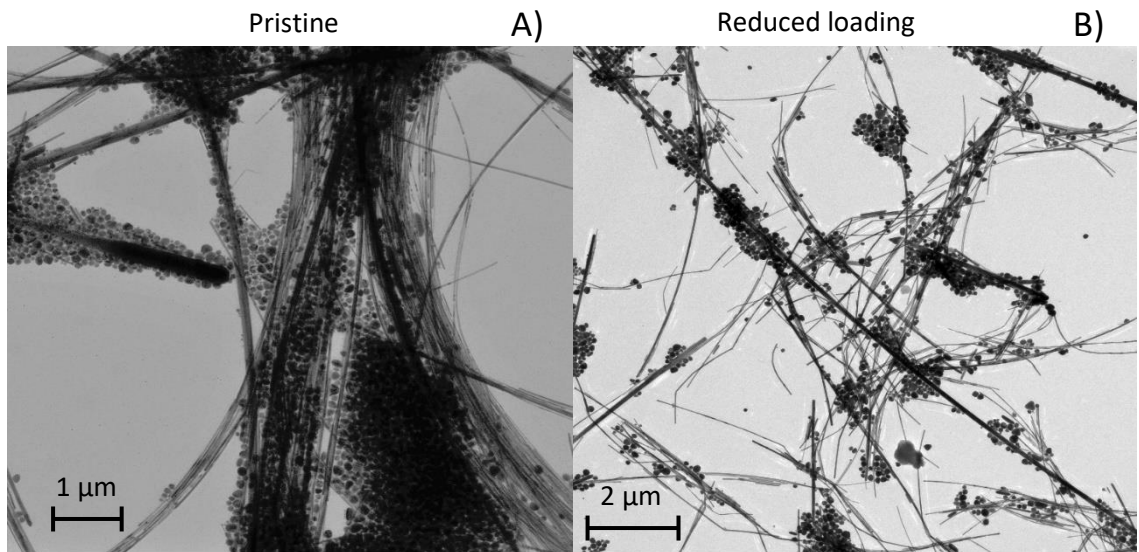
precipitation process has been done (**Annex**). However, the absorbance experiments of the pristine samples are irreproducible as the absorbance of the sample constantly fluctuates during our experiments. This fluctuation has been attributed to the fast deposition time of the nanowires. Therefore, experiments without diluting the sample in hexane in a cuvette for absorption should be done in the future. However, as shown in **figure 26** , even though after size-selective precipitation the NWs still show a fluctuating absorption (**annex E**), the extracted liquid during the process has a clear absorption peak at **A**) and **D**) 572 nm and **C**) 575 nm which correspond with the absorption peak of Cu nanoparticles. This absorption range agrees with the values from the plasmon resonance of Cu nanoparticles (570–590 nm).^{87,88,89} Moreover, local analysis of the samples using TEM (**figure 26 D**) was done in the extracted liquid during size-selective precipitation of the 30 nm NWs with multi-shaped NPs where only NPs were found during imaging. Therefore, combining the UV-vis absorbance spectroscopy of the extracted liquid during size-selective precipitation and the TEM analysis, we can confirm a reduction of the NPs concentration in all samples after the size-selective precipitation.

In **figure 27**, we can see the local TEM imaging of all catalysts before and after the size-selective precipitation process. In the case of 30 nm NW with multi-shaped NPs , and 30 nm NWs with nanopyramids, we can observe that the nanowires bundles have dispersed. Most nanowires were found in isolation or in small groups of nanowires, exposing a larger surface area. The concentration of nanoparticles has visibly decreased, at least in the analyzed area, and they are distributed more evenly throughout the sample. It is possible to still find agglomerates of nanoparticles, but most of them are distributed over the thicker nanowires.

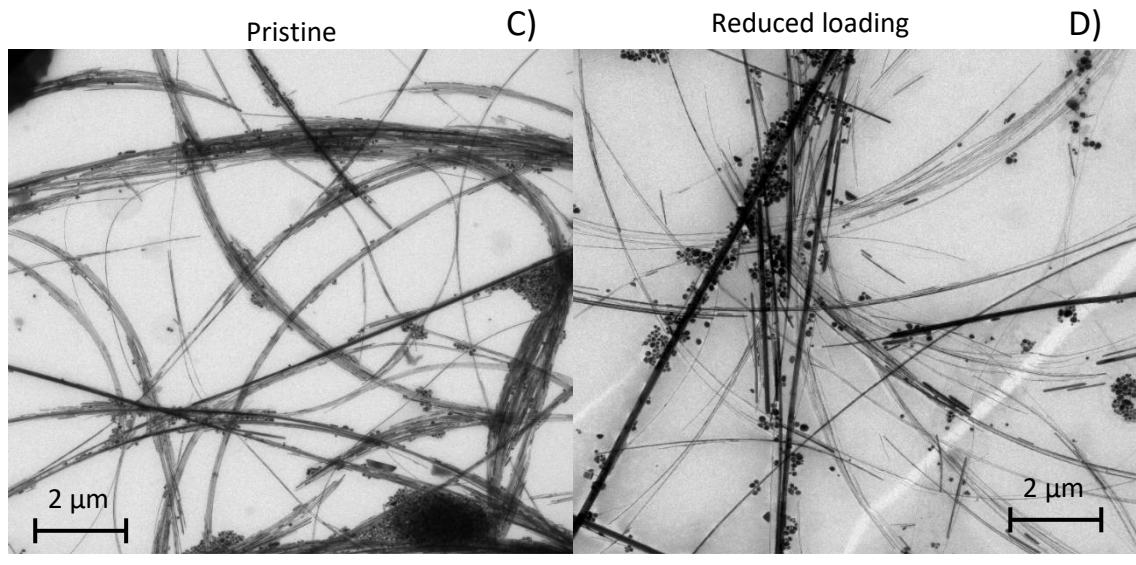
In the case of 40 nm nanowires (**figure 27 E,F**), the difference in the secondary nucleation concentration between the pristine and reduced loading samples is significantly more evident than in the other two catalysts samples. Agglomerations of nanoparticles have decreased in the analyzed area, and most nanowires can be encountered in isolation.

The repetition of the cleaning process has not shown a distinctly change in the concentration of nanoparticles, and the concentration of NPs found on the extracted liquid were almost negligible. More experiments should be done in the future aiming for the complete extraction of the secondary nucleation. The electrophoresis technique could be a possible approach for separating the nanowires and the secondary nucleation. Electrophoresis allows the nanoparticles' separation by their migration velocity inside a gel medium in an electric field.⁹⁰

30 nm Nanowires with multi-shaped nanoparticles



30 nm Nanowires with nanopyramids



40 nm Nanowires with multi-shaped nanoparticles

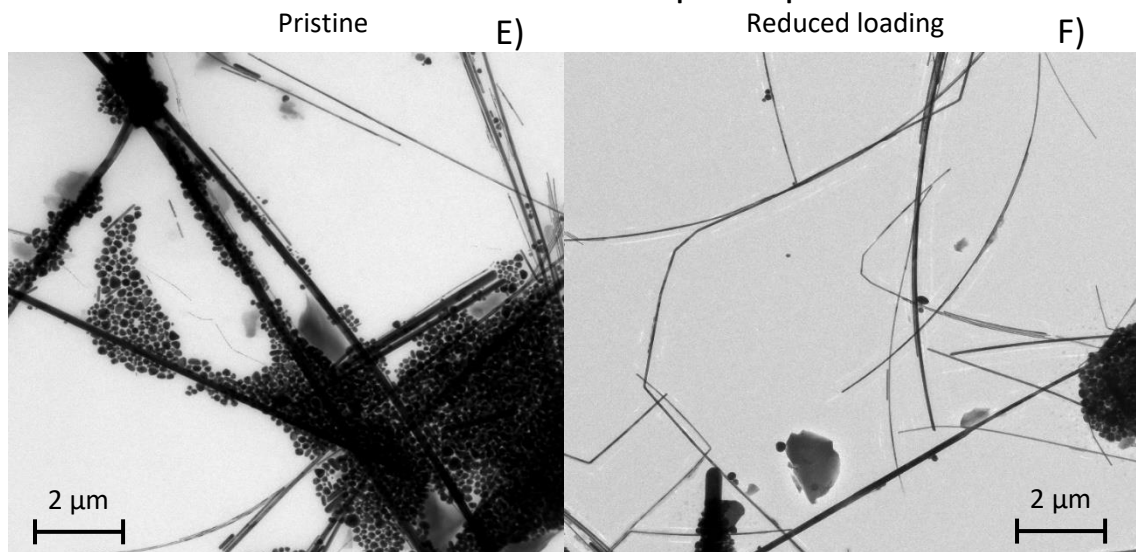


Figure 27: TEM images of A) Pristine sample and B) Reduced Loading sample of 30 nm nanowires with multi-shaped nanoparticles. C) Pristine sample and D) Reduced Loading sample of 30 nm Nanowires with nanopyramids. E) Pristine sample and F) Reduced Loading sample of 40 nm nanowires with multi-shaped nanoparticles

4.3 Characterization preactivity

4.3.1 XRD

In **figure 28** it is showed the normalized XRD diffractogram of the pristine samples of the 40 nm NWs with multi-shaped NPs, the 30 nm NWs with nanopyramids and the 30 nm NWs with multi-shaped NPs.

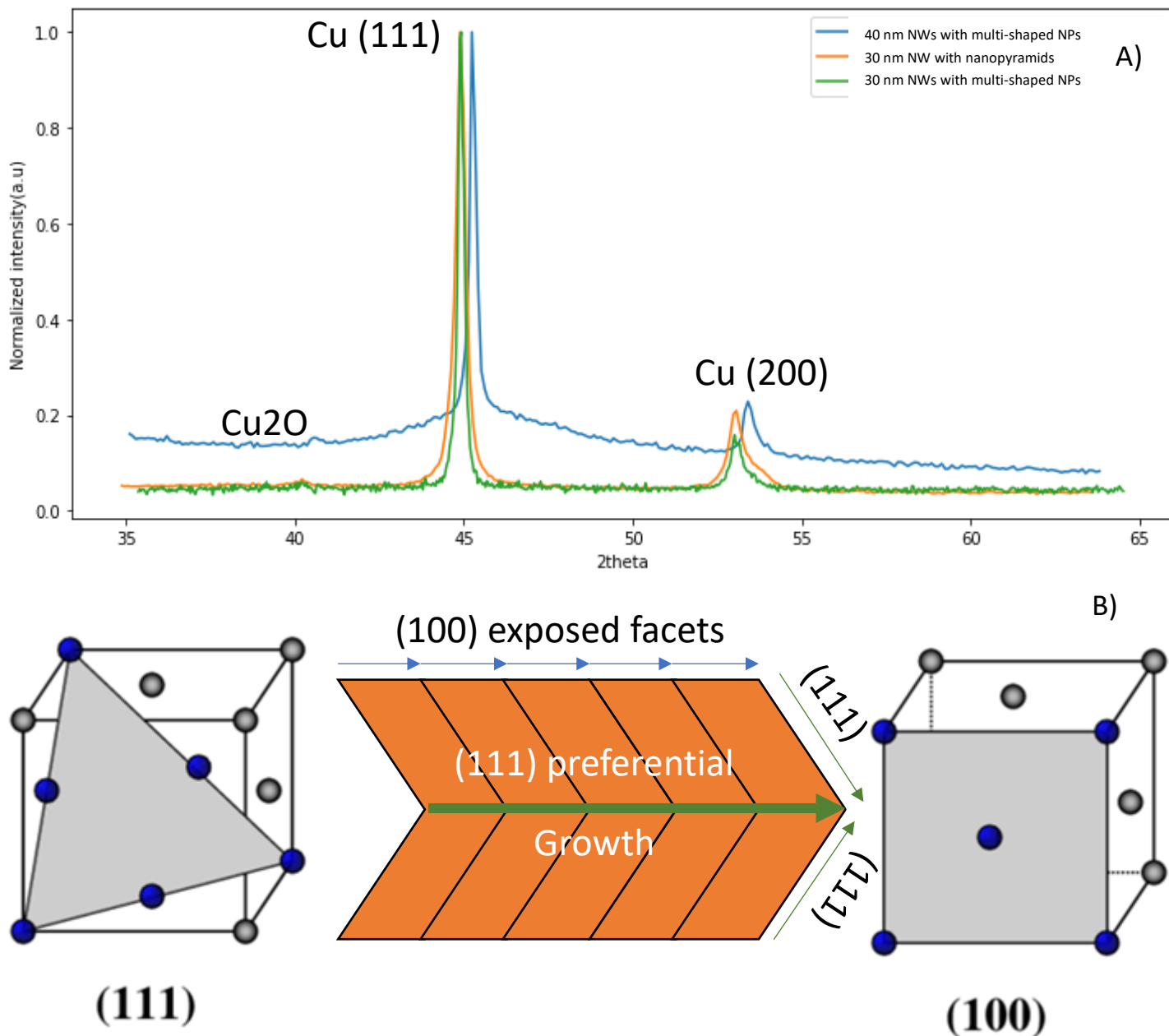


Figure 28: A) normalized XRD spectrum of the pristine samples of the 40 nm NWs with multi-shaped NPs, the 30 nm NWs with nanopyramids and the 30 nm NWs with multi-shaped NPs. B) Growth mechanism

Three reflections appear on all catalyst samples. One reflection on around 45°, which corresponds to the (111) plane of the copper cell, around 53° which corresponds to the (200) facet of the copper cell and one close to 40° which corresponds with Cu₂O.^{16,91,92}

The XRD pattern confirms a face-centered cubic structure for the nanoparticles and the nanowires with a (200) inter-planar distance.^{27,70} The growth of the NWs in the (111) direction will produced (as seen in **figure 28 B**) the exposition of the (100) facets over the NWs surface until the tip of the NW where we could find (111) facets. However, the NPs as the growth in the (111) direction is shorter, most of its exposed facets would be (111) with (100) grain boundaries.

The maximum of the reflections for the 30 nm NWs with multi-shaped NPs and the 30 nm NWs with nanopyrramids are located in the same 2θ angle. Moreover the reflection of the catalyst with nanopyrramids is wider than the one with multi-shaped NPs . According to the Debye-Scherrer formula, shown in equation 12, there is an inverse relation between the reflection's width and the NPs average size.

$$D = \frac{0.9\lambda}{\beta \cos\theta} \quad (12)$$

Where:

$$\begin{aligned} D &= \text{Particle diameter size (nm)} \\ \lambda &= X - \text{ray wavelenght (0.1790 nm)} \\ \beta &= \text{full width at half maximum} \\ \theta &= \text{Angle of the reflection} \end{aligned}$$

According to equation 12 the average size of the 30 nm NWs with multi-shaped nanoparticles is 85.7 nm and the average size of the 30 nm NWs with nanopyrramids is 47.8. This confirms what was shown in the TEM images of figure 24 and 25 that even though the size of the NWs is similar (30 nm) the NPs of the 30 nm NWs with multi-shaped nanoparticles are bigger than the nanopyrramids. Meanwhile, for the 40 nm nws and multishaped NPs the average size of the NPs is 93.6, which is lower than expected as the NWs are approximately 40 nm and the average size of the measured NPs is 60 nm bigger than for the 30 nm NWs with multishaped NPs. However, this could be as TEM is local and the measurement on the NWs and NPs size is approximated.

The (111)/(200) proportion of the 30 nm NWs with nanopyrramids and 40 nm NWs with multi-shaped NPs is lower than for the 30 nm NWs with multi-shaped NPs. This would indicate that the concentration of (200) interplanar distances is slightly lower for the 30 nm NWs with multi-shaped NPs which means that there is a lower concentration of NWs in comparison with NPs in the the 30 nm NWs with multi-shaped NPs. XRD experiments have to be done in the future using the reduced loading sample of the different catalyst to see

how (111)/(200) proportion changes. This was not possible during our research due to volume of sample limitations.

However, the copper catalyst is not pure metallic. All three samples have peak at 40° that correspond with the Cu_2O . Therefore, the catalysts are partially oxidized. The most probable cause of the catalyst oxidation is that the catalyst were exposed to air during the sample preparation and during the XRD analysis. Nevertheless, the intensity of this peak is considerably lower than the (111) and (200) peak in all samples, which would indicate a low CuO_2 concentration

4.3.2 Sample after drop casting

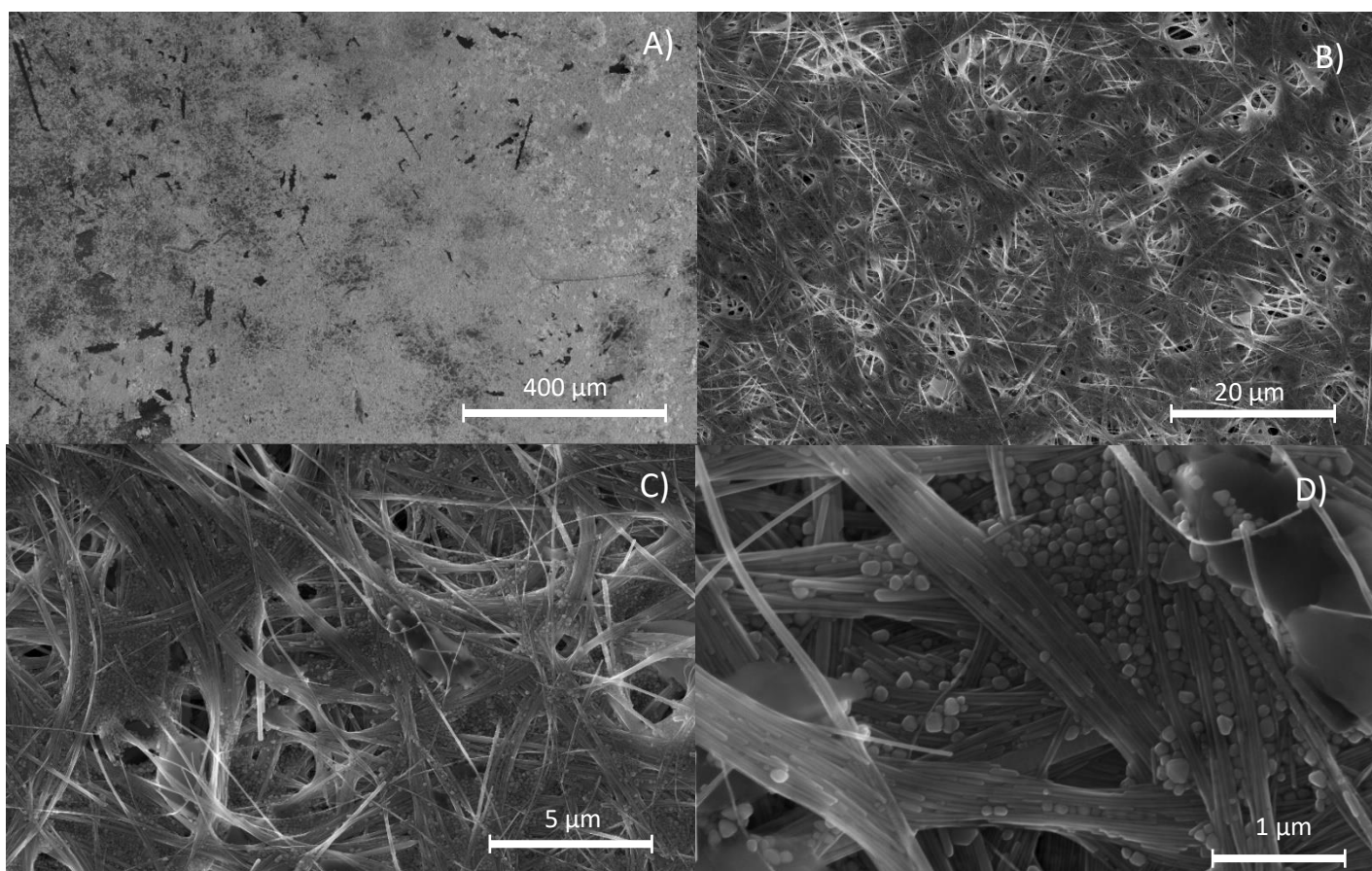


Figure 29: SEM images at different magnification of the 30 nm NWs with multi-shaped NPs catalyst after drop casting over the glassy carbon

Figure 29 shows how the 30 nm NWs with multi-shaped NPs catalyst is distributed over the glassy carbon after the drop-casting and drying. In **figure 29 A)** it is possible to see that the catalyst covers the glassy carbon in a primarily homogeneous way. There are spots on the glassy carbon electrode with a lower catalyst's concentration or even without any catalyst however, most of the surface is entirely coated by the colloidal nanostructures.

Increasing the magnification in the SEM (**Figure 29 B) C) D)**), it is possible to observe that the nanowires conform a 3D structure due to the stacking of the NWs, creating a porous structure. The nanoparticles can be found surrounding the nanowires or aggregated in some of these pores. The NWs conserve the bundle structure that we were able to see in the TEM images before the drop casting.

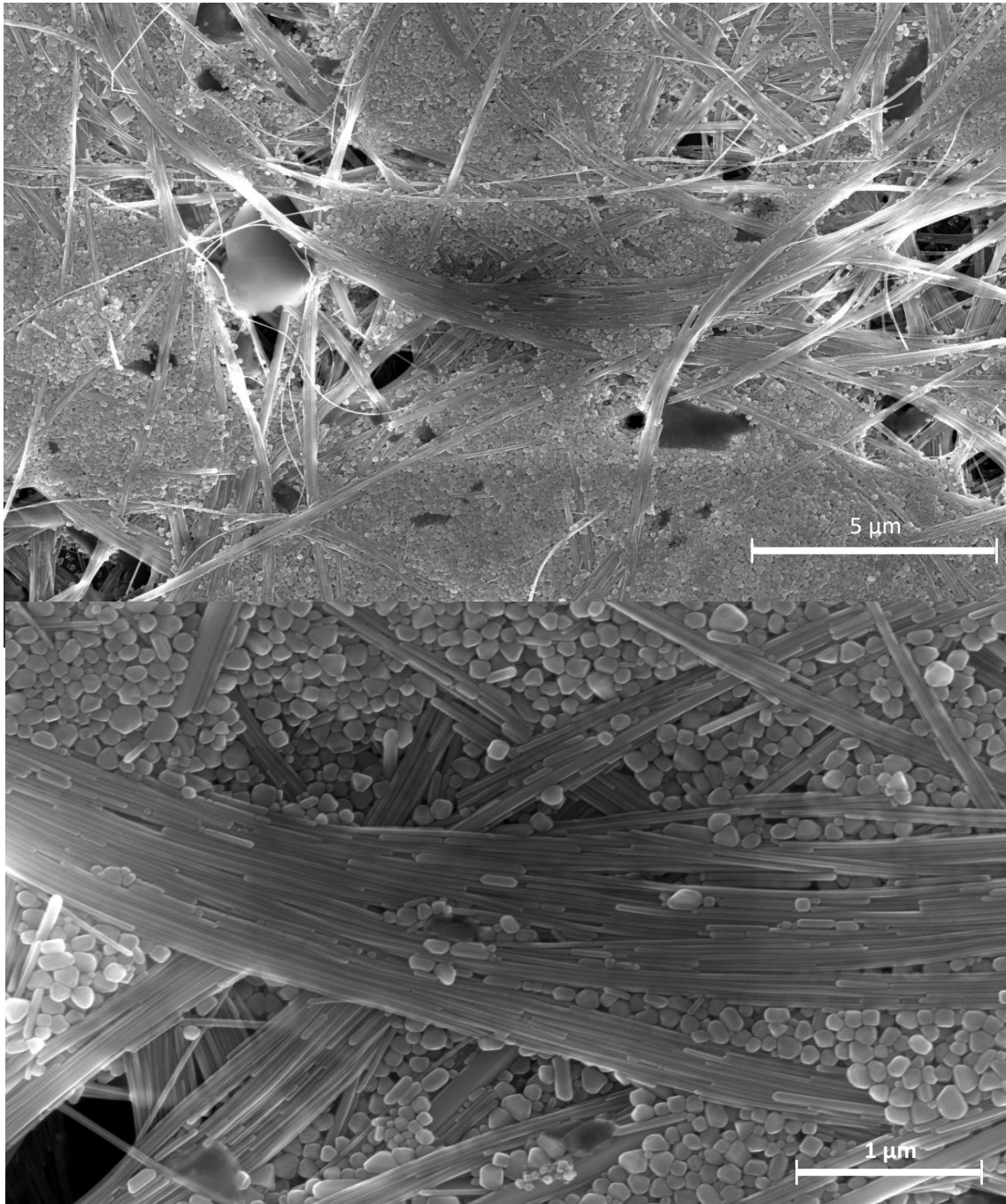


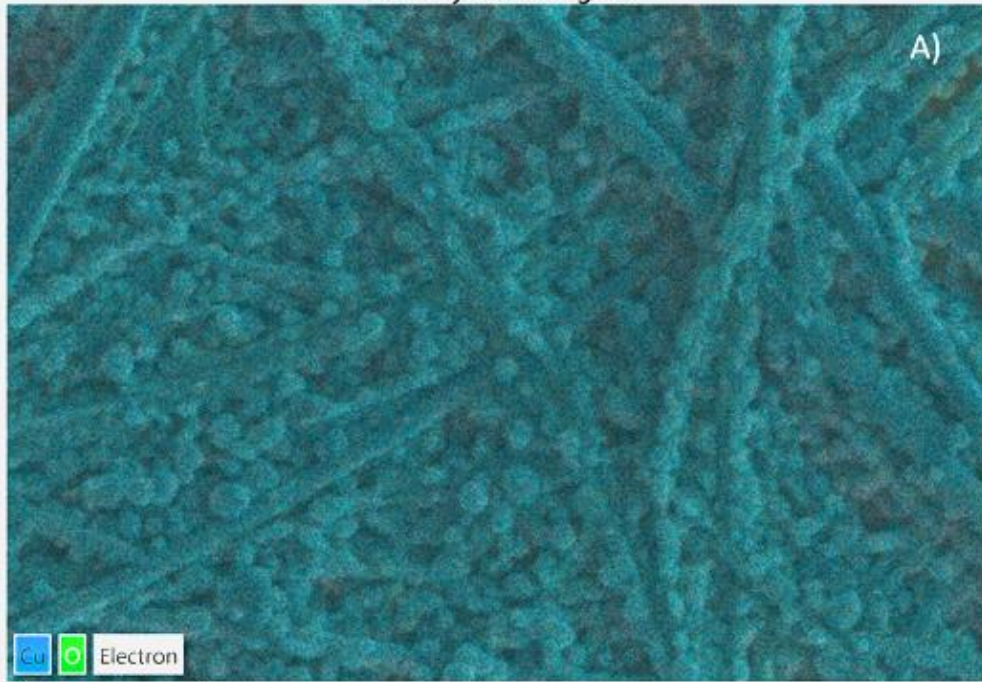
Figure 30: SEM images at different amplitudes of the 40 nm NW with a secondary nucleation of NP with multiple shapes catalyst after drop casting over the glassy carbon

In **figure 30**, we can see the 40 nm NWs with multi-shaped NPs catalyst over the glassy carbon after drop casting. The catalyst was spread similarly over the support as in the electrode shown in **figure 29**. The nanowires can be found individually or also aggregated in smaller bundles than in the 30 nm NWs catalysts. However, in contrast to the 30 nm NWs' sample shown in **figure 29**, in **figure 30** rather than the NPs being found surrounding the NWs or in pores created by the NWs accumulation, the NPs can be found in clusters that can completely cover the NWs in that area avoiding the adsorption of CO₂ over the NWs. Therefore, a phase-segregated system is created, where instead of having a mix of NWs and NPs over the electrode's surface, the NPs and NWs are founded separately.

Using EDX we were able to do an elemental mapping of catalyst over the electrode to analyze the distribution of copper, oxygen and if we can find any contamination. In **figure 31** the EDX elemental analysis of the pristine sample of 30 nm NW with a secondary nucleation of multi-shaped NPs catalyst is shown. The phase fraction for each product encountered in this area of the catalyst is 65.9% of copper, 17,2% of oxygen and 16.9% of carbon.

The elemental mapping use a color code to show the areas of the catalyst where the electron beam generate an x-ray radiation characteristic from certain element. In **figure 31**, Cu is represented with blue, O by green and C oby orange. The catalyst support is glassy carbon, which explains the apparition of this element in the EDX elemental analysis. However, we can not discard that the presence of carbon could also be due to contamination of the electrode with the polishing powder used during the cleaning as it is made of 5 μm diamonds. Carbon has a similar phase fraction as oxygen over the catalyst's surface and inspecting **figure 31 B) and C)** where the location of both elements is exposed, most of the oxygen is located in the same areas where the carbon is visible and dark areas are exposed in the fraction where the NWs would be located. However, the carbon is located in areas with also a high concentration of Cu NPs. Therefore, most of the oxygen is located over the glassy carbon and the nanoparticle which would suggest that the oxide contamination founded in the XRD analysis (**section 4.3.1**) could affect principally the NPs and not the NWs. XRD and EDX analysis was attempted only to the NPs, however it was not possible due to the very low signal emitted by the sample with XRD and the very high dilution of the NPs made impossible the sample preparation with high concentration for SEM .

EDS Layered Image 1



O K α 1

C K α 1_2

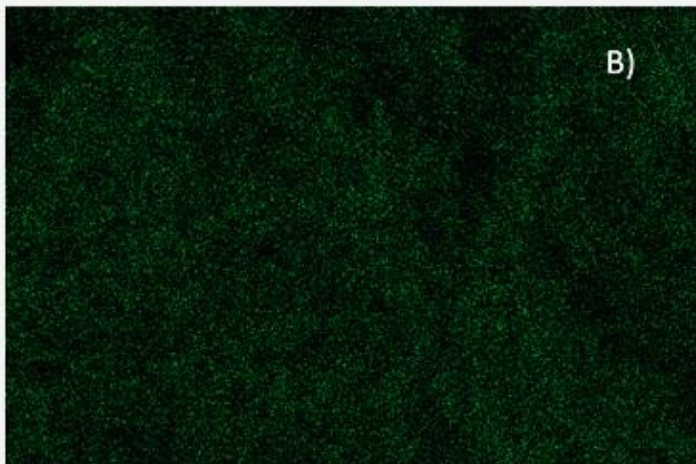


Figure 31: EDX mapping of the pristine sample of 30 nm NW with a secondary nucleation of multi-shaped NPs. A) Elemental mapping including the Cu and O elements. B) Elemental mapping of Oxygen. C) Elemental mapping of C

4.4 Electrochemical Performance and characterization post syhtesis

4.4.1 30 nm nanowires and multi-shaped nanoparticles

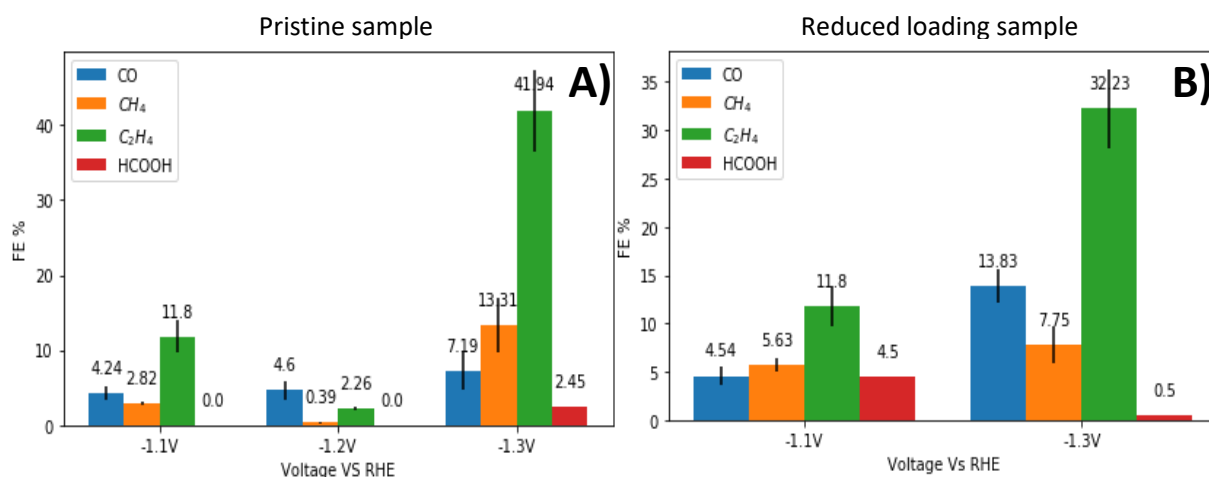


Figure 32: Average FE toward Carbon products from the last 10 injections from the catalyst formed by 30 nm nanowire and multiple shapes nanoparticles A) Pristine sample and B) Reduced Loading sample

In **figure 32**, it is represented the average faradaic efficiency for each specific carbon product during the last 10 injections (40 minutes) of the CO₂ electrocatalysis using 30 nm NWs and multiple shape NPs as a catalyst. **Figure 32 A)** is the pristine sample and **figure 32 B)** is the reduced loading sample. The rest of the FE of the catalytic reaction not represented in this table goes towards HER producing H₂. Experiments have been done at voltages less cathodic than -1.1V (at -1 V and -1.05 V); however, no product was detected.

Comparing both samples, it is possible to observe that the graphs follow a similar pattern. At -1.1V Vs RHE, both the CO and Ethylene have a comparable efficiency in the pristine and the reduced loading samples. At -1.2 V, a minimum is found for the FE of both catalysts, being the efficiency of the reduced loading sample less than 0.01% for all possible C products. Finally, at -1.3 V, both samples have a peak of ethylene production that exceeds 30%, being the pristine sample the one with the higher FE of all the tested catalyst with a 41.9%. Furthermore, at this overpotential, it is possible to observe liquid product (measured using NMR) in the form of Formic Acid in both catalysts.

The total Faradaic Efficiency for carbon products at -1.1 V is higher for the reduced loading sample with 26.7% than the 18.9% originating from the pristine sample. Yet, at -1.3 V, the pristine sample (64.9%) surpasses the reduced loading (54.3%) total FE toward carbon products. At -1.3 V, the pristine sample has a higher FE toward all the carbon products except for CO. Therefore, at -1.3 V, the reduced loading sample is producing CO* intermediate but is detached from the catalyst before it continues its reduction methane or

C₂ products. However, the pristine sample is able to maintain the CO* intermediate and continue its reduction toward ethylene.

The maximum FE towards ethylene in the experiments with polycrystalline Cu of Hori *et al.*¹³ and Kuhl *et al.*⁴⁶ was 28%. However, the overpotential needed to arrive at this FE was -1.1 V, whereas the 30 nm NW with multi-shaped NPs had an ethylene's FE of 11.8% in both the pristine and the reduced loading sample. Moreover, in the experiments with polycrystalline Cu, at more cathodic bias than -1 V and in the maximum FE toward ethylene, the presence of CO is less than 5%. However, in **figure 32 B**) at -1.3 V, there is a maximum toward CO production with a 13.8%.

If we compare the selectivity of the electrocatalytic reduction of CO₂ of the 30 nm NWs with multi-shaped NPs from **figure 32** with other Cu NWs catalysis experiments, we can notice several things. Comparing with the Cu NWs without (100) exposed facets from Ma *et al.*⁶⁹, the main product is CH₄ and their peak for ethylene production is 12% at -0.9 V vs RHE, much lower than the maximum for both the pristine and the reduced loading sample in **figure 32**, however Ma *et al.* reaches this maximum with a much less cathodic bias. Comparing it with the 20 nm 5-fold NWs with (100) exposed facets from Yifan *et al.*⁷⁸, the primary product is also CH₄, and the ethylene's peak is 10% at -1.25 V. This high selectivity towards methane was attributed to the edge sites of the five-fold twinned NWs. This edge sited are degraded with time under experimental conditions the FE shifts from methane to ethylene a 10%.⁷⁸ However, when Zhang *et al.*⁹³ used NWs with the same 5-fold twinned structure with (100) exposed facets but with a diameter of 50 nm, the FE towards ethylene was 35% at -1.1 V and with a 25% toward ethane. Nevertheless, the electrocatalysis experiment of Zhang *et al.*⁹³ differs from our set up as they used CO instead of CO₂, which favours C₂ production.⁵⁷ Therefore, even though more overpotential is needed to reach maximum FE for the 30 nm NWs with multi-shaped NPs, the maximum selectivity toward ethylene is higher than is most other examples. Activity experiments using CO should be done in the future to all NWs and NPs catalyst to be able to compare in the same catalysis conditions.

The presence of the nanoparticles together with the 30 nm nanowires seems to impact the reduction capacity of the catalyst directly. At -1.3 V, the total faradaic efficiency is higher for the pristine sample (64.91%) than for the reduced loading sample (53.9%). The reduced loading sample has a lower tendency towards CH₄ and C₂H₄ but higher for CO. CO is the key intermediate for C₂ products and methane, as shown in figure 7 from Birdja *et al.*⁵⁰. Therefore, if more CO is produced as a final product, it means that the binding strength for the CO* intermediate with the catalyst surface is lower in the reduced loading sample which avoids its reduction toward C₂ products.

In **figure 31** we can see that there is a high selectivity toward methane at -1.3 V in both the pristine and the reduced loading sample with a 13.3% and a 7.8% respectively. Yifan *et al.*⁷⁸ also had a high selectivity towards CH₄ with their 20 nm 5-fold NWs with (100) exposed

facets. However, in Yifan *et al.* experiments, this high selectivity is attributed to the active corner sites of the NWs, even more, according to Yang *et al.*⁷⁰, grain boundaries between (100) facets tends to increase the FE toward methane. As the NPs have a higher number of grain boundaries, (as they are not perfectly spherical) and there is a higher production of methane in the pristine sample than in the reduced loading sample there is a high chance of the NPs being responsible for the selectivity towards methane. However, experiments using only the NPs for catalysis should be done to confirm this hypothesis.

In the case of -1.2 V, the pristine sample has more reduction power than the reduced loading one. At -1.2 V, there is a minimum of activity from both samples, but even though the reduced loading sample is below the detection limit of the chromatograph, for the pristine sample, it has a total FE toward Carbon products of 7.25%. The hypothesis is that the NPs are catalytically active at -1.2 V whereas the nanowires have a minimum of activity at this voltage, which could imply that to activate the NW catalyst, it is necessary to arrive to more cathodic bias than -1.2 V. Nevertheless, the NPs can catalyze the CO_2 reduction at -1.1 V and -1.2 V. This hypothesis is reinforced with the zero selectivity toward CO_2 in bias less cathodic than -1.1 V which in comparison with the work of Raciti *et al.* and of Zhang *et al.*⁹³ with Cu NWs catalyst with (100) facets where their maximum FE toward ethylene was at -1.0 V and -1.1 V respectively. The first suspect for this minimum at -1.2 V and low activity at less cathodic bias was mass transfer limitations where the CO_2 was not able to reach the surface of the catalyst due to the high concentration of OH^- ions typical of the nanowires catalyst^{45,63,65}. However, according to the work of Raciti *et al.*⁹⁴, mass transfer limitation in nanowires is predominant in voltages more positive than -0.5 V and more negative than -1.2 V and in **figure 31** the maximum is at -1.3 V therefore discarding mass transport limitations as the cause of the high voltage needed to activate the catalyst. The next possibility is the presence of ligands over the surface of the catalyst that are not eliminated from the surface of the NWs until reaching high negative potentials. Raman spectroscopy was done for the 30 nm NWs with nanopyrramids (**section 4.4.2**) where a partial elimination of the oleylamine ligands were detected, however, no other organic species were found in the electrolyte after activity using NMR, which could imply that the organic species are completely reduce to CO_2 and N_2 and other gas species, or that most of the ligands are still attached to the surface during activity. The lack of ligand removal could explain the low current density shown in **figure 32**.

In **figure 32** we can observe the ethylene detected by the chromatograph in each injection of a catalysis experiment for the pristine and the reduced loading sample with a voltage of -1.3 V. In addition, the current intensity and average current of the experiments are also exposed against time. Looking at the current in both samples, it can be noticed that there is a shift in current towards more positive values in the first minute of activity. There are two possible reasons for this change. The first reason is the removal of the ligands by reduction of the organic species due to the negative bias applied to the catalyst, which increases the conductivity of the copper nanowires. The second reason could be a surface

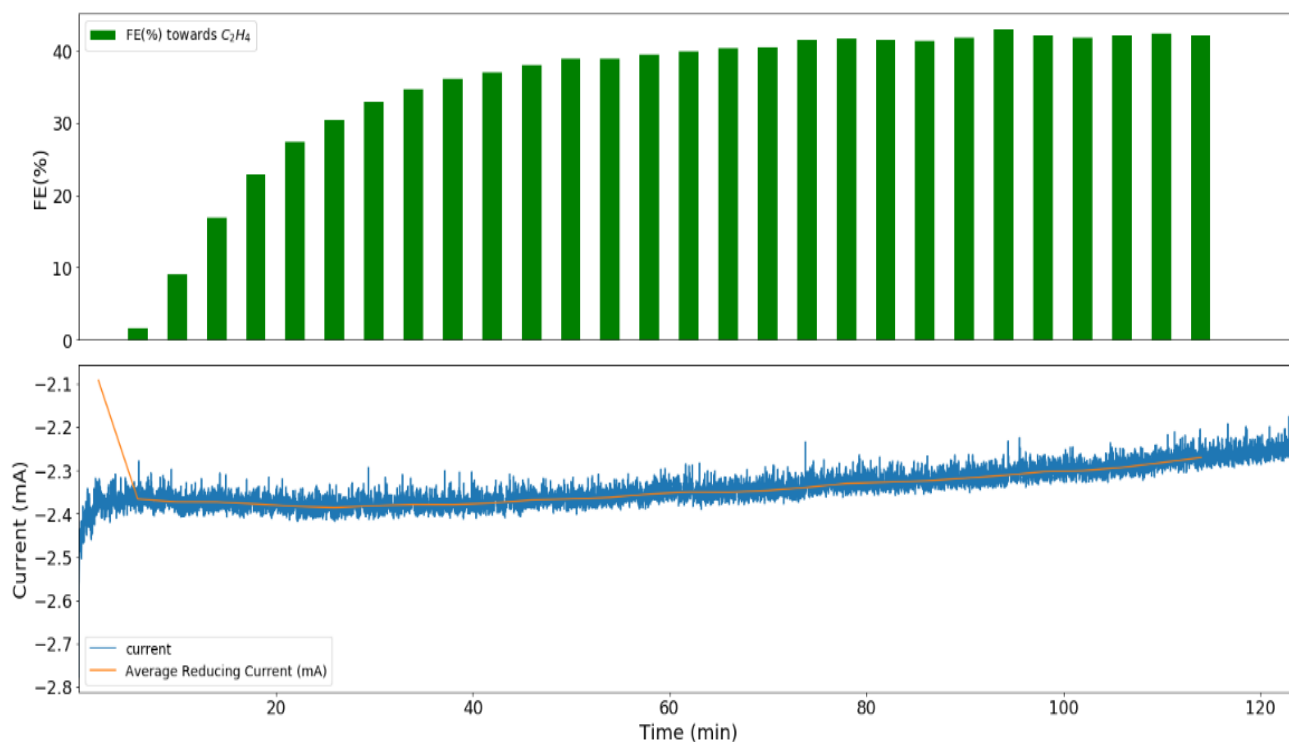
reconstruction due to the negative bias, as it happens in the work of Yifan *et al.*⁷⁸ where the highly active grain boundaries that produced CH₄ were eliminated and the selectivity transitioned toward a higher ethylene production. This hypothesis is supported by the constant increase of current ethylene production in the pristine sample shown in **figure 32 A**). In the reduced loading sample (**Figure 32 b**) the current is more stable and the maximum FE toward ethylene is reached sooner and is lower than for the pristine sample, as the reduced loading sample has less nanoparticles than the pristine one therefore it suggests that the reconstruction can be found mainly in the NPs. To confirm this theory XRD experiments have been done in the samples after catalysis, however the signal received was too low to make any conclusion due to the loss of material that we will analyze in **figure 33**. Another possibility is the migration of the NPs during catalysis conditions over the surface of the catalyst. A negative current could cause the migration and aggregation between themselves and the NWs. An example of this phenomenon can be seen in the work of Manthiram *et al.*²⁵ where their 7 nm Cu NPs aggregate during operando conditions forming 25 nm nanostructures. This hypothesis is supported by the SEM imaging post activity at -1.3 V in **figure 33**. In **figure 33** we can see a high catalyst material loss and how the NPs are aggregated over the catalyst surface. This aggregation could also explain the increase in time of the FE of ethylene as it approaches the NPs and the NWs, which facilitates the transfer of intermediates between structures.

It is possible to observe a sudden current change in **figure 32 B**) from -1.5 mA to -2.75 mA. This was due to the manual elimination of a CO₂ bubble over the membrane's surface by gently leaning the cell.

The average current for the pristine sample during the catalysis is approximately -2.25 mA and for the reduced loading sample is -2.1 mA. A low current causes mass transport limitations as the number of electrons that are available in the active sites to be transferred to the species for catalysis is reduced. If we compared it with the bulk copper sample from the work of Kuhl *et al.*⁴⁶ in **Figure 10 A**), the current is significantly lower for the copper nanowires using the same electrolyte. Bulk copper at -1.2 V vs RHE reached a current of -18 mA, 9 times higher than the 30 nm copper nanowires at -1.3 V. Multiple reasons can be attributed to this difference. The presence of ligands, organic material, over the catalyst surface can significantly reduce the conductivity of the nanowires. Moreover, the need for a glassy carbon support for the catalyst could also affect the final conductivity, as in the experiment of Hori *et al.* there was no need for support. Even more, as shown in **figure 33**, there is a loss in material after catalysis which exposes the glassy carbon and can also reduce the conductivity of the catalyst. Finally, due to contact with air during catalysis there can be a partial reduction of the copper catalyst to Cu₂ which has been observed in the XRD experiments (**section 4.3.1**) and Raman spectroscopy (**section 4.4.2**) would also lower the conductivity. The more negative current that we can find in the pristine sample can be explained by the higher number of nanoparticles making contact between the nanowires and helping to conduct the electrons.

Ethylene FE and current for 30 nm NW and multi-shaped NPs at -1.3 V

Pristine Sample



Reduced Loading Sample

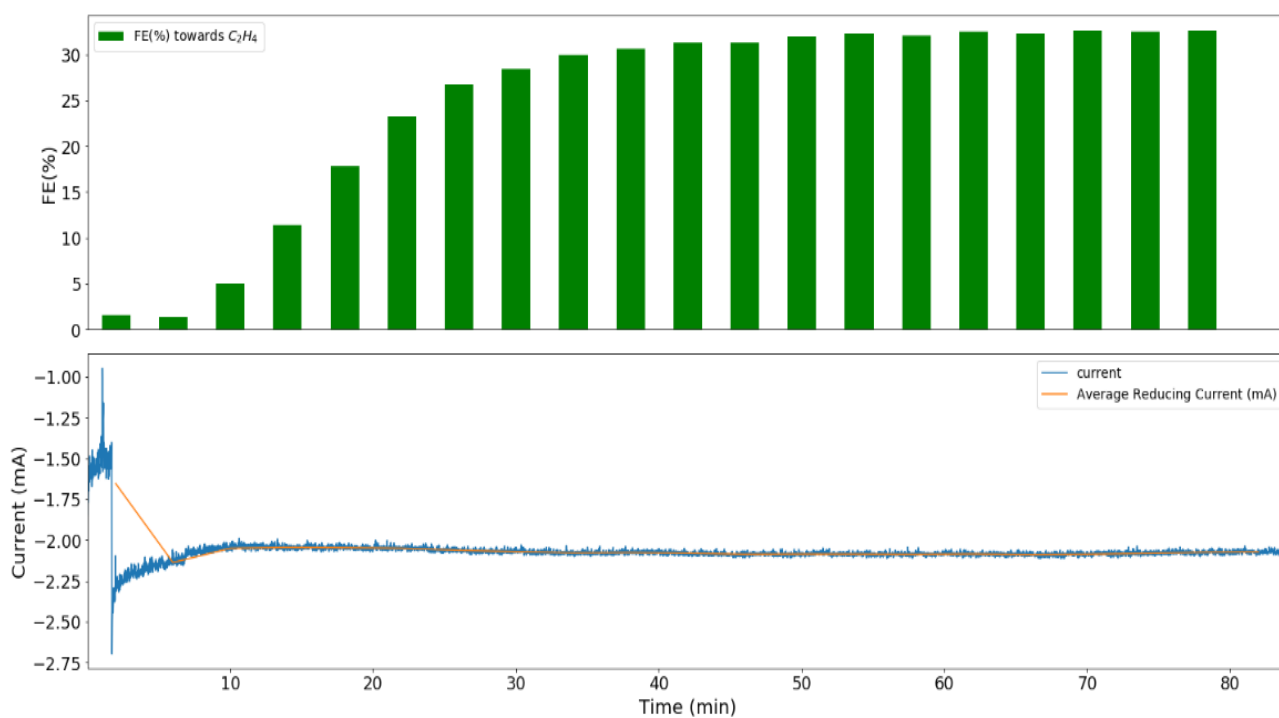


Figure 32: FE evolution of the Ethylene production against time during an activity experiment at -1.3 V using 30 nm NWs and multiple shape NPs as a catalyst and the current, and average current against time during the catalytic activity.

The pristine sample had a stable FE toward ethylene during the almost two hours of the experiments, reaching a 30% FE at 30 minutes and a 38% at 110 minutes. The current is stable for most of the experiment however, after 80 minutes, it starts to drift towards a more positive value slowly. In the case of the reduced loading sample, after the initial current shift, the current is stable for the duration of all the experiment, with the exception of the bubble removal. This stability indicates a lower surface reconstruction of the catalyst, which also imply that the principal nanostructure affected by the reconstruction are the multi-shaped NPs and not the NWs.

In the future, for all samples experiments to determine the ECSA (Electrochemical surface area) should be done. ECSA is the area of the electrode material that is accessible to the electrolyte that is used for charge transfer and/or storage.⁹⁵ Analyzing and comparing the ECSA from the different catalyst and its reduced loading counterpart will gave valuable information about the number of active sites available for catalysis and a better explanation of the low conductivity of the catalyst.

Figure 33 A) shows the 30 nm NWs with multi-shaped NPs catalyst after a 2 hours activity at -1.3 V vs RHE. At first glance it is possible to notice that compared with the pre activity sample (**figure 29**) there is a loss of material, probably dissolved in the electrolyte, which exposes the glassy carbon support. However, glassy carbon during catalysis produces H_2 , but hydrogen production constantly diminish during the experiments which indicates that most probably the material loss happens in the early stages of the experiment which would also partially explain the low current in **figure 32**. This loss of material does not occur at less negative potentials like -1.1 V, -1.2 V (Annex). Which would imply that the activation of the catalyst at higher overpotentials and the restructuring of the catalyst causes the material loss.

Most of the 3D structure has disappeared, the number of pores radically decreased, and all the NPs can be encountered around the NWs in a much lower concentration. Measuring the nanowires, we can observe that the diameter stayed roughly the same from 29.7 ± 4.3 nm to 31.8 ± 7.3 nm, which falls within the size standard deviation. Moreover, the nanoparticles went from 121.7 ± 13.6 nm to 110.01 ± 19.25 nm, which also falls into the standard deviation therefore, is it also roughly the same diameter. The low to none variation of the NP and NW sizes, suggest that if there is a surface reconstruction it does not affect the NWs and NPs width and that the catalyst's exposure to air does not completely oxidize the sample, or at least just form a thin layer of oxide over the NWs and/or the NPs. Moreover, on the EDX mapping (**figure 33 B) and C**) the oxygen can be seen mostly covering the exposed surface of the support and over the NPs, leaving empty spaces where the NWs are situated. The location of the oxygen would suggest that if there is any oxidation it principally affects the NPs. However, to be able to confirm the lack of oxidation of the nanowires, it would be necessary to perform XRD analysis after catalysis. But, as explained before, due to the loss

of material during activity, all XRD experiment done after catalysis gave as a result a signal too low to be able to give any definitive conclusion.

A possible alternative for XRD would be electron diffraction during electron microscopy. The resulting diffraction pattern after the interaction between the electrons and the crystalline (or not) structures of the catalyst after activity would inform us of the crystalline state of the sample.

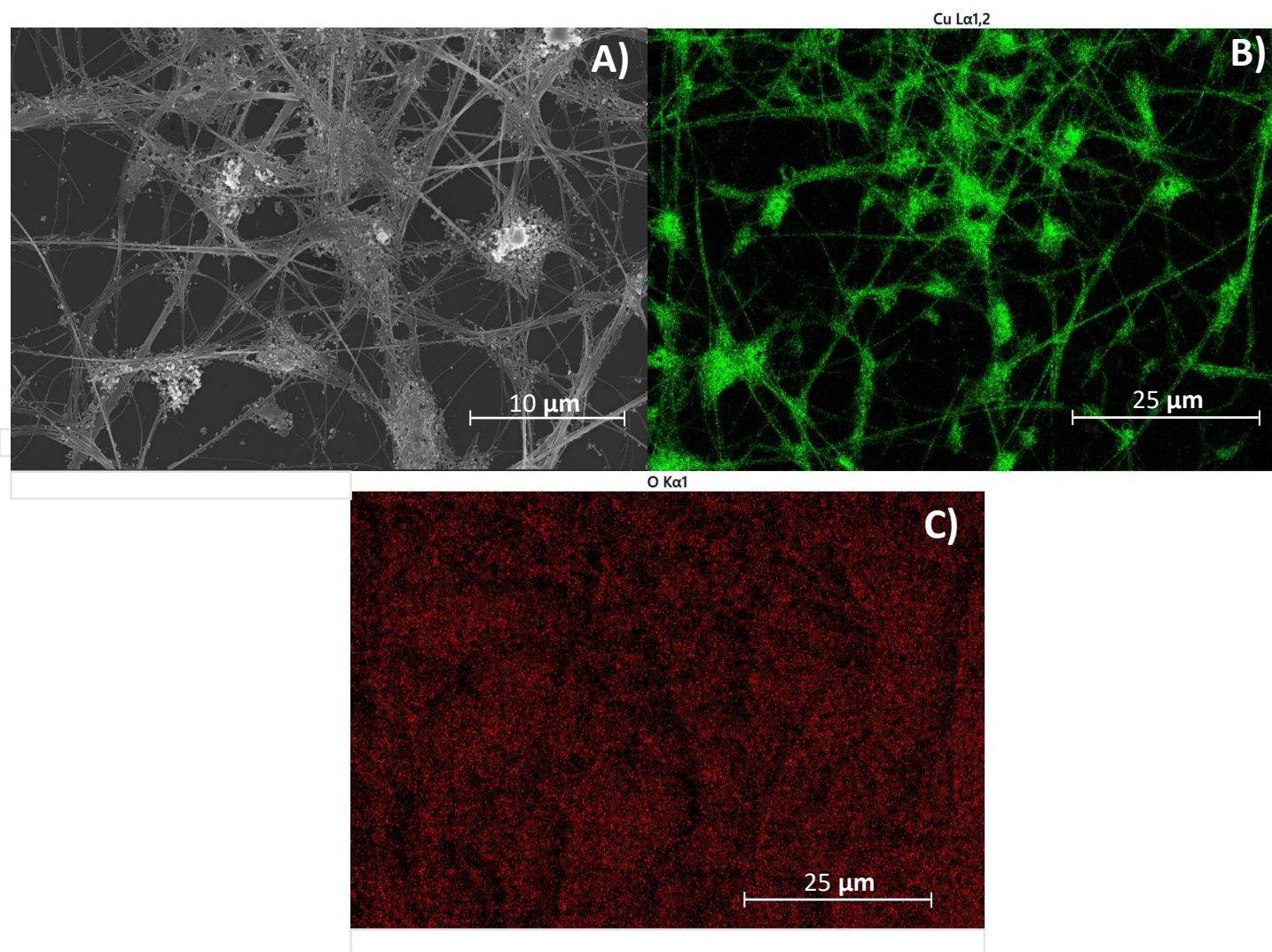


Figure 33: A) SEM image of the 30 nm NW with multi-shaped nanoparticles catalyst after 2 hours of activity at -1.3 V vs RHE. B) EDX mapping of the Cu element on the same area of the catalyst (green). C) EDX mapping of the O element on the same area of the catalyst (red)

The proposed mechanism for the formation of ethylene over the 30 nm NWs with multi-shaped nanoparticles to explain the FE reflected at -1.3 V in **figure 31** is exposed in **figure 34**.

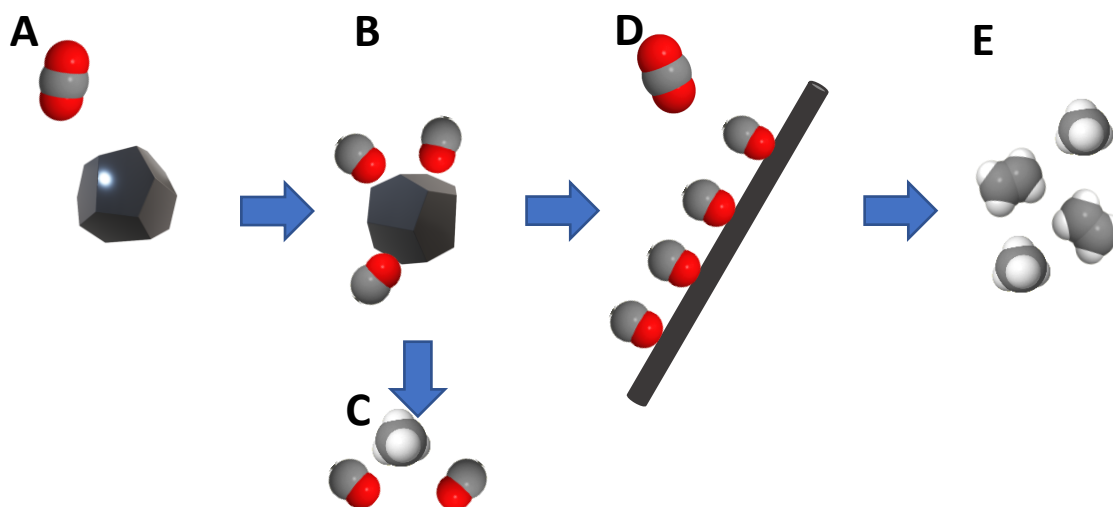


Figure 34: Reduction pathway mechanism for the reduction of CO over the the 30 nm NWs with multi-shaped nanoparticles catalyst

In **figure 34** we have represented how in A the CO_2 is adsorbed over the NPs surface to be reduced into the CO^* intermediate (B). Once CO^* is created over the NPs surface it can desorb to release CO into the electrolyte or be reduced over the NPs to form CH_4 (C). However, the CO^* can also be transferred to the NW surface where also CO_2 is being adsorbed (D) and be reduced to ethylene and methane (E).

4.4.2 30 nm nanowires and nanopyramids

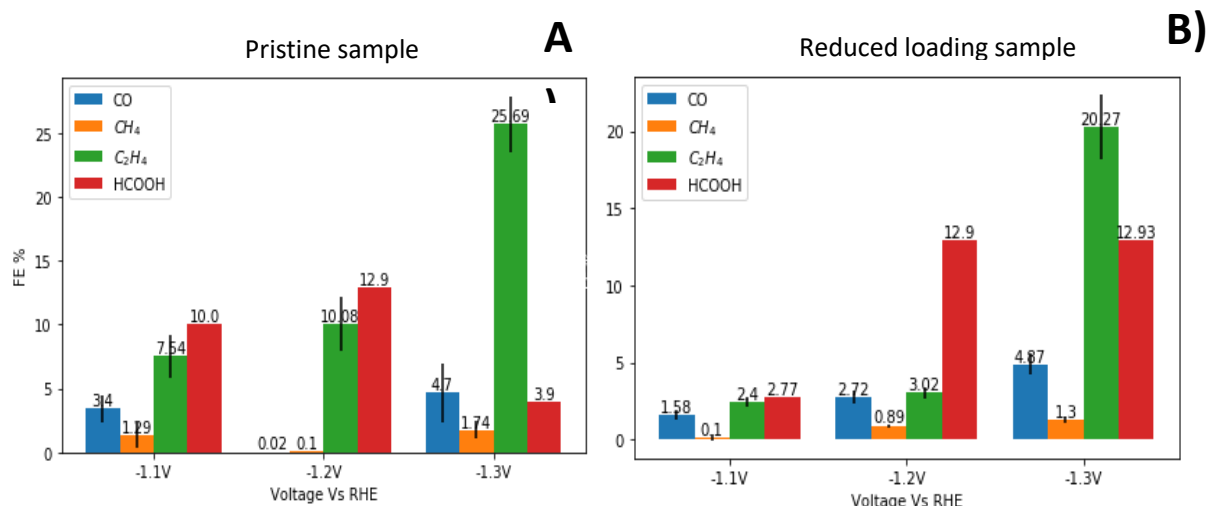


Figure 35: Average FE toward Carbon products from the last 10 injections from the catalyst formed by 30 nm nanowire and nanopyramids A) Pristine sample and B) Reduced Loading sample

In the case of 30 nm NW with nanopyramids, the total FE for carbon products (**figure 35**) is notably higher for the pristine sample at -1.1 V (22,3%) and -1.2 V (23,1%) than for the reduced loading sample, being 6.9% at -1.1 V and 19.5% at -1.2 V. This indicates an increase

in the catalyst's reducing power when there is a higher concentration of NPs, which is specially reflected in the ethylene production. At -1.1 V and -1.2 V the pristine sample FE toward ethylene (7.5% and 10.1% respectively) is three times higher than in the reduced loading sample (2.4% and 3.02%). At -1.3 V, the higher reducing power of the pristine sample is still present, with a higher selectivity toward ethylene even though the total FE for Carbon products is slightly higher for the reduced loading sample (39.4%) than for the pristine sample (36%).

Liquid products appear for both samples at all the different voltages in the form of formic acid. If we look at the trend, in the case of the pristine sample, the maximum is at -1.2 V with a 12.9%, and a minimum at -1.3 V with 3.9%. However, for the reduced loading sample the both -1.2 V and -1.3 V have the same FE towards formic acid (12.9%).

The catalyst formed by 30 nm NW and multiple shape NPs did not produce formic acid except at -1.3 V, therefore as the size and exposed facets of the NWs are the same, the nanopyrramids must produce the formic acid. Moreover, the lower production of ethylene in **figure 35** than in **figure 31** must also be correlated with the nanopyrramids.

According to recent literature, high production of formic acid during the electrocatalytic reduction of CO_2 has been attributed to highly oxidized Cu catalyst^{96,68} and to a high surface area due to a porous Cu structure caused by mass transport limitations and a high local pH.⁶³ The best example is the work of Guo *et al.*⁹⁷ with a FE toward formic acid of 80% with a highly porous dendritic Cu structure. However, the 30 nm nanowires are not highly oxidized pre-activity, as showed in **section 4.3.1**, or post-activity as showed in **figure 37**. Moreover, experiments have to be done to determine the ECSA, but as the 30 nm NWs and NPs of the 30 nm NWs with multi-shaped NPs (**figure 31**) and the 30 nm NWs with nanopyrramids (**Figure 35**), are similar in size and in XRD structure there is little reason to believe that the ECSA would be different enough to justify the high difference in the final product, however ECSA experiments should be done in the future to confirm this hypothesis.

Another factor that favours the production of formic acid is the presence of (111) exposed facets.²⁴ Liu *et al.*⁹⁸ tested the selectivity during CO_2 reduction of pyramidal Cu nanostructures with exposed (111) facets to compare it with the selectivity of the same Cu structure doped with Ag. Similarly to the 30 nm NWs with nanopyrramids, in Liu *et al.* nanopyrramids, there is a high FE towards formic acid between -1.0 V to -1.3 V with a maximum FE of 19% at -1.1 V. However, the selectivity towards ethylene in the same range is close to zero and the FE toward methane is approximately 50%, whereas in **figure 35**, the 30 nm NWs with nanopyrramids, there is less than 2% FE toward methane and a maximum of 25.7% towards ethylene.

As shown in **figure 7** from Birdja *et al.*,⁵⁰ the lower energy path toward methane and C_2 products originate from the CO^* intermediate, however formic acid, is produced after COH^* and COOH^* . During electrocatalysis, Cu (111) facets produce more COH^* and COOH^*

intermediates than (100) and (110) facets.⁹⁹ COH^* and COOH^* are transformed mainly in C_1 products like methane and formic acid.⁹⁹ Therefore, as the catalyst is not oxidated, and the surface area is probably not extremely different than in the 30 nm NWs with multi-shaped NPs the most probably hypothesis for the higher tendency toward formic acid is that the nanopyramid's exposed facets are (111). However, XRD or diffraction pattern with HR-TEM of exclusively the nanopyramids is necessary to confirm it.

However, as shown in the work of Hori et al.²⁴ and the Cu nanopyramids of Liu et al.,⁹⁸ (111) facets also produces a very low selectivity towards ethylene and a high selectivity toward methane, whereas in **figure 35** the FE toward CH_4 is lower than 2%. Opposite to C_2 products, methane can be formed by CO^* intermediate and COOH^* , but the lowest energy path is through the CO^* intermediate.⁹⁹ In **figure 35** the C_2 production is higher in all the voltage range for the pristine sample than at the reduced loading sample with similar values of FE towards CO. Therefore, we know that the production of CO^* intermediate is higher at the pristine sample in all the bias range, however most of this CO^* intermediate is reduced to C_2 products instead than to methane or released as CO. This would suggest that the nanopyramid both produce the COOH^* intermediate (which would become formic acid) and the CO^* intermediate, that without the presence of NWs would become methane, however the CO^* is transferred to the Cu NWs and reduced to ethylene. Electrocatalytic test using only the Cu nanopyramids as catalyst should be done in the future to see if there is an increase in the methane production to confirm this hypothesis. The proposed mechanism of the electrocatalytic reduction of CO_2 over the 30 nm NWs with nanopyramids can be seen in **figure 36**.

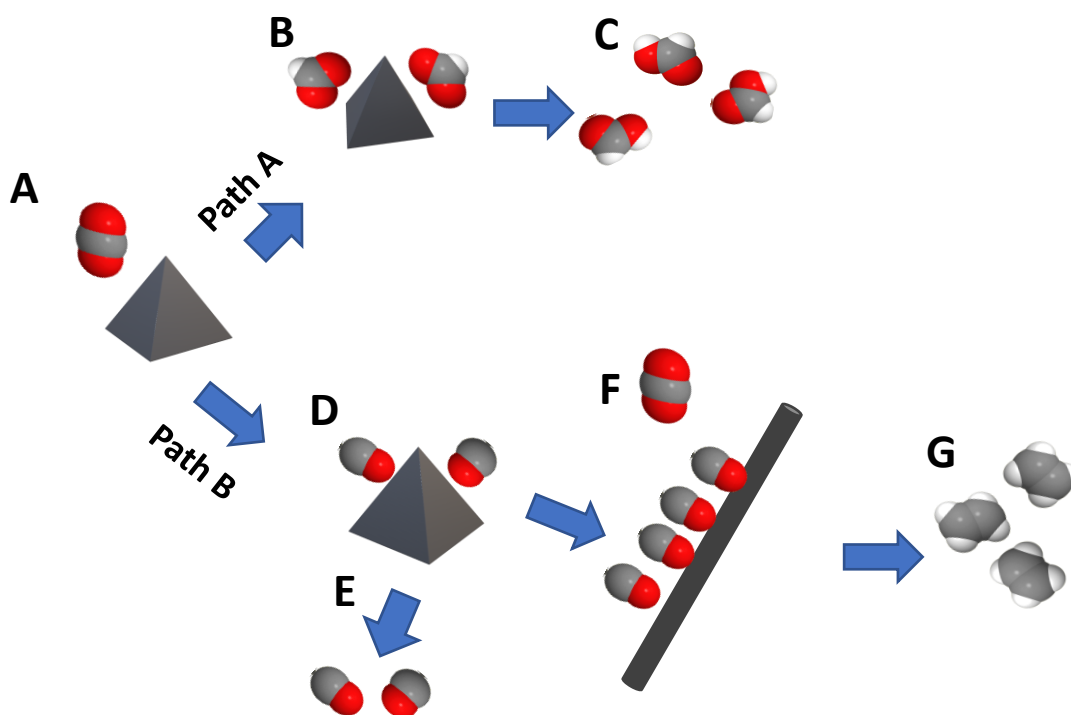


Figure 36: Reduction pathway mechanism for the reduction of CO_2 over the 30 nm NWs with nanopyramids catalyst

In **figure 36** we propose that the CO_2 gets adsorbed over the nanopyrramids surface (A) and there are two pathways. In path A, CO_2 is transformed into COOH^* (B) and then converted mainly into formic acid (C). In path B, CO_2 is transformed into the CO^* intermediate (D) and then it can be released in the form of CO (E) or the CO^* is adsorbed over the NWs surface at the same time as CO_2 and then transformed into ethylene.

In **figure 37** it is possible to see that in the pristine sample the C_2H_4 production has a slow but constant increase in the FE during the full duration of the experiment. Being the maximum FE toward Ethylene 26.7% at the 28th injection (112 minutes). The experiment had to be stopped due to time constraints, however, even though the FE keeps increasing the rate of growth was beginning to slow down. Focusing on the current of the pristine sample, we can observe that even if the current was constantly changing with many different peaks, the average current is relatively stable. After the first few minutes of ligand reduction and surface reconstruction, the current goes from -3.1 mA to -3.3 mA, and then gradually moves toward the -3.1 mA again in a steady pace for 40 minutes. The -3.1 mA will be maintained with slight variations, until the forced end of the experiment.

If we compare the ethylene FE evolution of the pristine 30 nm NWs with nanopyrramids sample (**figure 37 A**) with the pristine sample of 30 nm NWs with multi-shaped NPs in **figure 32 A**, we can see that with the multi-shaped NPs the current is more stable and the FE towards ethylene growth slows down just after 60 minutes. Moreover, if we compare the pristine sample of 30 nm NWs with nanopyrramids with its reduced loading sample, we can observe that the current is significantly more stable during the full duration of the experiment. In the work of Yifan *et al.*⁷⁸, using 20 nm 5-fold NWs with (100) exposed facets, they attributed the 10% shift on the FE between methane to ethylene after 20 minutes of activity to the surface reconstruction of the edge sites of the NWs. With the 30 nm NWs with multi-shaped NPs (**figure 32**) and with pyramids (**figure 37**) there is also a shift in ethylene production, this shift is in both cases more pronounced in the pristine sample than in the reduced loading sample and the current is more stable in both cases in the reduced loading sample than in the pristine sample. All these factors support the hypothesis that there is a surface reconstruction during catalysis conditions that principally affects the nanoparticles, multi-shaped and nanopyrramids. The more pronounced shift in ethylene production and the lower current stability in the pristine samples than the reduced loading samples indicate that this surface reconstruction mainly occurs in the NPs as the pristine sample has a higher concentration of NPs. Moreover, in the work of Yifan *et al.*⁷⁸ the surface reconstruction affects the surface's edge sites. Due to its structure, the nanopyrramids have high concentrations of these edge sites, which would explain why the surface reconstruction of the 30 nm NWs with nanopyrramids takes longer than in the catalyst with multi-shaped NPs as it keeps shifting towards ethylene production after 100 minutes of activity. However, XRD experiments have to be done post catalysis to prove the surface reconstruction. As in the case of the 30 nm NWs with multi-shaped NPs, after catalysis there is a loss of the 30 nm NWs with nanopyrramids catalyst over the electrode's surface which

Ethylene FE and current for 30 nm NW with Nanopyramids at -1.3 V

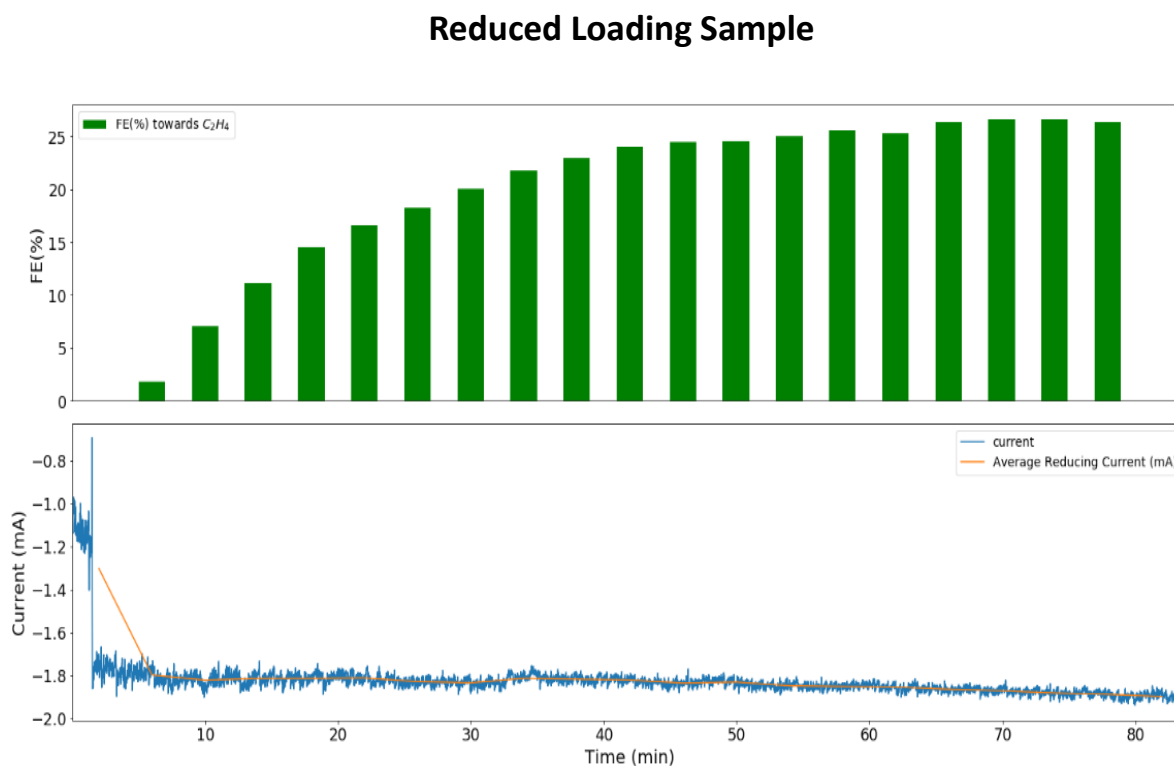
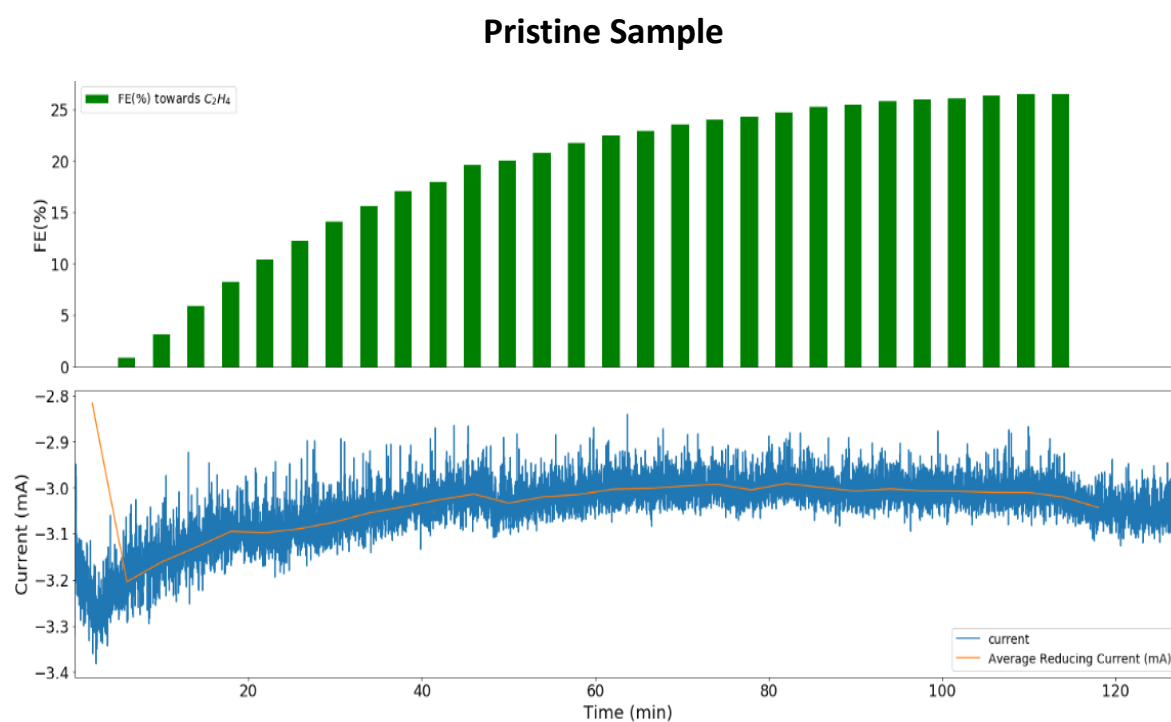


Figure 37: FE evolution of the Ethylene production against time during an activity experiment at -1.3 V using 30 nm NWs and nanopyramid as a catalyst and the current, and average current against time during the catalytic activity.

lowers the XRD signal and avoids the peak identification. However, SEM images have been taken after catalysis at -1.3 V vs RHE (**figure 38**). In **figure 38** and **annex C** is possible to see that the NPs and NWs have not been destroyed and most of the NPs conserve a triangular shape, however is not possible to have definitive conclusion about its exposed facets and edge sites.

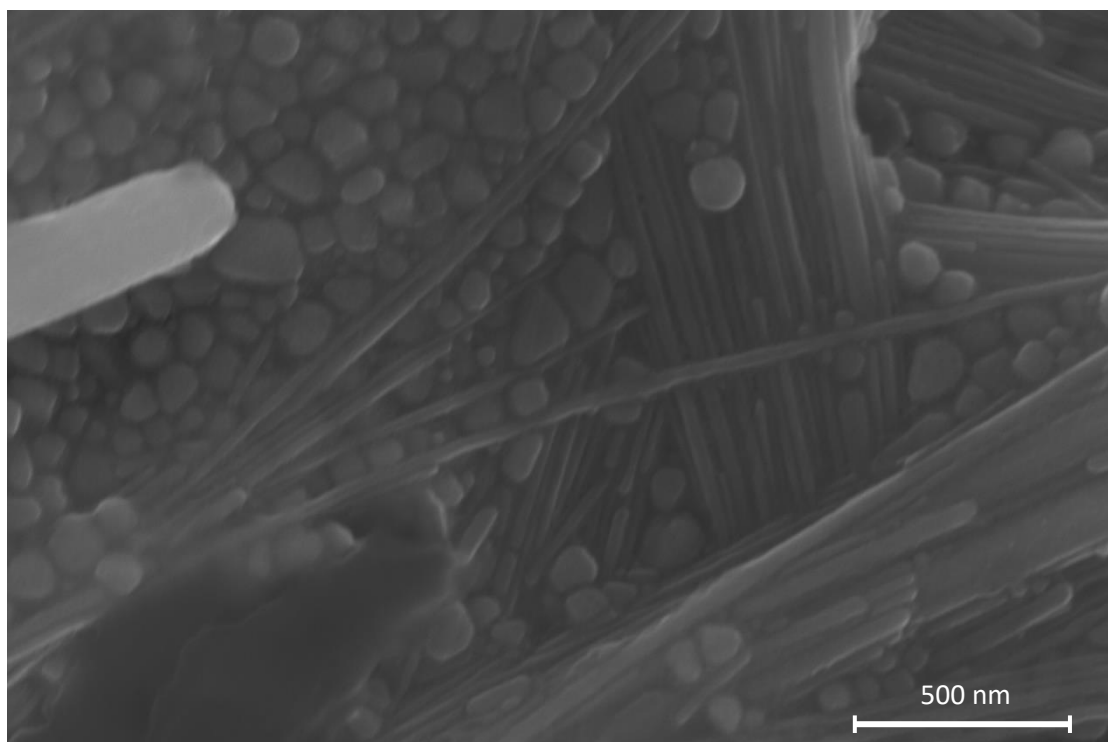


Figure 38: SEM image of the 30 nm NWs with nanopyrramids catalyst after 120 min of activity at -1.3 V vs RHE

The current jump in **figure 37 B)** from -1.2 mA to -1.8 mA is attributed to the elimination of gas bubbles formed around the cell's membrane. These bubbles are created due to the accumulation of the added CO_2 or gas product adsorbed over the membrane's surface. They affect the current as they change the electrolyte volume inside the catalytic cell, changing the volume of contact between the electrode and the electrolyte. Moreover, we can observe, as in the 30 nm NWs with multi-shaped NPs **figure 31**, there is also an increment in the negative current at the beginning which rapidly shifts towards more positive values. This shifts in current are attributed to an increment in the conductivity due to the reduction of the ligands, the lost of catalyst material over the electrodes surface (**figure 39 and annex**) which lowers the conductivity and to the surface reconstruction.

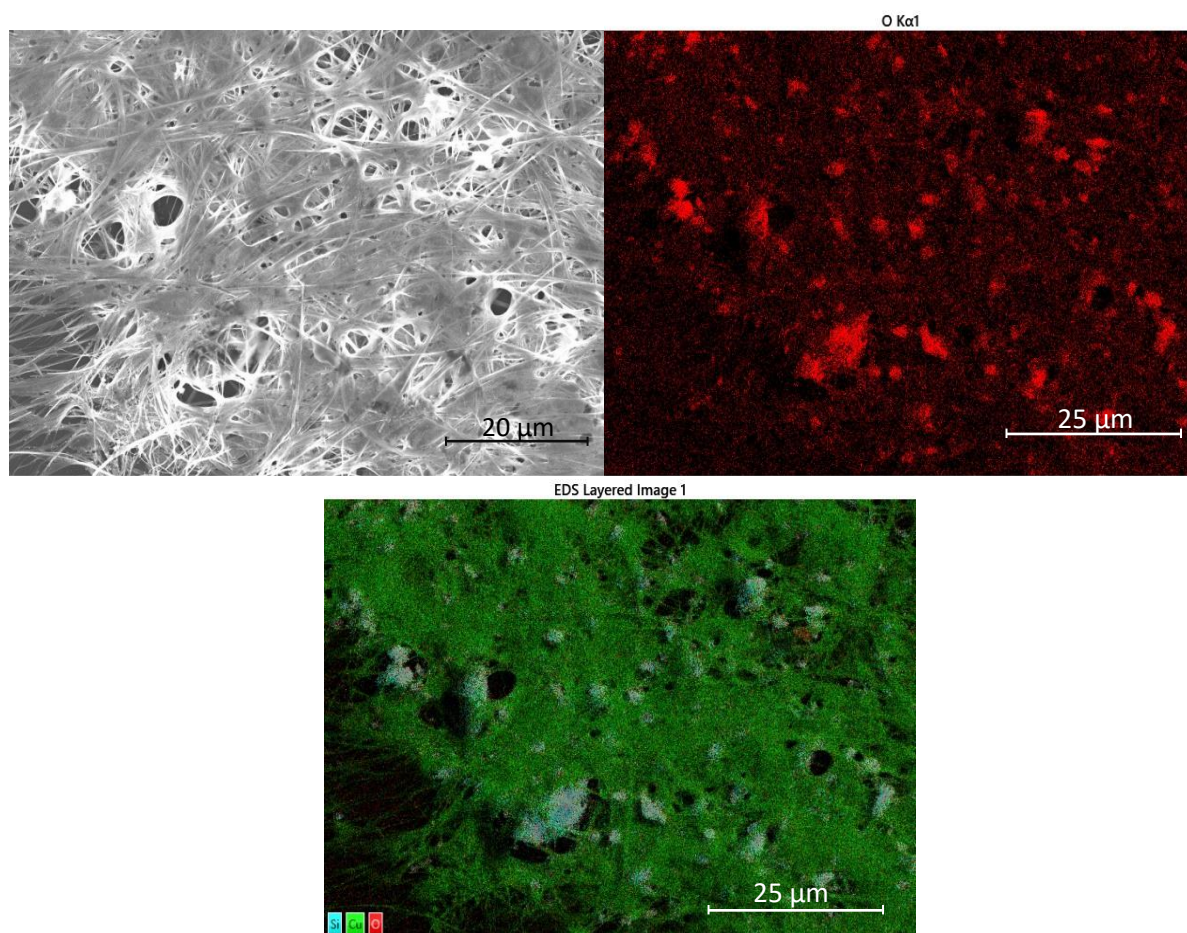


Figure 39: A) SEM image of the 30 nm NW nanopyramid catalyst after 2 hours of activity at -1.3 V vs RHE. B) Superposition of the EDX mappings of the Cu element, O element and Si element on the same area of the catalyst. C) EDX mappings of the O element on the same area of the catalyst .

In **figure 38 A)** it is shown the catalyst 30 nm NW with a secondary nucleation of nanopyramids after a 2 hour activity experiment at -1.3 V vs RHE. In this sample, there is also a considerable loss of material. The size of the NP and the NW are respectively $34,3 \pm 7.8$ nm and $87.29 \pm 16,43$, whereas, in the pre-activity sample it was respectively 31.1 ± 5.3 nm and 97.93 ± 13.8 . Both types of nanoparticles are still on the standard deviation which implies that there is not a growth of the catalyst during activity. On the EDX elemental analysis, we can see that there is a Silicon (Si) contamination over the catalyst, and most of the oxygen that is encountered in the sample is on the Si. The source of this contamination is believed to be a cross-contamination on the polishing station of a polishing powder composed of SiO_2 microspheres, which would explain the high content of oxygen over the Si. There has been research that have used SiO_2 and Cu to produce methanol during the electrocatalytic reduction of CO_2 , however, for the SiO_2 to interact with the CO_2 is necessary high temperature conditions with no activity reported under 170°C .¹⁰⁰ Therefore no influence of the SiO_2 is expected under our catalysis conditions.

In order to analyze the surface oxidation and the intermediates created during the electrocatalysis, Raman spectroscopy has been performed over the 30 nm NWs with nanopyramids surface. Raman is ideal as it allows the in situ characterization of the sample during catalytic conditions showing the bond vibration of the intermediate adsorbed over the catalyst surface and the oxidation of the sample.

Two Raman experiments were performed on the 30 nm NW nanopyramids catalyst. **Figure 40 A)** shows the different vibrations produced by the catalyst at -0.4 V vs RHE for 30 seconds. Between 0 and 750 cm^{-1} , it is possible to clearly distinguish three frequency peaks at 153, 209, and 409 cm^{-1} . These peaks correspond approximately to the vibrations of Cu_2O .¹⁰¹ The Cu_2O presence was expected due to the XRD analysis in **section 4.3.1** and it is attributed to the catalyst being exposed to air during Raman and XRD analysis.

Two peaks can be found at 520 and 605 cm^{-1} which do not correspond to any Cu or C vibration. This vibrations corresponds to the SiO_2 sample contamination that is shown in **figure 39**.¹⁰²

Below 750 cm^{-1} two more peaks can be encountered at 270 cm^{-1} and 348 cm^{-1} . The intensity of these two peaks compared to the background noise is lower than in the other 5 peaks, therefore they could be a false peak. However, these frequencies correspond to the Cu–CO vibrations modes, being 270 cm^{-1} the frustrated rotational mode of CO, and the 348 cm^{-1} the Cu–CO stretch vibration. Moreover, if we look at 2100 cm^{-1} , another small peak appear which correspond to the intramolecular CO stretching.^{47,103} The peaks are relatively low, and there is very low selectivity towards C products for the 30 nm NWs with nanopyramids at bias less cathodic than -1.1 V. Therefore, it is possible that the CO intermediate can be found at the surface of the catalyst at low negative overpotentials (-0.4V vs RHE), however it not possible to assure it.

Between the frequencies of 750 cm^{-1} and 1750 cm^{-1} a series of peaks can be seen that correspond to the vibrations of the ligand, oleylamine.¹⁰⁴ The presence of the ligand over the surface would be expected, as there has not been any negative bias applied to the surface or any other process that could eliminate the oleylamine from the catalyst surface. However, between the oleylamine peaks, we can encounter a specially predominant peak at 1065 cm^{-1} that is approximately the vibration frequency of carbonate (CO_3^-).¹⁰³ The presence of carbonate over the catalyst surface is expected as the electrolyte is 0.1 M KHCO_3 .

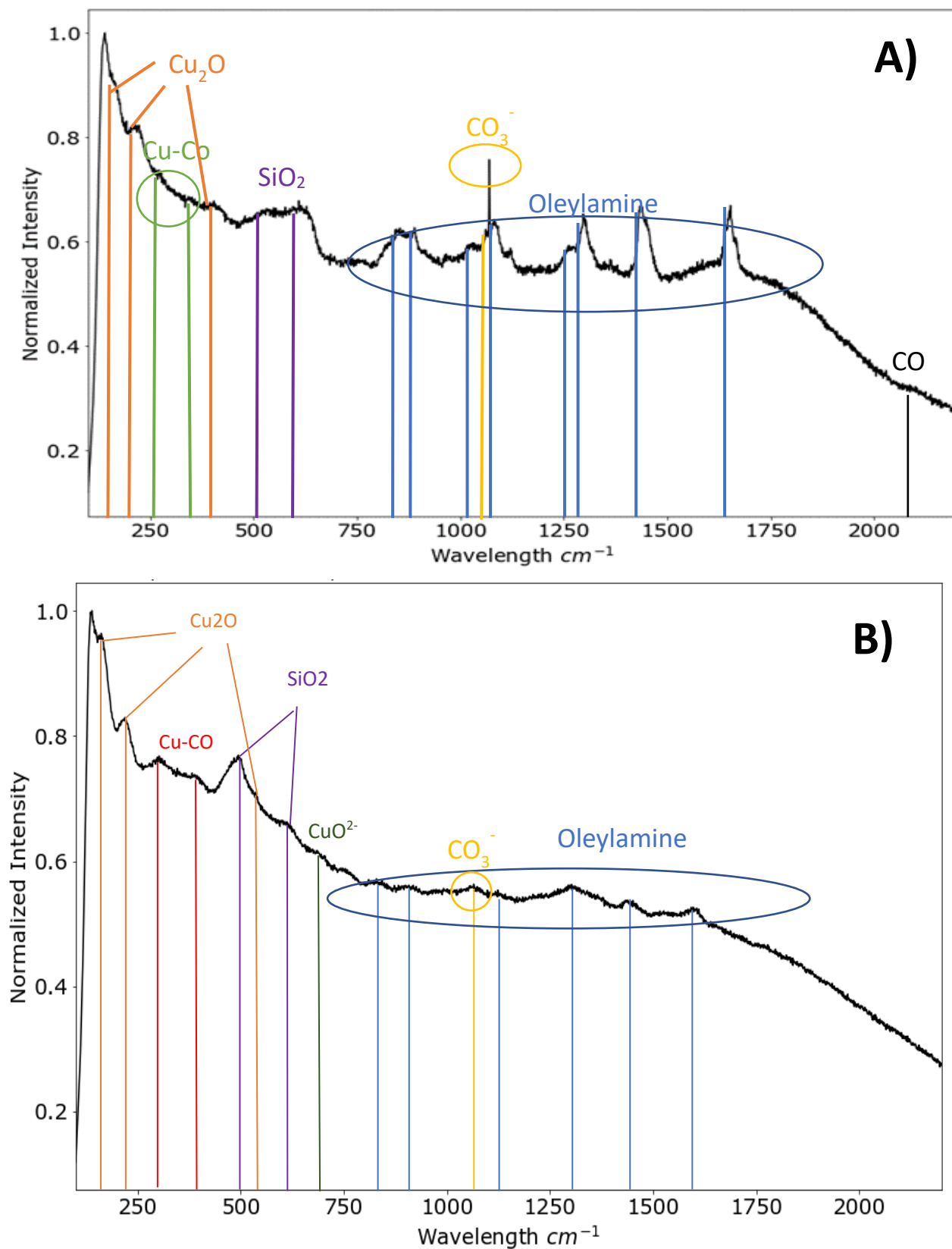


Figure 40: Raman scattering signal from the 30 nm NW with a secondary nucleation of nanopyramid catalyst. A) Signal after 30 seconds at -0.4 V Vs RHE before the Current Voltage experiments. B) Signal after 30 seconds at -1.1 V Vs RHE before the Current Voltage experiments

After the experiment at -0.4 V vs RHE for 30 seconds, 9 cycles of a cyclic-voltametry between 0.55 V to -0.9 V vs RHE were done to the same catalyst sample. After 112 minutes of activity the voltage was set at -1.1 V for 30 seconds, and all the vibrations were recorded in **figure 40 b)**.

In **figure 40 b)** all the vibration peaks that correspond to oleylamine have considerably decreased. Therefore, it is proven that after 112 minutes of CV between 0.55 V to -0.9 V vs RHE on the catalyst, there is a partial reduction of the oleylamine ligands from the surface.

There are still vibration peaks that correspond to Cu_2O at $160, 215$ and 530 cm^{-1} even though there is a high cathodic bias. The oxygen presence could be attributed to the formation of an oxide layer at anodic bias during the CV performed previously to this experiment. Moreover, the SiO_2 vibration are still present over the catalyst surface.

Due to the more cathodic bias, as we can already produce ethylene at -1.1 V , we can see the Cu-CO vibration at 290 and 372 cm^{-1} with a much higher intensity than at **figure 40 A)**. However, the vibration at 2100 cm^{-1} can not be found.

Finally, a new vibration peak appears at 701 cm^{-1} which corresponds to the CO^{2-} vibration. According to the bibliography is a possible intermediate for the creation of HCOO^* and, therefore, explain the selectivity toward formic acid of the 30 nm NWs with nanopyramids catalyst.¹⁰³

4.4.3 40 nm nanowires and multiple shapes nanoparticles

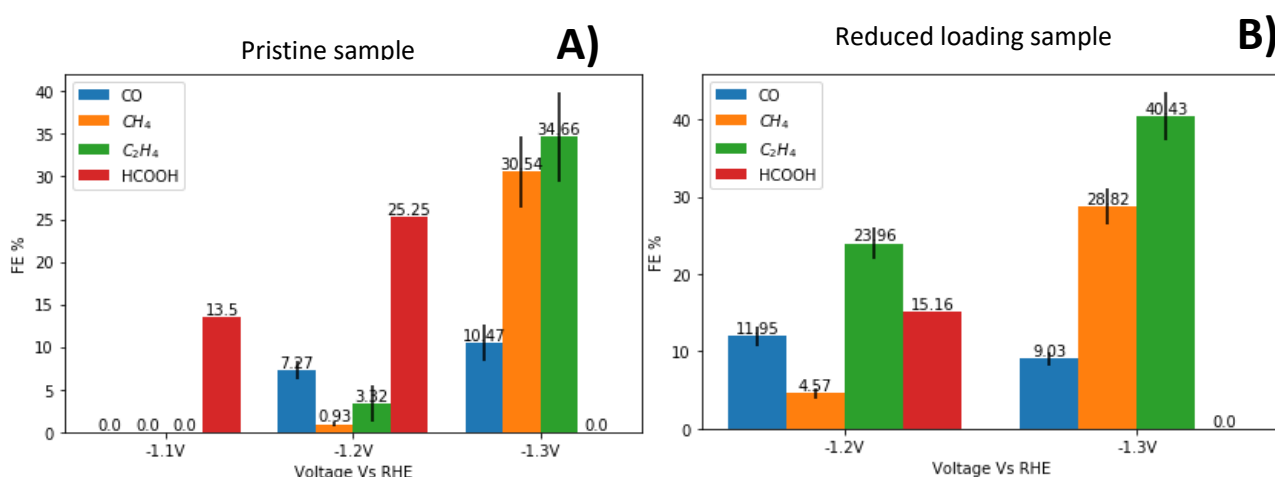


Figure 41: Average FE toward Carbon products from the last 10 injections from the catalyst formed by 40 nm nanowire and multiple shapes of nanoparticles A) Pristine sample and B) Reduced Loading sample

40 nm NW with multiple shape NPs is the most catalytically active sample from all the catalyst tested. This is proved in **figure 41** that shows a 75.67% and a 77.66% FE toward C products at -1.3V for both the pristine and the Reduced loading samples. However, both samples have a minimum of activity at -1.1 V , where the only product that could be found

was formic acid on the pristine sample. No selectivity towards CO, ethylene or methane was found for neither the pristine and the reduced loading sample even after several attempts. The current during all -1.1 V experiments was lower than -1 mA and stable. The FE for liquid product in the pristine sample implies that the formic acid is mainly produced by the NPs, as the reduced loading sample has low concentration of NPs even in comparison with the reduced loading samples of the other catalysts. Therefore, if the reduced loading sample, composed almost exclusively of nanowires, does not produce any Carbon product at -1.1V, the difference with the pristine sample has to be attributed to the NPs. Moreover, the high selectivity of the sample toward methane, with a maximum at -1.3 V of 31.4% with the pristine sample could be explained by high density of (111) facets as shown in the work of Hori et al.²⁴ Moreover, as showed in the review performed by Zhao *et al.*¹⁰⁵, there is a direct correlation between the increase in size of the Cu NPs with a higher tendency to create methane and ethylene.

At -1.2 V, the pristine sample produces mainly formic acid with a 25.3% FE meanwhile, the main product for the reduced loading sample is ethylene with a 24%. The principal component of the reduced loading sample are nanowires, which implies that the major producer of ethylene are the NWs. As shown in the work of Zhang *et al.*¹²⁵ the diameter of the NW has a great impact on the FE toward ethylene. Thicker nanowires with a diameter of 50 nm are 8 times more efficient for C₂ products than 20 nm NW due to an increase of the proportion area of (100) facets against the edge sites of the 5-fold NWs. Therefore, as the pristine sample has a higher proportion of NP and a very low FE towards ethylene (3.3%), we can conclude that the larger NPs are much more catalytically active than the NWs in the pristine sample at -1.2 V. The lack of activity at -1.1 V and the low activity of the NWs at -1.3 V imply that the catalyst need a high cathodic bias to be activated, even more cathodic than for both 30 nm NWs catalyst (**Figure 31 and 35**). Adding the low conductivity of the sample (less than -1 mA at -1.1 V) and that this catalyst is the one with the higher concentration of ligands during synthesis (10 mmol), suggest that the excess of ligand over the catalyst surface blocks the active sites of the catalyst at lower cathodic bias. Raman spectroscopy should be done over the 40 nm NWs with multi-shaped NPs to analyze the ligand removal.

At -1.3 V there is no liquid product in any of the samples. In the pristine sample, methane went from 0.93% at -1.2V to a, 30 times higher, 30.54%, and the ethylene went from 3.32% to 34.66%. On the other hand, the ethylene reached a FE of 40.43% for the reduced loading sample and methane went to 28.82%. According to Nie et al.⁹⁹ over the (111) surface, the top product at lower overpotentials is formic acid; however, at more cathodic bias the FE shifts from HCOOH to methane. This process would explain how at -1.2V in the pristine sample, formic acid is the main product with a 25.3% and at -1.3 V the methane production is over 30%. However, XRD experiments have to be done to only the NPs to be able to proof the (111) exposed facets or electron diffraction with HRTEM.

In the case of 40 nm NWs with multi-shaped NPs it seems that there is no increase in the reduction power of the catalyst with a higher concentration of nanoparticles. The reason can be attributed to different size of the nanoparticle, but also to the lack of intermediate transfer between NPs and NWs. The size of the NPs is linked with the surface's binding energy to different intermediate, which is the reason than according to Zhao *et al.*¹⁰⁵ larger nanoparticle had a higher tendency to create C₂ products and methane. A higher adsorption of CO* over the surface allows the reduction of the intermediate in the same NP to methane and avoid its transfer towards the NWs. Therefore, intermediates created on the NPs would not be able to continue their reduction toward ethylene over the NWs. Hence, we see the final product as not the synergy between two types of nanostructures but the sum of the products catalysed by two different catalyst phases. Nanoparticles with (111) facets mainly produce C₁ products and nanowires that mainly produce ethylene, as shown in the proposed mechanism in **figure 42**.

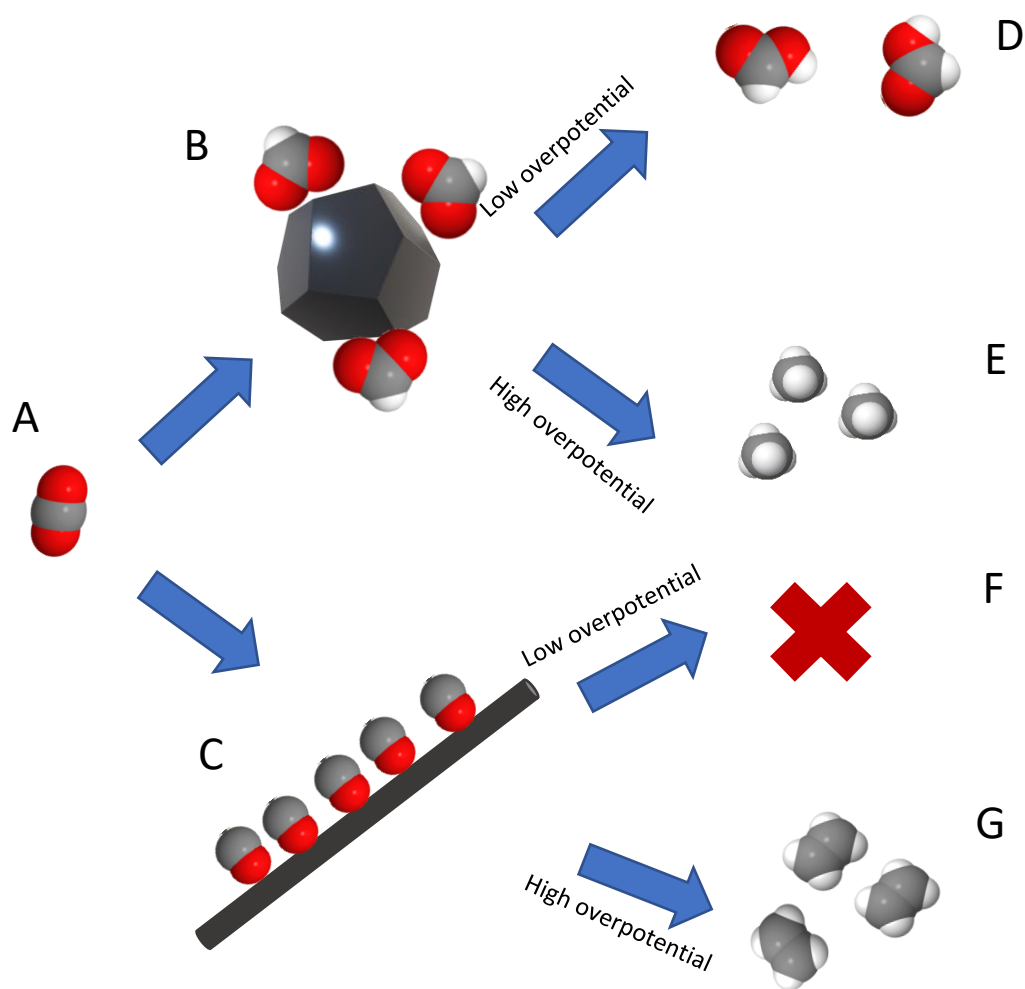


Figure 42: Reduction pathway mechanism for the reduction of CO over the the 30 nm NWs with multi-shaped nanoparticles catalyst

In **figure 42** is shown how CO_2 (A) can adhere to the NP (B) and be reduced to the COOH^* intermediate. If there is a low cathodic bias (-1.1 V or -1.2 V) the COOH^* intermediate becomes formic acid. However, if the cathodic bias is -1.3 V, the COOH^* becomes CO^* and then methane. Alternatively, CO_2 can adhere to the nanowire and be reduced to CO^* intermediate (C). If the overpotential is -1.1 there will be no product (F), however if the overpotential is -1.2 or -1.3 CO^* would be reduced to ethylene.

As we can observe in **figure 43**, the current and thus, the average current of both samples is stable except for a drastic change produced by the elimination of gas bubbles formed close to the cell's membrane. A differentiating characteristic of the 40 nm NW with irregular shape NP catalyst in comparison with the 30 nm NWs is that the current is more negative for the reduced loading sample than the pristine one.

Moreover, there is no current increase at the beginning of the experiment in neither the pristine sample or the reduced loading sample. The average current over the full experiment is stable with the exception of the two jumps in currents caused by the elimination of gas bubbles over the membrane's surface. Even more, the growth of FE towards ethylene rises rapidly and it slows down at 30 minutes in both samples, whereas for the 30 nm NWs the growth of the ethylene FE does not slow down until at least an hour. This differentiating characteristic could be attributed to two reasons. First, lack of reduction of the ligands over the catalyst surface which would also explain the low conductivity of the sample. Second, minor to no surface reconstruction. In the 30 nm NWs, we attributed the surface reconstruction to the elimination of edge sites and the migration of the NPs. In the 40 nm NWs with multi-shaped NPs the NWs and NPs are considerably larger than in both the other catalysts. The surface energy of the edge sites of larger nanoparticles is lower than in smaller nanoparticles and, therefore, more stables. In combination with the lower current during catalysis and the lower removal of ligands over the catalyst's surface is reasonable that the 40 nm NWs with multi-shaped NPs is more resistant to surface reconstruction.

Ethylene FE and current for 40 nm NW with irregular shape NP -1.3 V

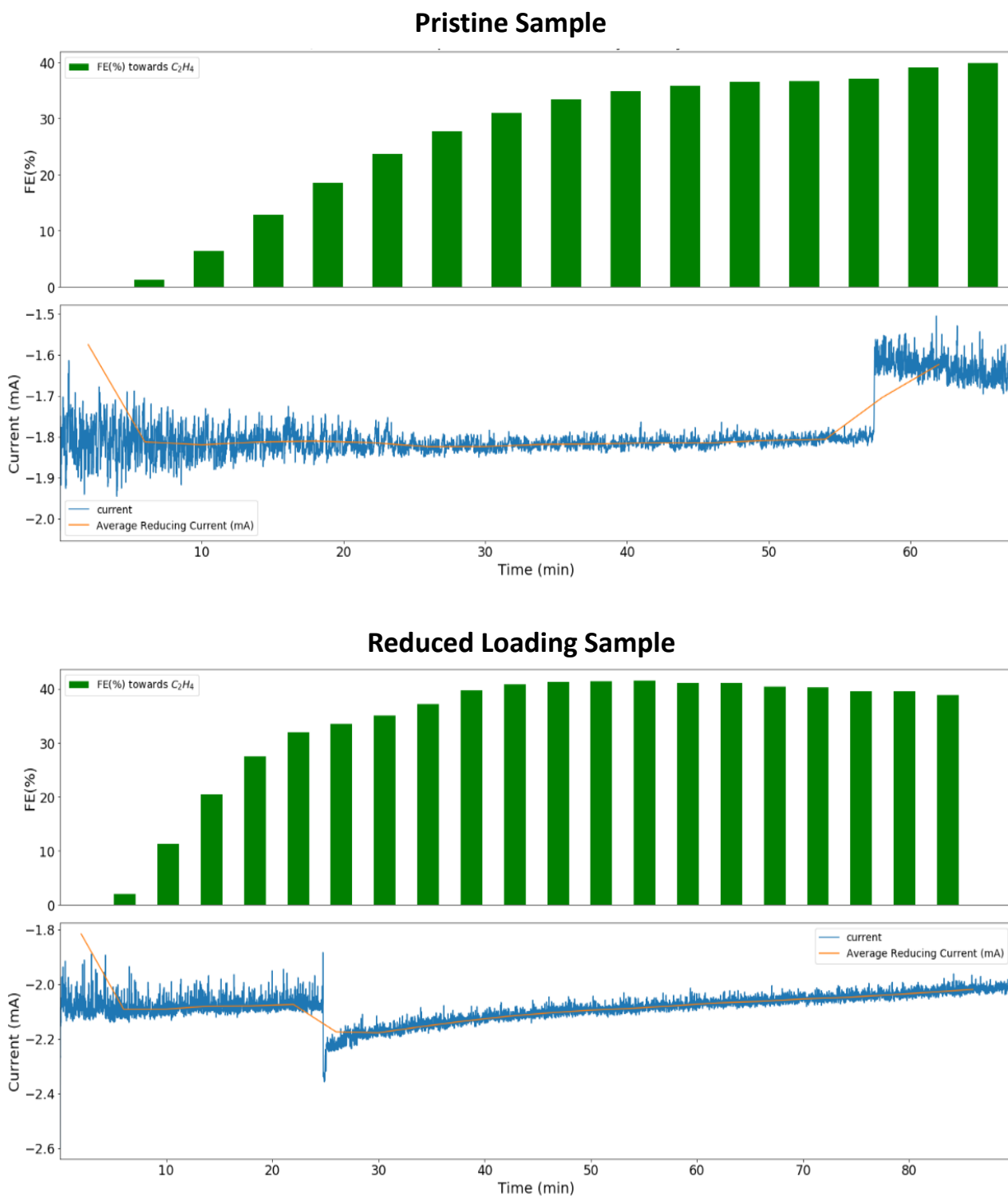


Figure 43: FE evolution of the Ethylene production against time during an activity experiment at -1.3 V using 30 nm NWs and multiple shape NPs as a catalyst and the current, and average current against time during the catalytic activity.

In the case of the 40 nm NWs with a secondary nucleation of multi-shaped NPs, there is also a considerable loss of material in comparison with the sample pre-activity (**figure 30 section 4.3.2**). Most of the aggregation of NPs have disappeared into the electrolyte and the NWs can be found individually without forming any time of bundle (see **figure 44 A**). However, as seen in **figure 42**, the current is stable during all catalysis and the selectivity towards C product increases over time, therefore the loss of material has to be immediate at the beginning of the experiment.

The size of the nanowires and the NP are respectively 45.74 ± 13.22 nm and 153.1 ± 53.6 nm. Both sizes are inside the standard deviation of the pre activity sample which are 40.27 ± 5.31 nm and 165 ± 49.5 nm respectively. On the EDX mapping, silicon contamination can be found over the electrode, which is attributed, as in the case of the 30 nm NWs with nanopyramids, to the SiO_2 polish powder used in the electrode preparation. As in the 30 nm NWs with nanopyramids catalyst, most of the oxygen is located over the silicon or the exposed glassy carbon, **figure 44 A) and B**). Therefore, as in the 30 nm NWs catalysts, it seems as the oxidation of the catalyst that we could see in the XRD analysis is principally located on the NPs and there is not a clear oxidation of the catalyst due to be exposed to air during activity for SEM analysis. However, HRTEM imaging should be done in the future to the catalyst sample after activity in order to identify the exposed facets of the surface in both the NWs and NPs and measuring the lattice distance of the exposed facets, it should be possible to determine if it is Cu^0 or it is oxidated as the crystal lattice depends on the element and its oxidation state.

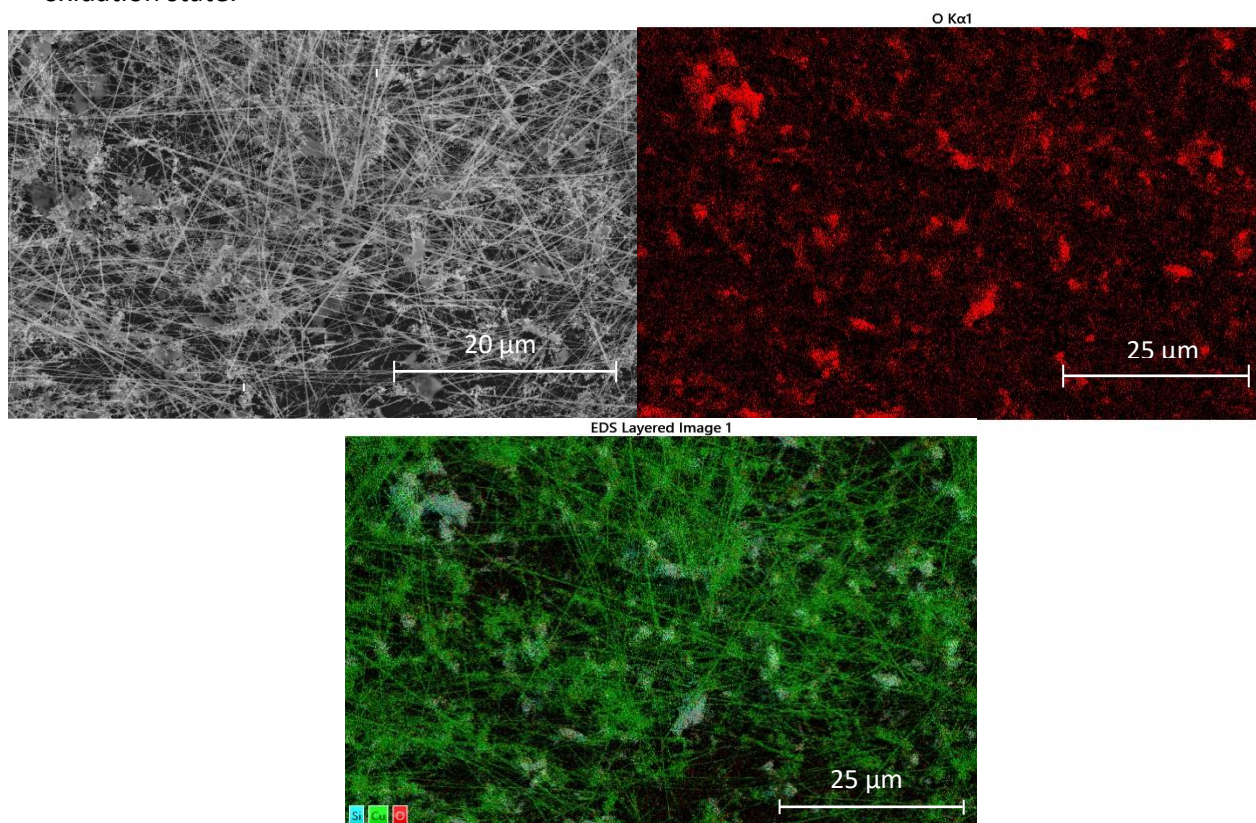


Figure 44: A) SEM image of the 40 nm NWs with multi-shaped NPs catalyst after 2 hours of activity at -1.3 V vs RHE. B) Superposition of the EDX mappings of the Cu element, O element and Si element on the same area of the catalyst. C) EDX mappings of the O element on the same area of the catalyst.

4.7 Comparison of the electrocatalytic performance between the different catalysts at -1.3 V vs RHE

Catalyst	Sample	Average current (mA)	Number of injections/time	FE toward ethylene during the last 10 injections	Total FE toward Carbon products	FE C ₂ products /FE C ₁ products
30 nm NWs with multi-shaped NPs	Pristine	-2.33	29 (116 min)	41.9%	64.9%	3.2
	Reduced Loading	-2.17	20 (80 min)	32.2%	54.3%	1.5
30 nm NWs with Nanopyramids	Pristine	-3.07	29(126 min)	25.7%	36%	2.5
	Reduced Loading	-1.8	20 (80 min)	20.3%	39.4%	1.1
40 nm NW with multi-shaped NPs	Pristine	-1.77	16 (64 min)	34.7%	76,7%	0.8
	Reduced Loading	-2.12	21(84 min)	40.4%	78.3%	1.7

Table 2: Electrocatalytic performance of the different catalyst.

In a general review of **Table 2**, we can see that the three different catalysts have several things in common at -1.3 V vs RHE.

The main product of all catalysts is ethylene, and the presence of C₂ product is between 3 (Pristine sample of 30 nm NW with multi-shaped NPs) to 0.8 times (Pristine 40 nm NW with multi-shaped NPs) higher than C₁ products. During the experiments of Hori *et al.*¹³ and Kuhl *et al.*⁴⁶, the maximum efficiency toward ethylene using polycrystalline Cu is 24% and with a high FE toward methane, CO, Formate and ethanol. The preferential growth presented in all catalyst samples in the (111) direction with (200) interplanar distance shown in the XRD analysis in section **4.3.1** support the idea that the exposed facets over the NWs surface is (100). In combination with the proven characteristic of the high selectivity toward ethylene of the Cu (100) exposed facets²⁴ we can conclude that all catalyst nanowires have (100) exposed facets which favour the selectivity towards ethylene

Another factor they have in common is the need for higher negative overpotentials to produce a high FE toward ethylene. During the experiments of Hori *et al.*¹³ and Kuhl *et al.*⁴⁶ with polycrystalline copper, the maximum FE towards ethylene when using bulk Copper can be found at -1.1 V vs RHE. Whereas in the NWs catalysts, a potential of -1.3 V vs RHE is needed to be able to surpass 25% FE. The closest one being the reduced loading sample of 40 nm NW with a 24% at -1.2 V. Even more, the current of all samples, with a maximum of $-3,07$ mA and a minimum of -1.77 mA at -1.3 V, is significantly lower than from bulk copper, which exceeds -18 mA at -1.2 V in the experiments of Kuhl *et al.*⁴⁶ This low current

could be due the presence of organic compounds (the ligands) over the catalyst surface. According Raman experiments performed over the 30 nm NWs with nanopyramids (**figure 40 section 4.4.2**) the ligands are partially removed due to the negative potentials. However, no organic molecules have been found in any of the NMR analysis of the catalyst after activity which could mean that a majority of the ligands resist reduction during activity. A better process of elimination of the ligands could be key for lowering the overpotential needed and increasing the exposed surface area. The dielectric barrier discharge plasma treatment, which eliminates the organic compounds using plasma, is a promising technique for future ligand removal experiments.¹⁰⁶

Comparing the catalyst composed by the 30 nm NWs with multi-shaped NPs and the 30 nm NWs with nanopyramids, we can see that in both cases, the presence of NPs significantly enhances the production of ethylene. In the pristine 30 nm NWs with multi-shaped NPs, the ethylene production triplicates (3.2) the production of C₁ products, but in the reduced loading sample, the production of C₂ products is only 1.5 times higher than C₁ products. However, in both the pristine and the reduced loading sample, the C₁ production remains similar with a 22% and a 22.1% respectively, being the main product CO. On the other hand, the 30 nm NWs with nanopyramids produced 2.5 times more ethylene in the pristine sample than C₁ but it is a 1:1 proportion at the reduced loading sample being the main C₁ product formic acid. Both catalysts have a similar XRD pattern and NW diameter. Therefore, the difference in FE has to be attributed to the different structure of the NPs. The (111) preferential growth causes that the sides of the nanopyramids have (111) exposed facets as seen in **figure 45**. Exposed (111) facets and experiments done with Cu nanopyramids with (111) facets show a high FE towards CH₄ and formic acid.^{24,98} However, in the 30 nm NWs with nanopyramids there is a low FE toward methane. Methane share the same intermediate as ethylene which is CO*, however formic acid is formed through the COOH* intermediate that instead of being reduced to CO* desorps the surface of the catalyst (see the proposed reaction mechanism in **figure 36**). The conclusion is that the CO* intermediate that would produce methane in the nanopyramids is being transferred to the (100) facets of the NWs and reduced toward ethylene. However, if we reduce the NPs concentration the interparticular distance increases and the intermediate transfer is reduced difficulting the reduction of COOH* to CO* to ethylene. Therefore, the difference between the 30 nm NWs with nanopyramids and the 30 nm NWs with multi-shaped NPs that justified the high selectivity of the pristine sample towards ethylene, is that in the multi-shaped NPs there is no COOH* to CO* step as the multi-shaped NPs don't produce formic acid but they do have a higher FE towards CO and methane (see the proposed reaction mechanism in **figure 34**). Thus, the limiting step is the transfer capacity of the CO* intermediates from the NPs towards the NWs, which justified the increase of CO production on the reduced loading sample.

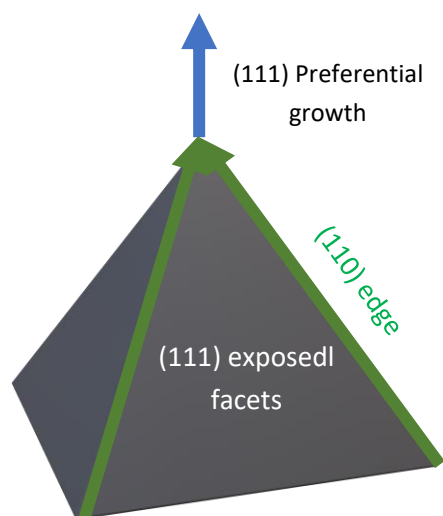


Figure 45: Surface structure of the Cu Nanopyramids

In the case of 40 nm NWs with multi-shaped NPs, we can observe that the trend is the opposite for the catalysts with 30 nm NWs. The FE towards ethylene is higher for the reduced loading sample (40.4%) than the pristine sample (34.7%). Moreover, the rate between C_2 products/ C_1 products is also the opposite of that with 30 nm NWs. In the pristine sample there are more C_1 products than C_2 with a proportion C_2/C_1 proportion of 0.8. Meanwhile, the reduced loading sample produces 1.7 times more C_2 products. Even more, at $-1.2V$, using the pristine sample, the main product is Formic acid (25,25%) with only a 3,32% FE toward ethylene. Nevertheless, the reduce loading sample has 15,16% for Formic Acid but 23,96% for Ethylene. Consequentially, we can infer that the NPs not only do not increase the FE towards ethylene of the NWs, but they decreased the reduction power of the catalyst. However, the pristine sample of the 40 nm NWs with multi-shaped NPs is the second highest producer of ethylene with a 40.4% only behind the pristine sample 30 nm NWs with multi-shaped NPs (41.9%). Therefore, if the NPs reduced the ethylene selectivity but the sample still produced 40% of ethylene we can conclude that 40 nm NWs have a higher selectivity toward ethylene than 30 nm NWs which is consistent with the research of Zhang *et al.*²⁷ who showed how 50 nm NWs had a considerably higher selectivity toward ethylene than the 25 nm NWs. In the 40 nm NWs with multi-shaped NPs the size of the NPs is 165 ± 49.5 nm whereas for the 30 nm NWs with multi-shaped NPs is 121.7 ± 13.6 . According to Zhao *et al.*¹⁰⁵ the increase in size of the NPs favours the production of methane and ethylene. The hypothesis is that the larger size of the NPs increases the adsorption energy of the CO^* intermediate over the NPs surface, which avoids its transfer to the NWs. Therefore the NPs lowers the FE of the NWs toward ethylene limiting its access to CO_2 as there is a competing adsorption reaction of the CO_2 over the NPs and NWs' surface as proposed in the reaction mechanism shown in **figure 42**.

Regarding the stability of the catalyst, Both the pristine samples of the catalysts composed of 30 nm NW and a secondary nucleation (multi-shaped or nanopyramids) were able to operate for 29 injections (116 minutes). However, there was a constant growth of the ethylene FE during the full experiment even though there is a considerable loss in catalyst material over the electrode surface after catalysis. Even more, in the pristine sample there is a slow shift towards less negative currents during the experiments even with the increase in ethylene. Whereas the reduced loading counterpart of the 30 nm NWs and multi-shaped NPs and the 30 nm NWs with nanopyramids, have a stable current during the full experiment and a slower and lower growth of ethylene production. These results indicate that the loss of material has to be immediate once the experiment commences and therefore does not affect negatively to the current or FE during the experiment, and that there is surface deformation during catalysis that favours the production of C₁ products. NWs and NPs are still present after catalysis as seen in the post-activity characterization in **figure 33 and 39**. Therefore the reconstruction is not creating bulk copper. In the work of Yifan *et al.*⁷⁸, During the electrocatalytic reduction of CO₂ using 20 nm 5-fold NWs with (100) exposed facets, they attributed the 10% shift on the FE between methane to ethylene after 20 minutes of activity to the surface reconstruction of the edge sites of the NWs. Therefore a possibility is that the shift in current and FE towards ethylene is due to the elimination of the edge sites during catalysis that affects principally the NPs, which would explain the stability of the reduced loading samples. However, XRD analysis or HRTEM imaging have to be done to the post catalysis sample measuring the exposed facets of the NPs and the NWs to be able to assure this. Another explanation could be the migration of the NPs over the catalyst surface over the electrode towards the NWs under catalysis conditions, reducing the inter-particle distance and favouring the exchange of intermediates between NPs and NWs. In **figure 33** we can see that all the NPs of the 30 nm NWs with multi-shaped NPs are found forming clusters around the NWs. However, in the case of the nanopyramids in figure 39 the NPs are more evenly distributed no definitive assessment can be done.

The pristine catalysis experiment of the 40 nm NWs with multi-shaped NPs pristine sample was stopped only after 16 injections (64 minutes). The current of the 40 nm NWs is more stable than the current of the 30 nm NWs samples and the ethylene growth stabilizes after 30 minutes whereas with the 30 nm NWs it takes longer than an hour. This suggests that there is no, or at least a low, catalyst's surface reconstruction. The larger size of the NPs and the NWs or the higher concentration of ligands attached to the surface (during catalysis, the 40 nm NWs use the highest concentration of Oleylamine, 10 mmol) could be the reason to the higher resistance of the surface to change its structure.

5. Conclusion and Outlook

The catalyst synthesized during our research had a secondary nucleation. Due to this condition, we proposed to answer the following questions:

- *Do the nanoparticles present in the nanowire catalyst enhance the FE towards ethylene of the nanowires?*

After reducing the nanoparticle loading using the size-selective precipitation method, we compared the electrocatalytic performance of each catalyst with its reduced loading version. This showed that the 30 nm NWs catalysts had a higher reduction power for CO₂ than the catalyst with lower nanoparticle concentration. The pristine sample of the 30 nm NWs catalysts had a higher FE toward Carbon products and significantly higher toward ethylene. However, it was also shown that the shape of the nanoparticles had a significant impact on the final product. Nanopyramids had a higher tendency to create the formic acid the multi-shaped nanoparticles had a higher tendency to catalyse CO*, therefore, the 30 nm NWs with multi-shaped NPs had a higher FE toward ethylene

Nevertheless, as seen for the 40 nm NWs catalyst, the NPs can also reduce the FE towards ethylene. The reduced loading sample of the 40 nm NWs with multi-shaped NPs have a higher FE toward ethylene than the pristine sample. Therefore, the presence of NPs on the pristine sample diminishes its reduction power. The reason is the CO₂'s competitive adsorption reaction over the NPs and the NWs, limiting the availability of CO₂ for its reduction to ethylene over the NWs surface.

Consequently, during this research we have demonstrated there is a strong impact in the final selectivity of the nanowires due to the presence of nanoparticles.

To further understand the synergy between nanowires and nanoparticles, it will be necessary to research the intermediates formed on the catalyst surface at -1.3 V to the three different catalysts. Raman spectroscopy was done over the 30 nm NWs with nanopyramids catalyst at -1.3 V, however the excess bubbling produced during the electrocatalysis made it impossible to detect the Raman scattering vibrations. The Raman spectroscopy over the 30 nm NWs with nanopyramids showed two vibration modes of the CO intermediate and presence of CO₂- which is considered an intermediate of HCOO*.¹⁰³ HCOO* produces formic acid that is the main product of the 30 nm NW with nanopyramids at -1.1 V. Comparing the peaks at -1.1 V, -1.2 V and -1.3 V would help understand the FE evolution and the state of the surface catalyst at operando conditions.

Moreover, we were not able to completely remove the nanoparticle loading from the catalyst sample. If we could analyse the FE carbon products of the NWs in isolation and the NPs in isolation, it would help us understand how the interaction between them really

affects the final product. A possible approach is the electrophoresis technique. Electrophoresis allows the nanoparticles' separation by their migration velocity inside a gel medium in an electric field.⁹⁰

- *How do different shapes and sizes of these nanostructures affect the nanowire's catalytic performance?*

From Raman spectroscopy and the selectivity of the different catalysts, we can draw several conclusions.

Nanoparticles with (111) exposed facets as the nanopyramids have a higher tendency to produce formic acid through the formation of HCOO* intermediate. Whereas multi-shaped NPs tend to produce the CO* intermediate and therefore increase the selectivity toward methane and ethylene.

Nanowires with larger diameter tend to have a higher FE to ethylene and are more catalytically active than nanowires with a smaller diameter, which agrees with Yifan *et al.*⁷⁸. On the other hand, larger nanoparticles in the presence of nanowires do not help to increase the total FE toward ethylene and mainly produce methane and, according to Zhao *et al.*, ethylene but at a lower FE than the NWs. However, the production of ethylene of the larger NPs without the presence of NWs should be studied to be able to confirm it.

The first step to understand the synergy between different sizes of NWs and NPs should be the characterization using HRTEM of the 120 nm multi-shaped NPs from the 30 nm NWs with multi-shaped NPs. Understanding the average exposed facets and the type and number of active sites would help us understand the reason of the high CO* production and its transfer to the NWs.

Another important experiment would be mixing the 40 nm NWs with the 120 nm multi-shaped NPs from the 30 nm NWs with multi-shaped NPs. If the high CO* intermediate production and transfers of intermediates towards the 40 nm NWs is similar to those to the 30 nm NWs a significant increase in FE over ethylene can be expected.

- *What is the stability of Cu anisotropic NPs, like NWs, under operando conditions? Does the presence of other nanostructures with different shapes have an effect on the stability of the catalyst?*

Both the pristine samples of the catalysts with 30 nm NWs (with multi-shaped NPs and with nanopyramids) were able to perform for 2 hours with a constant increase of the FE toward ethylene. However, in both pristine samples there is a current shift towards more positive current due to surface reconstruction. This surface reconstruction can be the etching of edge sites, the migration of nanoparticles towards the nanowires or both. Meanwhile, the reduced loading samples of both catalysts started to reduce its FE toward ethylene after 70

minutes of activity, still, the current is stable during the full duration of the experiment. Thus, in the case of the multi-shaped nanoparticles and the nanopyramids in conjunction with 30 nm NWs, the nanoparticles affect the current stability of the catalyst even though it enhances the selectivity towards ethylene. Therefore, longer electrocatalysis experiments with a duration of 4+ hours should be done to the pristine samples of the 30 nm NWs with multi-shaped NPs and the 30 nm NWs with nanopyramids to be able to know if the current shift eventually stabilizes or if it is a continuous current degradation.

In the case of the catalyst with 40 nm NWs, the FE towards ethylene of the reduced loading sample began to decrease after only 50 minutes of activity. However, the current is stable during the full experiments in both the pristine sample and the reduced loading sample. Therefore, the bigger NPs do not have a impact on the stability of the sample, probably due to resistance to surface deformation.

Due to the loss of material across the catalyst support during catalysis, XRD analysis after activity was not possible due to the received signal was too low. Therefore, we cannot know what the oxidation state of the catalyst was, whether there was a loss of the (100) exposed facets or whether new facets appeared during catalysis. ECSA studies should be done before and after the catalysis experiments to determine when this loss of material occurs and HRTEM imaging of the NPs and NWs after catalysis would indicate the oxidation state and exposed facets of the Cu nanostructures.

In conclusion, it has been proved that the NPs impact the final selectivity of the NWs. This impact can be an enhancement or a reduction depending on the structure and size of these nanoparticles. The structure and size of the nanoparticles determine the type of intermediates created during catalysis conditions and how they can interact with the NWs to transfer those intermediates. Finally, also depending on the size and structure, the nanoparticles impact the catalyst stability. Smaller nanoparticles are more vulnerable to surface reformation during operando conditions which impact the average current density and the selectivity of the catalyst.

6. Acknowledgements

First and foremost, I would like to thank Dr. Ward Van der Stam for his guidance and patience. Thanks to him and the opportunity he has given me, I have strengthened my passion for research and discovered a field of research that is as interesting as it is important. More than that, I am especially grateful for the opportunity to work with such a vibrant and passionate group of people as the Electrobuzz team.

Second, Thanks to Shuang Yang for all the time, effort and dedication that she devoted helping me improve as a scientist, even when before being my daily supervisor. Without her help this thesis would not have been possible.

I would also like to thank the inestimable help that Jim de Ruiten gave me during the worst part of the covid pandemic. Without his help and selfless supervision, I would have not been able to work in the lab for months. Moreover, his help with the Raman spectroscopy and his lessons about python made my work not only easier but also much more interesting.

Thanks to Kees Kolmeijer, that even though he was a master student like me, he also dedicated time and energy to help me understand not only the lab procedures but also about the Dutch culture. He taught me from all his successes and mistakes during his thesis and made my research path much easier.

Additionally, I would like to appreciate the help that Dr Longfei Wu and Dr Hongyu An for dedicating their time in helping me understand XRD and Raman spectroscopy. And for their patience and help when answering all my question.

Finally, I would like to thank Joris Janssens for giving me a hand in my constant battle against the Schenk line, and to Dr Jochem Wijten for all the hours he spends in from of the TEM and SEM so I could have such wonderful images of my nanowires.

7. References

1. Environmental Protection Agency, U. S. Global Greenhouse Gas Emissions Data. <https://www.epa.gov/ghgemissions/global-greenhouse-gas-emissions-data> (2014).
2. Quiancheng, M. Greenhouse Gases: Refining the Role of Carbon Dioxide. *nasa.gov* https://www.giss.nasa.gov/research/briefs/ma_01/ (1998).
3. Climate Nasa. Carbon dioxide. <https://climate.nasa.gov/vital-signs/carbon-dioxide/> (2020).
4. Stips, A., Maclas, D., Coughlan, C., Garcia-Gorriz, E. & Liang, X. S. On the causal structure between CO₂ and global temperature. *Sci. Rep.* **6**, 1–9 (2016).
5. RECS. European 20-20-20 Targets.
6. Khan, Z., Ali, S., Umar, M., Kirikkaleli, D. & Jiao, Z. Consumption-based carbon emissions and International trade in G7 countries: The role of Environmental innovation and Renewable energy. *Sci. Total Environ.* **730**, 138945 (2020).
7. Center for Climate and energy solutions. Renewable Energy. <https://www.c2es.org/content/renewable-energy/> (2020).
8. Denholm, P., Kulcinski, G. L. & Holloway, T. Emissions and energy efficiency assessment of baseload wind energy systems. *Environ. Sci. Technol.* **39**, 1903–1911 (2005).
9. Denholm, P. & Margolis, R. M. Evaluating the limits of solar photovoltaics (PV) in electric power systems utilizing energy storage and other enabling technologies. *Energy Policy* **35**, 4424–4433 (2007).
10. Ziegler, M. S. *et al.* Storage Requirements and Costs of Shaping Renewable Energy Toward Grid Decarbonization. *Joule* **3**, 2134–2153 (2019).
11. De Luna, P. *et al.* What would it take for renewably powered electrosynthesis to displace petrochemical processes? *Science (80-.)*. **364**, (2019).
12. Hori, Y., Kikuchi, K., Murata, A. & Suzuki, S. Production of Methane and Ethylene in Electrochemical Reduction of Carbon Dioxide At Copper Electrode in Aqueous Hydrogencarbonate Solution. *Chem. Lett.* **15**, 897–898 (1986).
13. Hori, Y., Murata, A. & Takahashi, R. Formation of hydrocarbons in the electrochemical reduction of carbon dioxide at a copper electrode in aqueous solution. *J. Chem. Soc. Faraday Trans. 1 Phys. Chem. Condens. Phases* **85**, 2309–2326 (1989).
14. Bagger, A., Ju, W., Varela, A. S., Strasser, P. & Rossmeisl, J. Electrochemical CO₂ Reduction: A Classification Problem. *ChemPhysChem* **18**, 3266–3273 (2017).

15. Handoko, A. D., Wei, F., Jenndy, Yeo, B. S. & Seh, Z. W. Understanding heterogeneous electrocatalytic carbon dioxide reduction through operando techniques. *Nat. Catal.* **1**, 922–934 (2018).
16. Xiao, T. *et al.* The Catalyst Selectivity Index (CSI): A Framework and Metric to Assess the Impact of Catalyst Efficiency Enhancements upon Energy and CO₂ Footprints. *Top. Catal.* **58**, 682–695 (2015).
17. Huang, J. & Buonsanti, R. Colloidal Nanocrystals as Heterogeneous Catalysts for Electrochemical CO₂ Conversion †. *Chem. Mater.* **31**, 13–25 (2019).
18. Choi, J. *et al.* Energy efficient electrochemical reduction of CO₂ to CO using a three-dimensional porphyrin/graphene hydrogel. *Energy Environ. Sci.* **12**, 747–755 (2019).
19. Geyer, R., Jambeck, J. R. & Law, K. L. Production, use, and fate of all plastics ever made. *Sci. Adv.* **3**, 25–29 (2017).
20. Brems, A., Dewil, R., Baeyens, J. & Zhang, R. Gasification of plastic waste as waste-to-energy or waste-to-syngas recovery route. *Nat. Sci.* **05**, 695–704 (2013).
21. Murata, A. & Hori, Y. Product selectivity affected by cationic species in electrochemical reduction of CO₂ and CO at a Cu electrode. *Bulletin of the Chemical Society of Japan* vol. 64 123–127 (1991).
22. Loiudice, A. *et al.* Tailoring Copper Nanocrystals towards C₂ Products in Electrochemical CO₂ Reduction. *Angew. Chemie - Int. Ed.* **55**, 5789–5792 (2016).
23. Guntern, Y. T. *et al.* Colloidal Nanocrystals as Electrocatalysts with Tunable Activity and Selectivity. *ACS Catal.* 1248–1295 (2021)
doi:10.1021/acscatal.0c04403.
24. Hori, Y., Takahashi, I., Koga, O. & Hoshi, N. Electrochemical reduction of carbon dioxide at various series of copper single crystal electrodes. *J. Mol. Catal. A Chem.* **199**, 39–47 (2003).
25. Manthiram, K., Beberwyck, B. J. & Alivisatos, A. P. Enhanced electrochemical methanation of carbon dioxide with a dispersible nanoscale copper catalyst. *J. Am. Chem. Soc.* **136**, 13319–13325 (2014).
26. Wang, Z., Yang, G., Zhang, Z., Jin, M. & Yin, Y. Selectivity on Etching: Creation of High-Energy Facets on Copper Nanocrystals for CO₂ Electrochemical Reduction. *ACS Nano* **10**, 4559–4564 (2016).
27. Zhang, H. *et al.* Cu nanowire-catalyzed electrochemical reduction of CO or CO₂. *Nanoscale* **11**, 12075–12079 (2019).
28. Yang, H. J., He, S. Y. & Tuan, H. Y. Self-seeded growth of five-fold twinned copper nanowires: Mechanistic study, characterization, and SERS applications. *Langmuir* **30**, 602–610 (2014).

29. Leeuwen, P. W. N. M. History of catalysis. *Stud. Surf. Sci. Catal.* **79**, 3–21 (1993).
30. Armor, J. N. A history of industrial catalysis. *Catal. Today* **163**, 3–9 (2011).
31. Penczek, S. *et al.* Glossary of terms related to kinetics, thermodynamics, and mechanisms of polymerization (IUPAC Recommendations 2008). *Pure Appl. Chem.* **80**, 2163–2193 (2008).
32. Hagen, J. *Concepts of Modern Catalysis and Kinetics Catalysis from A to Z Principles and Practice of Heterogeneous Catalysis Catalytic Membranes and Membrane Reactors Spectroscopy in Catalysis.* Wiley-VCH (2006).
33. Schlögl, R. Heterogeneous catalysis. *Angew. Chemie - Int. Ed.* **54**, 3465–3520 (2015).
34. Pines, H. & Haag, W. O. Alumina: Catalyst and Support. I. Alumina, its Intrinsic Acidity and Catalytic Activity. *J. Am. Chem. Soc.* **82**, 2471–2483 (1960).
35. Dai, H. *et al.* Finned zeolite catalysts. *Nat. Mater.* **19**, 1074–1080 (2020).
36. Kumar, K. V., Porkodi, K. & Rocha, F. Langmuir-Hinshelwood kinetics - A theoretical study. *Catal. Commun.* **9**, 82–84 (2008).
37. Fertig, M. Finite Rate Surface Catalysis Modelling of Pm1000 and Sic. *Proc. 8th Eur. Symp. Aerothermodyn. Sp. Veh.* (2015).
38. Roduner, E. Selected fundamentals of catalysis and electrocatalysis in energy conversion reactions—A tutorial. *Catal. Today* **309**, 263–268 (2018).
39. Georgia State University. Electrochemical Cell. <http://hyperphysics.phy-astr.gsu.edu/hbase/Chemical/electrochem.html#c3>.
40. Georgia State University. Electrocatalytic Cell. <http://hyperphysics.phy-astr.gsu.edu/hbase/Chemical/electrolyt.html#c1>.
41. Wipf, D. O. Ohmic drop compensation in voltammetry: Iterative correction of the applied potential. *Anal. Chem.* **68**, 1871–1876 (1996).
42. Pavlishchuk, V. V. & Addison, A. W. Conversion constants for redox potentials measured versus different reference electrodes in acetonitrile solutions at 25°C. *Inorganica Chim. Acta* **298**, 97–102 (2000).
43. Ciobanu, M., Wilburn, J. P., Krim, M. L., Cliffel, D. E. & Electrochemistry, C. I. N. Fundamentals. (1893) doi:10.1016/B978-0-444-51958-0.50002-1.
44. Cai, Y. & Anderson, A. B. The reversible hydrogen electrode: Potential-dependent activation energies over platinum from quantum theory. *J. Phys. Chem. B* **108**, 9829–9833 (2004).
45. Nitopi, S. *et al.* Progress and Perspectives of Electrochemical CO₂ Reduction on Copper in Aqueous Electrolyte. *Chem. Rev.* **119**, 7610–7672 (2019).
46. Kuhl, K. P., Cave, E. R., Abram, D. N. & Jaramillo, T. F. New insights into the

- electrochemical reduction of carbon dioxide on metallic copper surfaces. *Energy Environ. Sci.* **5**, 7050–7059 (2012).
47. Jin, L. & Seifitokaldani, A. In situ spectroscopic methods for electrocatalytic CO₂ reduction. *Catalysts* **10**, (2020).
 48. Schouten, K. J. P., Qin, Z., Gallent, E. P. & Koper, M. T. M. Two pathways for the formation of ethylene in CO reduction on single-crystal copper electrodes. *J. Am. Chem. Soc.* **134**, 9864–9867 (2012).
 49. Bockris, J. O. & Potter, E. C. The Mechanism of the Cathodic Hydrogen Evolution Reaction. *J. Electrochem. Soc.* **99**, 169 (1952).
 50. Birdja, Y. Y. *et al.* Advances and challenges in understanding the electrocatalytic conversion of carbon dioxide to fuels. *Nat. Energy* **4**, 732–745 (2019).
 51. Garza, A. J., Bell, A. T. & Head-Gordon, M. Mechanism of CO₂ Reduction at Copper Surfaces: Pathways to C₂ Products. *ACS Catal.* **8**, 1490–1499 (2018).
 52. DeWulf, D. W., Jin, T. & Bard, A. J. Electrochemical and Surface Studies of Carbon Dioxide Reduction to Methane and Ethylene at Copper Electrodes in Aqueous Solutions. *J. Electrochem. Soc.* **136**, 1686–1691 (1989).
 53. Harley, J., Nel, W. & Pretorius, V. Flame ionization detector for gas chromatography [3]. *Nature* **181**, 177–178 (1958).
 54. Fulmer, G. R. *et al.* NMR chemical shifts of trace impurities: Common laboratory solvents, organics, and gases in deuterated solvents relevant to the organometallic chemist. *Organometallics* **29**, 2176–2179 (2010).
 55. Scholar, A. Crystalline structure of cellulose. *Nature* **139**, 599–600 (1937).
 56. Mayrhofer, K. J. Oxygen Reduction and Carbon Monoxide Oxidation on Pt - from Model to Real Systems for Fuel Cell Electrocatalysis. (2006).
 57. Calle-Vallejo, F. & Koper, M. T. M. Theoretical considerations on the electroreduction of CO to C₂ Species on Cu(100) electrodes. *Angew. Chemie - Int. Ed.* **52**, 7282–7285 (2013).
 58. Stephens, I. E. L., Bondarenko, A. S., Grønbjerg, U., Rossmeisl, J. & Chorkendorff, I. Understanding the electrocatalysis of oxygen reduction on platinum and its alloys. *Energy Environ. Sci.* **5**, 6744–6762 (2012).
 59. Farias, M. J. S. & Feliu, J. M. Determination of Specific Electrocatalytic Sites in the Oxidation of Small Molecules on Crystalline Metal Surfaces. *Top. Curr. Chem.* **377**, 1–22 (2019).
 60. Reske, R., Mistry, H., Behafarid, F., Roldan Cuenya, B. & Strasser, P. Particle size effects in the catalytic electroreduction of CO₂ on Cu nanoparticles. *J. Am. Chem. Soc.* **136**, 6978–6986 (2014).
 61. Varela, A. S., Kroschel, M., Reier, T. & Strasser, P. Controlling the selectivity of

- CO₂ electroreduction on copper: The effect of the electrolyte concentration and the importance of the local pH. *Catal. Today* **260**, 8–13 (2016).
62. Suen, N. T. *et al.* Electrocatalysis for the oxygen evolution reaction: Recent development and future perspectives. *Chem. Soc. Rev.* **46**, 337–365 (2017).
 63. Raciti, D., Mao, M., Park, J. H. & Wang, C. Local pH Effect in the CO₂ Reduction Reaction on High-Surface-Area Copper Electrocatalysts. *J. Electrochem. Soc.* **165**, F799–F804 (2018).
 64. Lasia, A., Lamm, A. & Gasteiger, H. A. Hydrogen evolution reaction Chapter 29 Hydrogen evolution reaction. **2**, 416–440 (2003).
 65. Singh, M. R., Clark, E. L. & Bell, A. T. Effects of electrolyte, catalyst, and membrane composition and operating conditions on the performance of solar-driven electrochemical reduction of carbon dioxide. *Phys. Chem. Chem. Phys.* **17**, 18924–18936 (2015).
 66. Ma, M., Djanashvili, K. & Smith, W. A. Controllable Hydrocarbon Formation from the Electrochemical Reduction of CO₂ over Cu Nanowire Arrays. *Angew. Chemie - Int. Ed.* **55**, 6680–6684 (2016).
 67. Gupta, N., Gattrell, M. & MacDougall, B. Calculation for the cathode surface concentrations in the electrochemical reduction of CO₂ in KHCO₃ solutions. *J. Appl. Electrochem.* **36**, 161–172 (2006).
 68. Kas, R., Kortlever, R., Yilmaz, H., Koper, M. T. M. & Mul, G. Manipulating the Hydrocarbon Selectivity of Copper Nanoparticles in CO₂ Electroreduction by Process Conditions. *ChemElectroChem* **2**, 354–358 (2015).
 69. Ma, M., Djanashvili, K. & Smith, W. A. Selective electrochemical reduction of CO₂ to CO on CuO-derived Cu nanowires. *Phys. Chem. Chem. Phys.* **17**, 20861–20867 (2015).
 70. Yang, H. J., He, S. Y. & Tuan, H. Y. Self-seeded growth of five-fold twinned copper nanowires: Mechanistic study, characterization, and SERS applications. *Langmuir* **30**, 602–610 (2014).
 71. Ha, D. H. *et al.* Activity and stability of cobalt phosphides for hydrogen evolution upon water splitting. *Nano Energy* **29**, 37–45 (2016).
 72. Wang, C., Daimon, H., Onodera, T., Koda, T. & Sun, S. A general approach to the size- and shape-controlled synthesis of platinum nanoparticles and their catalytic reduction of oxygen. *Angew. Chemie - Int. Ed.* **47**, 3588–3591 (2008).
 73. Pachón, L. D. & Rothenberg, G. Transition-metal nanoparticles: Synthesis, stability and the leaching issue. *Appl. Organomet. Chem.* **22**, 288–299 (2008).
 74. Jia, C. J. & Schüth, F. Colloidal metal nanoparticles as a component of designed catalyst. *Phys. Chem. Chem. Phys.* **13**, 2457–2487 (2011).
 75. Turkevich, J., Stevenson, P. C. & Hillier, J. A study of the nucleation and growth

- processes in the synthesis of colloidal gold. *Discuss. Faraday Soc.* **11**, 55–75 (1951).
76. Ghosh, S. & Manna, L. The Many ‘facets’ of Halide Ions in the Chemistry of Colloidal Inorganic Nanocrystals. *Chem. Rev.* **118**, 7804–7864 (2018).
 77. Jin, M. *et al.* Shape-controlled synthesis of copper nanocrystals in an aqueous solution with glucose as a reducing agent and hexadecylamine as a capping agent. *Angew. Chemie - Int. Ed.* **50**, 10560–10564 (2011).
 78. Li, Y. *et al.* Structure-Sensitive CO₂ Electroreduction to Hydrocarbons on Ultrathin 5-fold Twinned Copper Nanowires. *Nano Lett.* **17**, 1312–1317 (2017).
 79. Cui, F. *et al.* Synthesis of Ultrathin Copper Nanowires Using Tris(trimethylsilyl)silane for High-Performance and Low-Haze Transparent Conductors. *Nano Lett.* **15**, 7610–7615 (2015).
 80. Cuya Huaman, J. L., Urushizaki, I. & Jeyadevan, B. Large-scale Cu nanowire synthesis by PVP-ethylene glycol route. *J. Nanomater.* **2018**, (2018).
 81. Wiley, B., Herricks, T., Sun, Y. & Xia, Y. Polyol synthesis of silver nanoparticles: Use of chloride and oxygen to promote the formation of single-crystal, truncated cubes and tetrahedrons. *Nano Lett.* **4**, 1733–1739 (2004).
 82. Ruan, H. *et al.* Study on synthesis and growth mechanism of copper nanowires via a facile oleylamine-mediated process. *J. Mater. Sci. Mater. Electron.* **27**, 9405–9409 (2016).
 83. You, H., Liu, X., Liu, H. & Fang, J. Theoretical description of the role of amine surfactant on the anisotropic growth of gold nanocrystals. *CrystEngComm* **18**, 3934–3941 (2016).
 84. Tovstun, S. A. & Razumov, V. F. Theory of size-selective precipitation. *J. Nanoparticle Res.* **19**, (2017).
 85. Baldi, P. *Brownian Motion.* (2017).
 86. Yang, J., Choi, M. K., Kim, D. H. & Hyeon, T. Designed Assembly and Integration of Colloidal Nanocrystals for Device Applications. *Adv. Mater.* **28**, 1176–1207 (2016).
 87. Huang, H. H. *et al.* Synthesis, characterization, and nonlinear optical properties of copper nanoparticles. *Langmuir* **13**, 172–175 (1997).
 88. Savinova, E. R., Chuvilin, A. L. & Parmon, V. N. Copper colloids stabilized by water-soluble polymers. Part I. Preparation and properties. *J. Mol. Catal.* **48**, 217–229 (1988).
 89. Lisiecki, I., Billoudet, F. & Pileni, M. P. Control of the shape and the size of copper metallic particles. *J. Phys. Chem.* **100**, 4160–4166 (1996).
 90. Surugau, N. & Urban, P. L. Electrophoretic methods for separation of

- nanoparticles. *J. Sep. Sci.* **32**, 1889–1906 (2009).
91. Soliman, H. M. A. & Abdel-Rahman, H. H. The use of rotating cylinder electrode to study the effect of 1,3-dihydroxypropane on the production of copper powder. *J. Braz. Chem. Soc.* **17**, 705–714 (2006).
 92. Zhao, Y. *et al.* Large-scale synthesis of Cu nanowires with gradient scales by using ‘hard’ strategies and size effects on electrical properties. *CrystEngComm* **15**, 332–342 (2013).
 93. Zhang, X. G., Jin, X., Wu, D. Y. & Tian, Z. Q. Selective Electrocatalytic Mechanism of CO₂ Reduction Reaction to CO on Silver Electrodes: A Unique Reaction Intermediate. *J. Phys. Chem. C* **122**, 25447–25455 (2018).
 94. Raciti, D. Mass Transfer Effects in CO₂ Reduction on Cu Nanowire Electrocatalysts. *Catal. Sci. Technol.* **2019-Novem**, (2019).
 95. Dupont, M., Hollenkamp, A. F. & Donne, S. W. Electrochemically active surface area effects on the performance of manganese dioxide for electrochemical capacitor applications. *Electrochim. Acta* **104**, 140–147 (2013).
 96. Gupta, K., Bersani, M. & Darr, J. A. Highly efficient electro-reduction of CO₂ to formic acid by nano-copper. *J. Mater. Chem. A* **4**, 13786–13794 (2016).
 97. Guo, S. *et al.* Cu-CDots nanocorals as electrocatalyst for highly efficient CO₂ reduction to formate. *Nanoscale* **9**, 298–304 (2017).
 98. Liu, Y., Qiu, H., Li, J., Guo, L. & Ager, J. W. Tandem Electrocatalytic CO₂ Reduction with Efficient Intermediate Conversion over Pyramid-Textured Cu–Ag Catalysts. *ACS Appl. Mater. Interfaces* **13**, 40513–40521 (2021).
 99. Nie, X., Luo, W., Janik, M. J. & Asthagiri, A. Reaction mechanisms of CO₂ electrochemical reduction on Cu(1 1 1) determined with density functional theory. *J. Catal.* **312**, 108–122 (2014).
 100. Qian, C. *et al.* Catalytic CO₂ reduction by palladium-decorated silicon–hydride nanosheets. *Nat. Catal.* **2**, 46–54 (2019).
 101. Deng, Y., Handoko, A. D., Du, Y., Xi, S. & Yeo, B. S. In Situ Raman Spectroscopy of Copper and Copper Oxide Surfaces during Electrochemical Oxygen Evolution Reaction: Identification of Cu^{II} Oxides as Catalytically Active Species. *ACS Catal.* **6**, 2473–2481 (2016).
 102. Borowicz, P., Taube, A., Rzodkiewicz, W., Latek, M. & Gieratowska, S. Raman spectra of high-κ dielectric layers investigated with micro-Raman spectroscopy comparison with silicon dioxide. *Sci. World J.* **2013**, (2013).
 103. Jiang, S., Klingan, K., Pasquini, C. & Dau, H. New aspects of operando Raman spectroscopy applied to electrochemical CO₂ reduction on Cu foams. *J. Chem. Phys.* **150**, (2019).
 104. Baranov, D. *et al.* Purification of Oleylamine for Materials Synthesis and

- Spectroscopic Diagnostics for trans Isomers. *Chem. Mater.* **31**, 1223–1230 (2019).
105. Zhao, J. *et al.* An overview of Cu-based heterogeneous electrocatalysts for CO₂ reduction. *J. Mater. Chem. A* **8**, 4700–4734 (2020).
 106. Tan, Y. *et al.* Effective removal of the protective ligands from Au nanoclusters by ambient pressure nonthermal plasma treatment for CO oxidation. *Cuihua Xuebao/Chinese J. Catal.* **39**, 929–936 (2018).

8. Annex A

Colloidal synthesis used to optimize the synthetization of the Cu NWs catalysts.

Salt Source	Mmol Salt	Mmol Olam	Mmol TOA	Growth Temperature	Time (h)	Result
CuOAc	1	5	2	180	3	10 nm nanoparticles and microstructures
CuOaC	1	6	2,5	180	3	Nanoparticles And microstructures
CuOAc + CuCl	0,85 + 0,15	6	2,5	180	3	Nanoparticles and nanorods
CuBr	1	6	2,5	180	3	
CuCl	1	7	2,5	180	3	Nanowire and nanoparticles
CuCl	1	2.5	6	180° C	4	Bulk copper
CuCl	1	2.5	6	200° C	3	Bulk copper
CuCl	1	2.5	6	160° C	3	No nanoparticle formation
CuCl₂	1	2.5	8	180° C	3	Not enough reduction power
CuCl+CuBr	1	2.5	8	180° C	3	Nanowire and Nanoparticle formation
CuCl	1	3	3	180° C	3	Irregular nanowires and amorphous structures
CuCl	1	0	10	180° C	3	Nanoparticles and amorphous structures

9. Annex B

30 nm NWs with multi-shaped NPs.

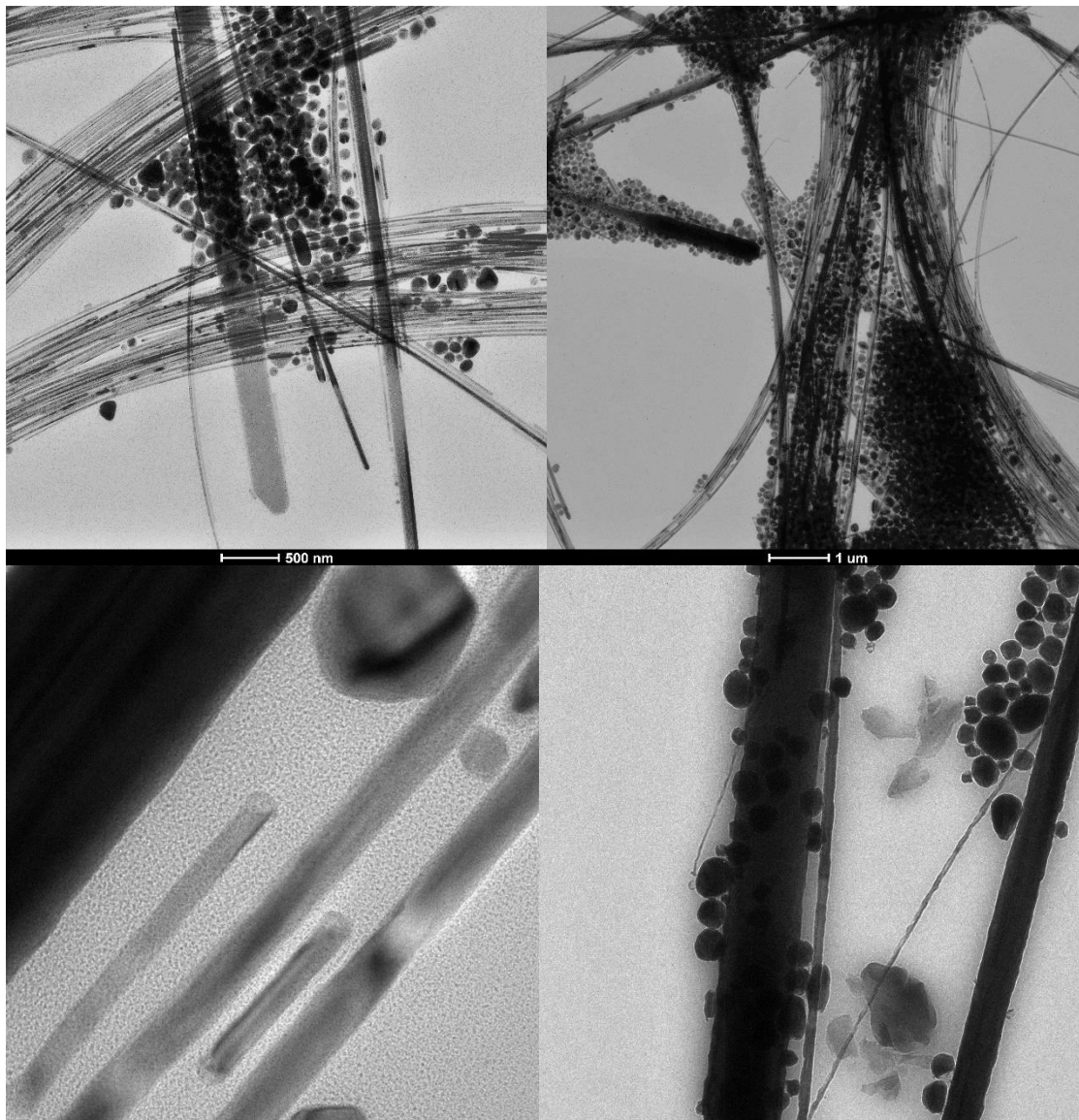


Figure 46: TEM images with different magnifications of the 30 nm NW with multi-shaped NPs

10 Annex C

30 nm NWs with Nanopyramids.

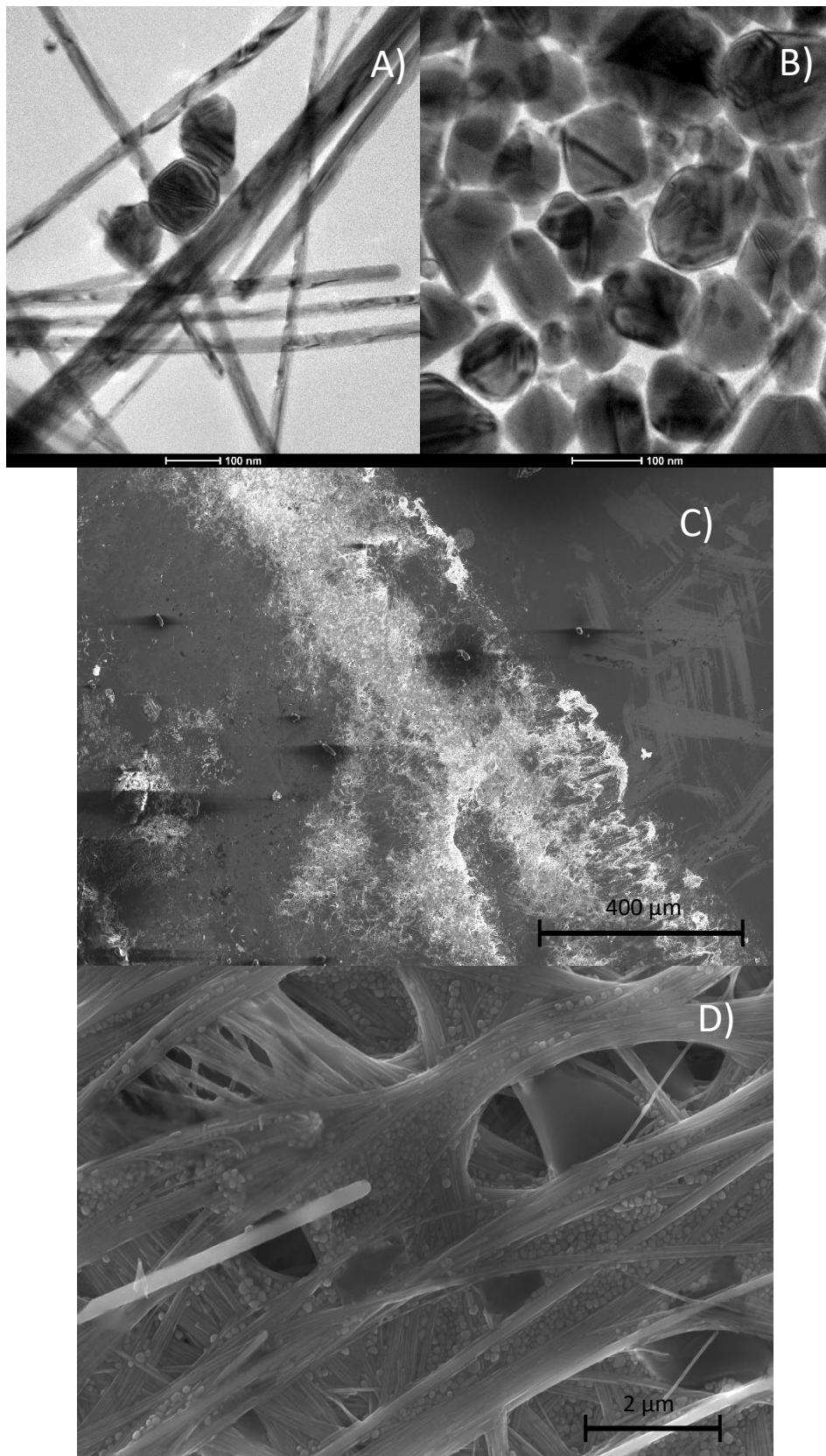


Figure 47: A) and B) HRTEM images of the Nanopyramids. C) Loss of catalyst sample over the electrode after activity at -1.3V shown using SEM. D) SEM image showing NWs and NPs structure after 2 hours of activity at -1.3V

11 Annex D

40 nm NWs with multi-shaped NPs.

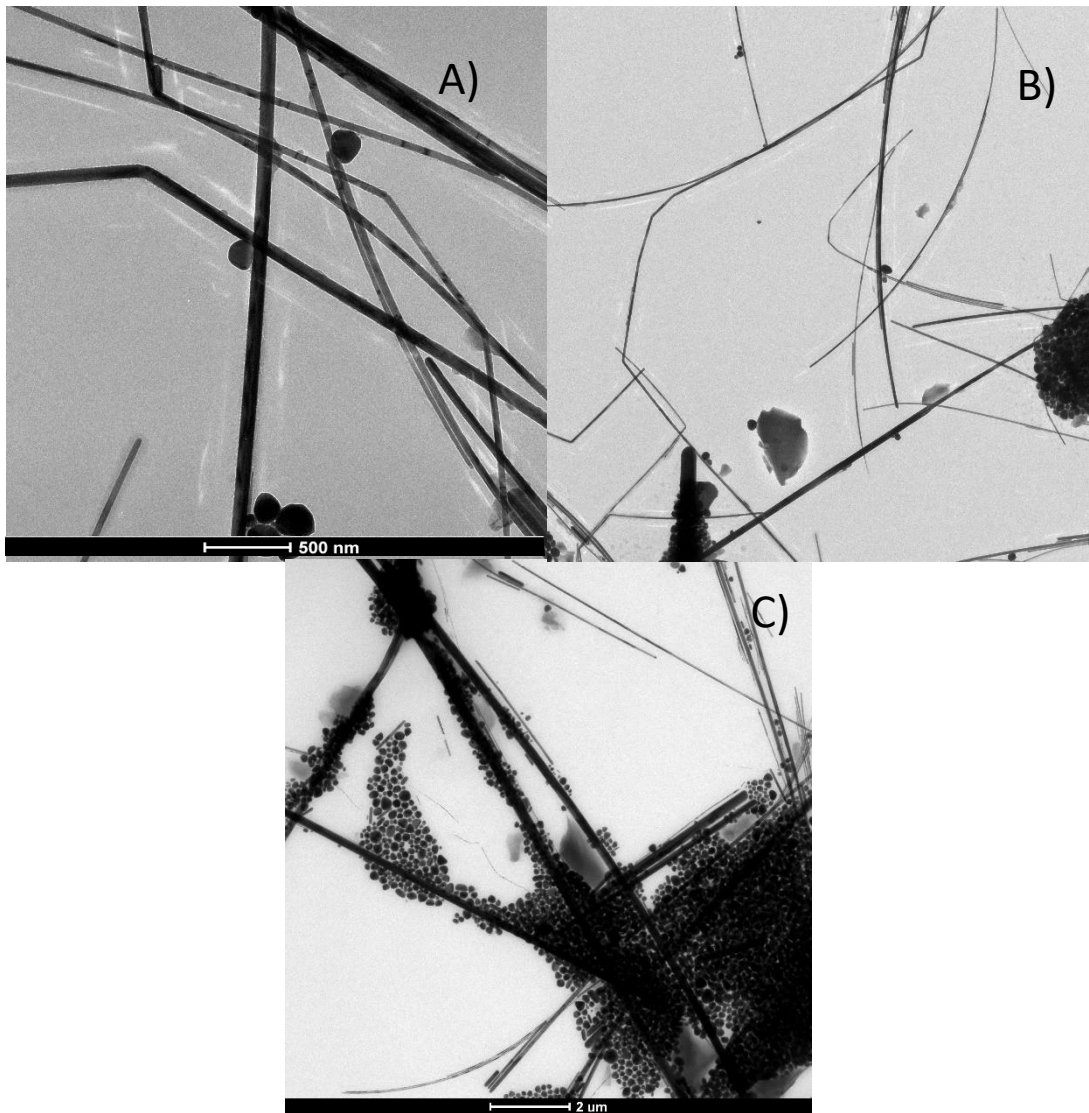
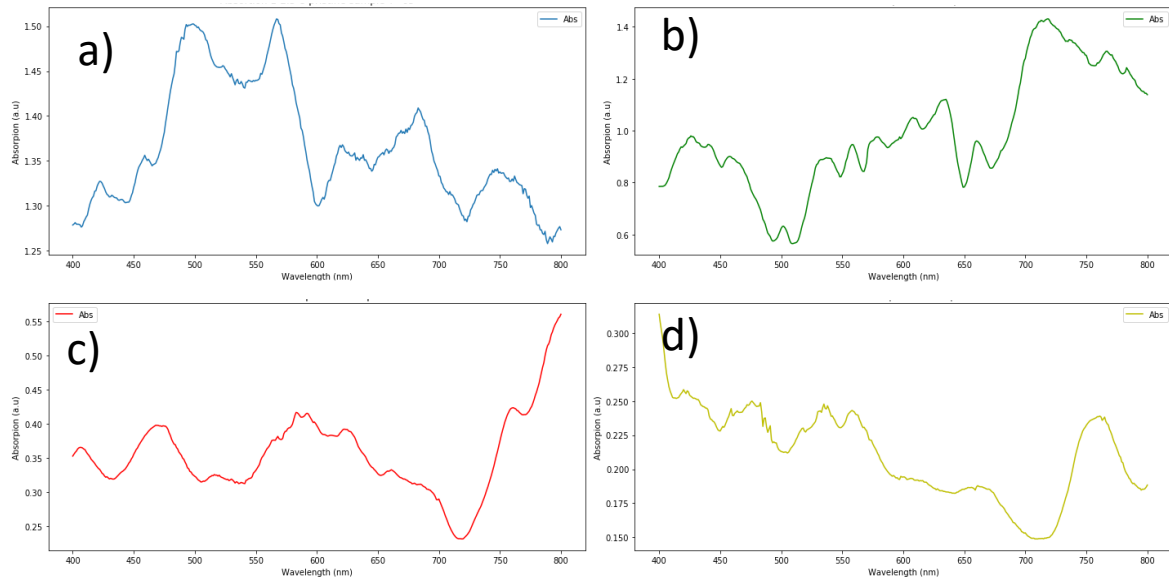


Figure 48: A) and B) TEM images of the 40 nm NWs changing direction growth C) TEM image of the 40 nm NWs with a high concentration of NPS

12 Annex E

Absorption spectra of the 30 nm NWs with nanopyramids



Graph 2: Uncoheren absorption spectrum of the pristine 30 nm NWs nanopyramids sample at a) 0 s b) 45 s c) 90 s d) 135 s. All pristine catalysts sample shown a similar behaviour.